Dário Barros Rodrigues
BSc and MSc in Biomedical Engineering

Target-Specific Multiphysics Modeling For Thermal Medicine Applications

Dissertation to obtain the degree of Doctor of Philosophy in Biomedical Engineering

Supervisor: Professor Paolo Francesco Maccarini, PhD
Duke University, USA

Co-supervisors: Professor Pedro Jorge da Silva Pereira, PhD
Instituto Superior de Engenharia de Lisboa, Portugal

Professor Paulo Limão-Vieira, PhD
Universidade Nova de Lisboa, Portugal

Jury

President: Professor António Manuel Nunes dos Santos, PhD
Examiners: Professor Eduardo Luís Bliebernicht Ducla-Soares, PhD
Professor João Manuel Ribeiro da Silva Tavares, PhD
Vowels: Professor João Erse de Goyri O'Neill, PhD
Professor Jorge Manuel Lopes Leal Rodrigues da Costa, PhD
Professor Luís Manuel Trabucho de Campos, PhD

FACULDADE DE CIÊNCIAS E TECNOLOGIA
UNIVERSIDADE NOVA DE LISBOA

November 2013

Target-Specific Multiphysics Modeling For Thermal Medicine Applications

Dedicado aos meus pais, Abílio e Maria Emília.
Dedicated to my parents, Abílio e Maria Emília.

“It is said that mathematics is the language of Nature. If so, then physics is its poetry.”
Hermann Weyl

Abstract

This thesis addresses thermal medicine applications on murine bladder hyperthermia and brain temperature monitoring. The two main objectives are interconnected by the key physics in thermal medicine: heat transfer. The first goal is to develop an analytical solution to characterize the heat transfer in a multi-layer perfused tissue. This analytical solution accounts for important thermoregulation mechanisms and is essential to understand the fundamentals underlying the physical and biological processes associated with heat transfer in living tissues. The second objective is the development of target-specific models that are too complex to be solved by analytical methods. Thus, the software for image segmentation and model simulation is based on numerical methods and is used to optimize non-invasive microwave antennas for specific targets. Two examples are explored using antennas in the passive mode (probe) and active mode (applicator).

The passive antenna consists of a microwave radiometric sensor developed for rapid non-invasive feedback of critically important brain temperature. Its design parameters are optimized using a power-based algorithm. To demonstrate performance of the device, we build a realistic model of the human head with separate temperature-controlled brain and scalp regions. The sensor is able to track brain temperature with 0.4 °C accuracy in a 4.5 hour long experiment where brain temperature is varied in a 37 °C, 27 °C and 37 °C cycle.

In the second study, a microwave applicator with an integrated cooling system is used to develop a new electro-thermo-fluid (multiphysics) model for murine bladder hyperthermia studies. The therapy procedure uses a temperature-based optimization algorithm to maintain the bladder at a desired therapeutic level while sparing remaining tissues from dangerous temperatures. This model shows that temperature dependent biological properties and the effects of anesthesia must be accounted to capture the absolute and transient temperature fields within murine tissues. The good agreement between simulation and experimental results demonstrates that this multiphysics model can be used to predict internal temperatures during murine hyperthermia studies.

Keywords: Multiphysics, Thermal Medicine, Bioheat Transfer, Antenna Design, Microwave Hyperthermia and Microwave Radiometry.

Resumo

Esta dissertação aborda aplicações em Medicina Térmica para estudos de hipertermia em roedores e para a monitorização da temperatura do cérebro em humanos. Os seus dois principais objectivos estão interligados por fenómenos de transferência de calor. O primeiro objectivo consiste no desenvolvimento de uma solução analítica para caracterizar a transferência de calor em tecidos biológicos multicamada. Esta solução inclui mecanismos de termorregulação e é essencial para compreender os fundamentos subjacentes à física e à biologia associados aos fenómenos de transferência de calor em tecidos biológicos. O segundo objectivo é o desenvolvimento de modelos com alvos específicos que têm de ser abordados com métodos numéricos por serem demasiado complexos para métodos analíticos. Para este fim, foram desenvolvidos códigos para a segmentação de imagens utilizadas na simulação dos modelos com alvos específicos. Estes códigos usam diversos métodos numéricos, entre os quais, o método dos elementos finitos para optimizar antenas de micro-ondas não invasivas dirigidas a alvos específicos. Dois exemplos são apresentados: antena no modo passivo (sonda) e no modo activo (aplicador).

A antena passiva integra um sensor radiométrico de micro-ondas desenvolvido para a medição não invasiva da temperatura do cérebro em tempo real. Os parâmetros geométricos da antena são determinados usando um algoritmo que optimiza a colecta de energia proveniente do cérebro. Um fantoma realista da cabeça humana foi construído para demonstrar o desempenho da antena. Este fantoma inclui dois compartimentos líquidos correspondentes ao escalpe e ao cérebro, cuja temperatura é controlada de uma forma independente. O erro do sensor radiométrico é de 0.4 °C numa experiência com uma duração de 4.5 horas, onde a temperatura do fantoma líquido do cérebro é variada num ciclo de 37 °C, 27 °C e 37 °C.

A antena no modo activo consiste num aplicador de micro-ondas com um sistema de arrefecimento integrado e é utilizada para desenvolver um novo modelo multi-físico para estudos de hipertermia na bexiga de roedores. O planeamento da terapia é assistido por um algoritmo para a optimização do aquecimento da bexiga salvaguardando os tecidos circundantes de excessos de temperatura. Este mode1o demonstra que a dependência das propriedades biológicas na temperatura e na anestesia tem de ser contabilizada para caracterizar correctamente a distribuição de temperatura no interior do corpo dos roedores. A boa concordância entre os resultados numéricos e os experimentais demonstra que este modelo multi-físico pode ser utilizado para prever a distribuição da temperatura durante estudos de hipertermia em roedores.

Palavras-chave: Multi-física, Medicina Térmica, Transferência de calor em tecidos biológicos, Desenho de Antenas, Hipertermia por Micro-ondas e Radiometria por Micro-ondas.

Acknowledgments

First of all, I would like to thank Professor Pedro Pereira. He has been in my PhD life since an early phase and enhanced deeply my understanding of academic research and writing style. Furthermore, he taught me how to apply Physics and Mathematics to the real world and that revolutionize the way I look to partial differential equations that are the basis of the most interesting disciple of knowledge: Physics. Furthermore, his level of dedication and commitment to the truth is really inspiring.

Professor Paul Stauffer accepted me at Duke University and that set the beginning of an outstanding journey. Although he was not an official advisor he sure worked as one. The extensive corrections and constructive critics to my work clearly enhanced my research skills. By treating me as an equal he forced me to find the best in me. I feel like I had an injection of Thermal Medicine after spending two years at Duke University and a significant part of it I owe to him. I will always be grateful to you and to your family. Debby is an outstanding woman that gives the best pieces of advice and best parties in the USA. Cleta is by far the youngest minded grandmother I know. You all made me feel at home and I'm really thankful for it.

The permanent and revolutionary ideas of Professor Paolo Maccarini were a source of continuous learning. The scientific discussions – either in the lab or bar – and teachings were endless and the overnights at the radiometry room as well. He sure passed me his passion for microwave engineering. Professor Paolo and Professor Paul were more than just advisors they were great colleagues and friends that had significant patience for all my questions and contributed for both my professional and personal development.

I went to visit Professor Paulo Limão-Vieira at the right moment. I was not sure of what to do regarding to my PhD and he clearly indicated me the right course to take. His level of dedication and efficiency was remarkable and I thank him for providing me fast feedback for all the scientific and bureaucratic paperwork.

I would like to thank Professor Valentina Vassilenko, Professor José Luis Ferreira and Professor João Goyri O'Neill that initiated with me my PhD adventure.

I would also like to thank my colleagues Tiago, Sara and Fabio for the many fruitful discussions and friendship; and friends in Durham especially Haydee, Ana, Maria, Alessandro, Simo and Max.

My PhD life was marked by a health problem that reduced my ability to work and I would like to thank all the health professionals that treated me and helped me understanding the source of the problem: Luís, Fernanda, Ricardo, Acácio, Ana Roque, Kitty, Dr. Washington, Dr. Mascarenhas, among many others.

There is no joy in life without true friends. Henrique, Vitor, Vidinha, Xico, Zé, Pedro, Anacleto, Danny, Raquel, Maria Inês, Ana, Nuno, Rita. You all make my life colorful. Especially thank to Vitor for the many times he shared his house with me and to Henrique and Danny for the fruitful scientific discussions.

To Anabela, Paulo, Sónia, Luís Pedro, Daniel and Mónica you set a standard at many levels in my life. Although you are quite different, you all share strong power will and remarkable skills that inspire me. In many occasions you all gave me the support I needed. I'm a happy younger brother.

To my dear nieces and nephews: Daniela, Francisco, Duarte, Mafalda and Martim, you are simply great. Besides testing my patience, you bring joy to my life at a very fundamental level and I hope I can be present many times to see you grow and be part of that growth.

To all my family who, in different circumstances, helped me in my PhD life: thank you. A special thanks to my aunt Benilde that is tireless in helping those in need.

Finally and most important acknowledgement: to my parents. *Vocês não são apenas um exemplo. Vocês são o exemplo a seguir. Trago em mim muito de vós e isso orgulha-me. Estão sempre prontos a ajudar, a mim e a qualquer outra pessoa. O vosso coração não tem limites e a vossa capacidade de trabalho e dedicação também não. Diria mesmo que trabalham demasiado, mas já percebi que isso está no vosso sangue. Algo que passaram para mim, e para os meus irmãos, o qual agradeço. Para se chegar a algum lado tem que se trabalhar muito e nunca se deve deixar de dar a mão a quem necessita. Estes ensinamentos assim como as vossas acções diárias transmitem-me referências que um dia ambiciono passar para uma próxima geração. Espero vir a ser um pai tão bom como vocês foram e estão a ser. Obrigado.*

Contents

List of figures

List of tables

List of nomenclature

1D, 2D and 3D	One, two and three dimensional, respectively
ADC	Analog-to-digital converter
Avizo	Avizo® segmentation software (VSG, Burlington, MA, USA)
ANSYS	Engineering simulation software (Ansys Inc., Philadelphia PA)
BC	Boundary conditions
BMI	Body mass index
BNC	Bayonet Neill–Concelman
CAD	Computer-aid design
CFL	Courant–Friedrichs–Lewy
COMSOL	COMSOL Multiphysics software (COMSOL, Palo Alto, CA, USA)
CT	X-ray computed tomography
dB	Decibel
DesignModeler	3D CAD Design Software (Ansys Inc., Philadelphia PA)
Eccostock	Eccostock® HiK500F (Emmerson&Cumming, Randolph, MA, USA)
e.g.	for example (*exempli gratia*)
EM	Electromagnetic
EMI	Electromagnetic interference
FCC	Federal Communications Commission
FEM	Finite element method
GMRES	Generalized minimal residual method
HDMI	High-Definition Multimedia Interface
HFSS	High frequency structural simulator (Ansys Inc., Philadelphia PA)
HP	High pass
i.e.	In other words (*id est*)
ID	Identification number
IRB	Institutional review board
Labview	Laboratory virtual instrument engineering workbench (National Instruments, Austin, TX, USA)
LP	Low pass
MEAS	Measurement
MFH	Magnetic fluid hyperthermia
microMR	Micro-magnetic resonance
MMC	mitomycin-C
MW	Microwave(s)
NIH	National Institutes of Health
PARDISO	Parallel sparse direct linear solver
PC	Personal computer
PDE	Partial differential equation
RO	Substrate from Rogers Corp., USA
SAR	Specific absorption rate
SD	Standard deviation
TSMM	Target-specific multiphysics modeling

ULN	Ultra-low noise
USB	Universal Serial Bus
SMA	SubMiniature version A
V-solution	Analytical solution of the analytical model proposed in this thesis
vs.	Versus

List of symbols

*	The subscript asterisk is used to denote dimensional quantities only in chapter 2
$\{\boldsymbol{e}_x, \boldsymbol{e}_y, \boldsymbol{e}_z\}$	Orthonormal basis vectors
a	Spiral growth rate coefficient
a_m, b_m, d_m	Unknown coefficients to define R and Ψ
A_1	Maximum strength of the volumetric heat generation
A_{in}, B_{in} and C_{in}	Coefficients to define the boundary conditions of the inner surface
A_{out}, B_{out} and C_{out}	Coefficients to define the boundary conditions of the outer surface
B	Dissipation of heat through blood perfusion
Br	Brinkman number
c	Specific heat capacity (Chapter 2) Speed of light (remaining chapters)
c_b	Specific heat capacity of blood
c_{np}	Specific heat capacity of nanoparticles
C_p	Specific heat capacity
$\hat{c}$, $\hat{\phi}$, $\hat{\omega}$, $\hat{\Phi}$, $\hat{\Omega}$	Coefficients to define some matrices to evaluate u and v
$\bar{c}$, $\bar{\phi}$, $\bar{\omega}$	Coefficients of the determinant to determine the eigenvalues
$\hat{C}$	Real constant
d	Characteristic dimension of the mouse
$\tilde{d}$	Coefficient to redefine d_m
D	Inlet tube diameter
e	Radiation emissivity
$\boldsymbol{E}$	Time-harmonic electric field vector
$\boldsymbol{E}_0$	Spatial dependent component of $\boldsymbol{E}$
E_{0x}, E_{0y}, E_{0z}	Components of the electric field $\boldsymbol{E}_0$
E_a	Activation energy
Ei	Exponential integral
f	Frequency
f_l	Lower frequency limit where $S_{11} \leq$ -10 dB
f_h	Upper frequency limit where $S_{11} \leq$ -10 dB
f_H	Upper cut-off frequency
f_L	Lower cut-off frequency
$\boldsymbol{F}$	Volume force induced by gravity
g	Gravitational acceleration
G	G = 0, 1 and 2 for problems with 1D Cartesian, cylindrical and spherical symmetric regions, respectively (chapter 2) Radiometer gain (remaining chapters)
h_{air}	Air convective coefficient
H	Solution of the homogenous equation to determine $\hat{T}$
i	Tissue layer index
I, K	Modified Bessel functions of the first and second kinds, respectively

$Im(z)$	Imaginary part of the complex number z
j	Imaginary unit
J, Y	Bessel functions of the first and second kinds, respectively (chapter 2)
J	Goal function (chapter 4)
J_n	Normalize goal function
k	Thermal conductivity
k_{bl}	Thermal conductivity of blood
k_B	Boltzmann constant
k_{scalp}	Thermal conductivity of scalp
l_t	Initial edge length
L	Tissue layer (chapter 2)
	Spiral length (chapter 3)
m,l	Natural numbers
m_m	Mass of the mammal
M	Order of the truncation of the infinite Bessel series (chapter 2)
	Metabolic heat rate (chapter 4)
M_0	Basal metabolic heat rate
M_A	Impaired metabolic heat rate due to anesthesia
M_{Q10}	Metabolic heat rate given by the van't Hoff Q10 factor
N	Number of tissue layers or antenna regions (chapter 2)
	Number of log-spiral turns (chapter 3)
N_m	Coefficient to define the orthogonality condition
$\boldsymbol{n}$	Unit vector normal
np	Nanoparticles index
O_2	Oxygen
p	Pressure
P	Internal heat generation (chapter 2)
	Radiated power (remaining chapters)
P_{ant}	Radiometric power collected by the antenna (chapter 3)
	Input power of the antenna (chapter 4)
P^*_{ant}	Dimensionless input power of the antenna
P_{ave}	Average power
P_d	Power loss density
Q_1, Q_2, Q_3	Coefficients of the polynomial heat source term
Q_{10}	Species dependent temperature coefficient
Q_m	Metabolic heat generation
Q_{m0}	Basal metabolic heat generation
Q_{ms}	Slope of the linear relationship to define Q_m
Q_{TOTAL}	Total amount of energy produced by a mammal
r	Spatial coordinate
$\boldsymbol{r}$	3D position vector
r_0	Radius of the inner tissue layer
r_{bl}	Blood vessel radius

r_ϕ	Parameter to determine how far the nanoparticles spread from injection site
R	Spatial dependent function to define $\bar{T}$
R_ω	Anesthesia induced change in blood perfusion
R_M	Anesthesia induced change in metabolism
Re	Reynolds number
Ri	Richardson number
S	Particular integral of the differential equation to determine $\hat{T}$
S_{11}	Mismatch (dB) between antenna and load
t	Time
t_{heat}	Heating time
T	Temperature
T_0	Initial temperature
T_a	Arterial temperature
T_{air}	Air temperature
T_{brain}	Radiometric brain temperature
T_B	Brightness temperature
$T_{bladder}$	Bladder temperature
T_{bolus}	Temperature at the input of the water-loaded waveguide antenna
T^*_{bolus}	Dimensionless temperature at the input of the water-loaded waveguide antenna
T_{cr}	Critical temperature
T_{EMI}	Radiation power contribution from EMI
T_{naso}	Nasopharyngeal temperature
T_{pad}	Temperature of the thermal pad heater
T_{r0}	Initial temperature reference
T_{REC}	Radiation power contribution from microwave receiver
T_{rectum}	Rectum temperature
T_{ss}	Steady state temperature
T_{uterus}	Uterus temperature
T_t	Transient temperature
$T_{targetmax}$	Maximum target temperature
$T_{targetmin}$	Minimum target temperature
$\bar{T}$	Transient and homogenous component of temperature in the dimensionless form
$\hat{T}$	Steady state and nonhomogeneous component of temperature in the dimensionless form
u,v	Unknown coefficients associated to the Bessel functions of the first and second kinds, respectively
$\boldsymbol{u}$	Velocity vector
u_m	Mean fluid velocity
V	Sensing volume
w	Weighting functions for the goal function

W Generic spatial function to define the particular integral of the steady state nonhomogeneous problem (chapter 2)
Weighting function of the antenna's radiation pattern (chapter 3)

z Complex number

$\mathbb{N}$ Set of natural numbers

$\mathbb{R}$ Set of real numbers

α Coefficient of the thermal conduction term in the dimensionless bioheat transfer equation

α_{air} Thermal diffusivity of air

β Coefficient of the temperature term in the dimensionless bioheat transfer equation (chapter 2)
Thermal expansion coefficient (chapter 4)

$\delta_{coverlay}$ Coverlay thickness

Δf Frequency bandwidth

ε Truncation error of the transient analytical solution (chapter 2)

ε_0 Relative permittivity of free space

ε_c Complex dielectric permittivity

ε_r Relative permittivity

$\varepsilon_{r,eff}$ Effective relative permittivity

ε_{skin} Average dimensionless body emissivity constant

$\varepsilon(G)$ Orde of the modified Bessel functions given by (G-1)/2

γ Coefficient associated with the spatial coordinate r which define the argument of the modified Bessel functions of the first and second kinds

Γ Digamma function (chapter 2)
Input voltage reflection coefficient (remaining chapters)

$|\Gamma|^2$ Power reflection coefficient

η Antenna efficiency

$\eta_{\Delta f}$ Average antenna efficiency over Δf

φ Volume fraction of nanoparticles in tissue

λ Eigenvalues of the analytical problem (chapter 2)
Wavelength (remaining chapters)

μ Dynamic viscosity

μ_0 Magnetic permeability of free space

ν Kinematic viscosity

v_{air} Wind speed

θ Polar coordinate

ρ Polar coordinate (chapter 3)
Mass density (remaining chapters)

ρ_0 Initial inner radius of the log-spiral antenna

ρ_1 Initial outer radius of the log-spiral antenna

ρ_{e0} Inner edge of the log-spiral antenna

ρ_{e1}	Outer edge of the log-spiral antenna
ρ_{ext}	Outermost radius of the log-spiral
ρ_b	Mass density of blood
ρ_{np}	Mass density of nanoparticles
σ	Heat source term in the dimensionless bioheat transfer equation (chapter 2) Electric conductivity (remaining chapters)
σ_b	Stefan-Boltzmann constant
υ_{air}	Kinematic viscosity of air
ω	Angular frequency
ω_0	Basal mass blood perfusion rate
ω_1, s	Coefficients for temperature dependence of ω_B
ω_A	Impaired mass blood perfusion rate due to anesthesia
ω_b	Blood perfusion rate
ω_B	Mass blood perfusion rate
ω_m	Average blood perfusion
Ψ	Time dependent function to define $\bar{T}$

Chapter 1

Introduction

The real world is inherently multiphysics. Heat transfer, in particular, does not exist in isolation. Rather, other physical effects, like electromagnetic heating or mechanical fluid forces, change the thermodynamics of any system. By considering all relevant physical effects, it is possible to develop mathematical models that provide accurate surrogates for complex biological systems. Such models allow detailed investigation of interactions between living organisms and the outside world. The theoretical characterization of biological systems provided by these models can be used to explore new diagnostic and therapeutic techniques in the medical field and improve the results of evolving pre-clinical and clinical applications. This thesis focuses on thermal medicine applications that involve measurement or manipulation of tissue temperatures for either diagnosis or treatment of disease.

1.1. Motivation

Thermal medicine is a branch of medical science that deals with manipulation of tissue temperature for treatment or diagnosis of disease. It can be traced back to the earliest practice of medicine where hot and cold were used for therapeutic purposes. Modern research in thermal medicine however aims to understand molecular, cellular and physiological effects of temperature manipulation as well as the stress response induced by disturbing the body temperature homeostasis [1, 2].

There are a growing number of thermal-based clinical applications that benefit patients with a variety of diseases, such as cancer or ischemic heart disease [2-4]. In the same track, numerous medical devices have been developed to address these novel applications. They use non-ionizing radiation to induce the desired temperature variation, by means of ultrasound [5], laser [6] or radio waves [2]. The specificity of each heating/cooling mechanism and the complexity of the target – a biological system

– develop a need for target-specific medical equipment that must be designed to be effective and safe for the intended clinical application.

This thesis presents a new strategy to assist the development of improved medical devices for the field of thermal medicine. The strategy is built upon a target-specific model that is coupled with the medical device in a virtual environment (see Figure 1.1). The most important elements in this modeling strategy are the following: (1) accurate anatomy and biological properties in the target-specific model, which includes both target and relevant surrounding structures; (2) accurate geometry and thermophysical properties in the medical device model; (3) physical interaction between the medical device and the specific target; (4) thermoregulation mechanisms, such as the temperature dependence of biological properties; and (5) effects on the biological properties of tissue from exogenous factors such as anesthesia.

Accurate biological and thermophysical properties are best achieved by measuring *in situ* the specific properties of the target and medical device. If not possible, extensive literature review has to be considered to find the most adequate properties. In the particular case of biological properties, it is important to account for the conditions where such properties are acquired. The most important factors to take into consideration in this stage of the modeling process are the following: animal species, measurement technique, temperature, environmental conditions, use of anesthesia, and type and concentration of anesthesia.

Once the model is established, a multiphysics simulation can be implemented in order to characterize the system and theoretically optimize the medical device. This is achieved using specific goals for the treatment or diagnostic tool. This comprehensive approach is here named as target-specific multiphysics modeling (TSMM) and its efficiency is presented for both therapeutic and diagnostic medical devices:

a) Diagnostic tool case study:
   Microwave radiometry probe for brain temperature monitoring;
b) Therapeutic tool case study:
   Microwave hyperthermia applicator for murine bladder cancer treatment.

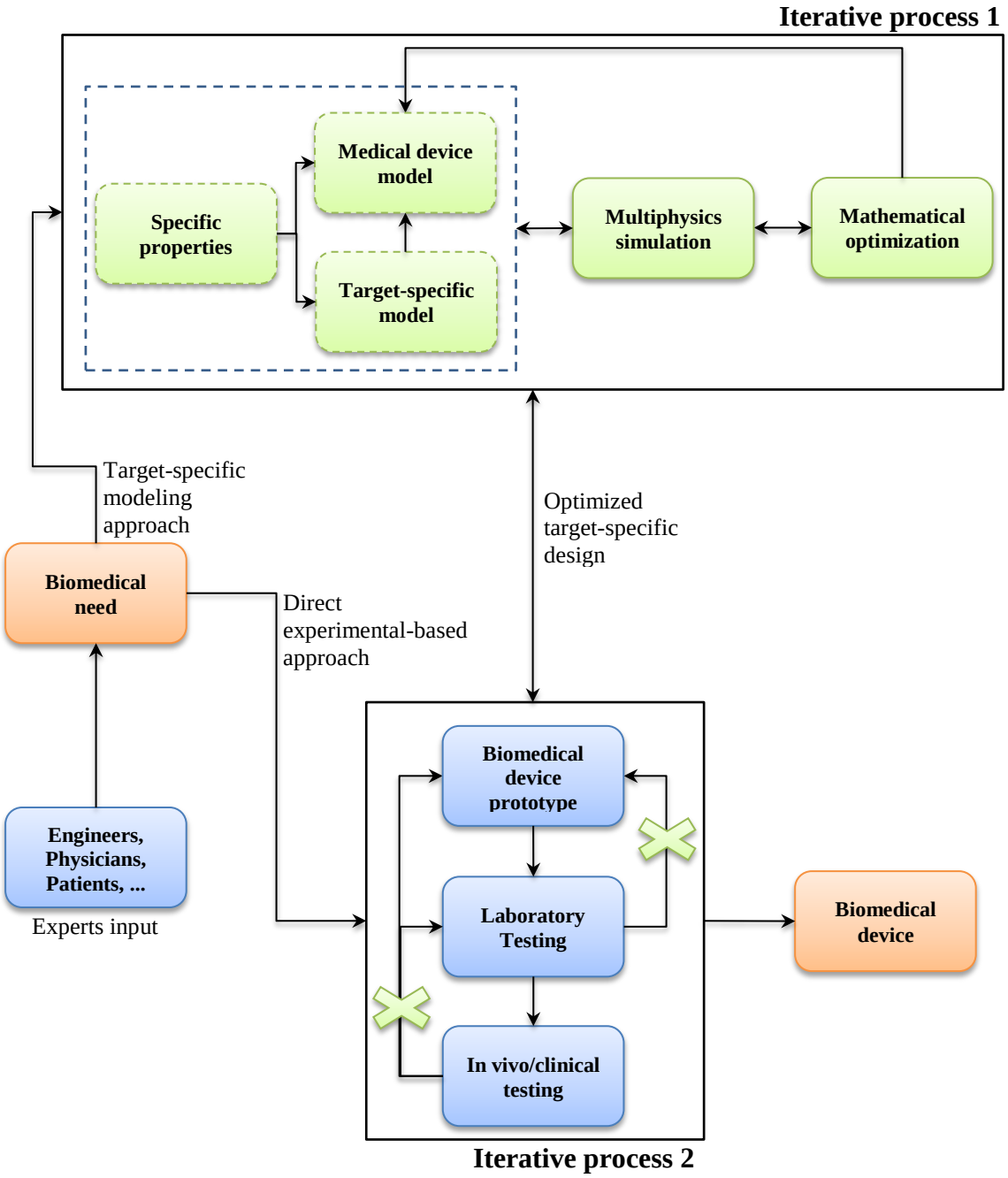

Figure 1.1 – Workflow for the target-specific multiphysics modeling (TSMM) *vs*. the traditional direct approach for the development of medical devices. By including iterative process 1 (virtual environment) in the medical device design, iterative process 2 (experimental) is dramatically reduced. Thus, using a TSMM approach reduces cost, increases efficiency, and improves the clinical outcome.

1.2. Case study techniques

1.2.1. Distinctions between probes and applicators

As in any field, terminology is essential to create standards. Microwave (MW) probes and applicators have similar underlying fundamental principles associated with their use of electromagnetic fields. In practice, however, there are significant differences between MW probes and MW applicators that make the design considerations quite different.

A microwave applicator is a device that applies microwave energy into a volume at a level sufficient to create either a permanent or temporary change in a material parameter or property [7]. The change could be a rise in temperature either to induce hyperthermia ([42, 45] °C for [15, 60] min) or ablation (>47 °C for >10 min) of cancerous tissues [2]. Important considerations for applicator design include the required power level and operating frequency, which is often restricted to one of the Industrial, Scientific, or Medical (ISM) bands: 915 MHz, 2.45 GHz, 13.56 MHz, 24.13 GHz, 27.12 MHz and 40.68 MHz [8]. Note that these are approved frequencies for the North and South American continents. The example explored in this thesis consists of a microwave applicator operating at 2.45 GHz and using 10-17 W for heating murine bladder [3, 9].

A probe or a "sensor head" is a device that uses the field interactions to obtain information from a material [7]. It is coupled to an electronic system named sensor that processes that information and converts it into a readable signal. Some probes might apply an electric field to human tissues to obtain information about its dielectric properties [10]. Other probes are completely passive and collect information about the tissue such as thermal noise that may be converted into temperature using a radiometric sensor [11]. In general, the power levels required for probes are far below those used in applicators. On the other hand, probes often involve input signals over a wide bandwidth, which allow probes to work outside the allowable ISM frequency bands [7]. The example explored in this thesis consists of a microwave antenna probe operating in the band [1.1, 1.6] GHz for radiometric monitoring of brain temperature [3, 9].

1.2.2. Microwave radiometry for brain temperature monitoring

Microwave radiometry is a non-invasive technique that collects thermal radiation emitted in the microwave frequency spectrum by any material above absolute zero

temperature. This type of radiation, also called electromagnetic noise, is generated by the random motion of charged particles [12]. It propagates through bodies and is partially absorbed and partially irradiated once reaching the body surface. The intensity of this emission is described by Planck's blackbody radiation law and, in the microwave region, is given by $P = Gk_BT\Delta f$, where P is the radiated power, G is the radiometer total gain, k_B the Boltzmann's constant, T is the blackbody temperature and Δf the bandwidth over which power is being collected. Blackbodies are idealized materials that absorb all incident energy and reflect none. Any real body, however, partially reflects the incident energy. Thus, a real body does not radiate as much power as a blackbody would at the same temperature. This results in $P = Gk_BT_B\Delta f$, where T_B is the brightness temperature of the real object that can be related to the ideal blackbody using $T_B = eT$, where e is the real body emissivity ($0 \leq e \leq 1$) [12, 13].

MW radiometry is well assessed as a monitoring tool in remote-sensing geophysical applications [14], such as monitoring global temperature trends [15] or estimation of surface soil moisture and sea surface salinity [16]. Over the last 25 years it has also been proposed as a passive and noninvasive technique for measuring/ monitoring temperature in medical applications. This interest rose from the possibility to derive temperature of deep-seated targets – located a few centimeters depth – from the microwave thermal radiation emitted by tissue [27, 34]. Proposed applications of MW radiometry in medicine include detection of breast cancer [17], monitoring and control of superficial and hyperthermia applicators for deep regions [18-22], measurement of brain temperature in infants [23, 24] or adult brain phantoms [25], vesicoureteral reflux detection in young children [26-29] and more recently monitoring of brown fat metabolism [30].

A crucial limitation of microwave radiometry lies in the nature of electromagnetic noise itself: extremely low power levels of the order 10^{-14} W/MHz at 37 °C, where "/MHz" stands for "per MHz of bandwidth". Thus, it becomes essential to maximize power collection by using a probe that collects radiation over a wide band. In MW radiometry, the probe is usually a wideband multiple polarization microwave antenna such as a microstrip log-spiral structure [31, 32]. Once received by the antenna, the impinging radiation is transduced into an electrical current at the input of the receiver circuit. This microwave radiometer receiver uses ultra-low loss and ultra-low noise high gain MW components to amplify and process the extremely low energy signal in order to retrieve

brightness temperature using $P = Gk_BT_B\Delta f$. The ultimate challenge for MW radiometry in medicine is to retrieve, however, temperature solely from deep tissue targets. The brightness temperature includes information from both superficial and deep tissues. Thus, a TSMM approach can be used to characterize the target and its surroundings and develop an adequate tool to separate the target temperature from T_B [33-35].

1.2.3. Microwave hyperthermia for cancer treatment

In oncology, the term hyperthermia refers to the treatment of malignant diseases by delivering heat and inducing neoplastic cell death in various ways. Tumor cell death can occur through a direct path, where heat causes denaturation of cytoplasmatic and membrane proteins. This direct cell kill occurs at temperatures usually higher than [43, 45] °C for 60 minutes [36-38]. Hyperthermia can also be used via an indirect path in conjunction with two distinct nanoparticles: thermosensitive liposomes that carry drugs through the blood stream and are liberated in the tumor by means of focused heating with, e.g., a microwave applicator [3, 39-41]; or magnetic nanoparticles that absorb energy from an externally applied electromagnetic (EM) field and release that energy in the form of heat into the surroundings – ideally the tumor [42-44].

The temperature at which hyperthermia is administered is critical and will induce different responses. For instance, moderate hyperthermia at 40 °C tries to reproduce fever and actually increases natural killer cells immunologic activity. Above 42 °C, however, cellular function is impaired [37, 45, 46].

All moderate hyperthermia modalities have in common that their efficacy is not enough to replace any of the established therapy modalities when applied alone. However, using hyperthermia as an adjuvant therapy enhances the cell-killing effect of radiation (thermal radiosensitization) and/or cytotoxic drugs (thermal chemosensitization). By applying hyperthermia at 42 °C, the tumor blood flow increases which oxygenates the cell. The oxygen increase makes the tumor more sensitive to radiation and thus increases the effectiveness of radiotherapy. In the case of chemotherapy, increasing blood flow in tumors will increase the drug delivery and thus the effectiveness of chemotherapy. Therefore, hyperthermia aims to improve the results of the conventional treatment strategies within the framework of multimodal treatment concepts [37, 47, 48].

This thesis addresses an EM method of heating – microwaves – and its most important aspect is the direct nature of energy deposition. There is no heat transfer in the conventional sense and, from a thermodynamic point of view, the material itself is the source of heat [7]. At radiofrequencies below 20 MHz, an EM field between implanted or surface contacting electrodes induces a net movement of electrons. The induced currents deposit power from resistive losses, with the highest power deposition occurring in tissues with the highest current density. At MW frequencies above 100 MHz, the radiative mode of EM propagation and dielectric losses in tissue predominate over conduction current losses. Under these conditions, heating results from friction among adjacent polar water molecules which oscillate in response to the time varying field [2, 49, 50].

A MW applicator can be designed using a power-based optimization approach, where the goal is focused on power deposition. This approach, however, does not take into account heat transfer. To treat cancers with any of the aforementioned hyperthermia techniques, we need to develop an optimization technique based on temperature in order to provide focused heating rather than focused power deposition. The latter does not take into account the many thermal mechanisms in biological systems. This is especially relevant since increasing temperature increases biological reaction rates such as metabolic heat or blood perfusion rates. This establishes a critical need for accurate applicator and biological models, and both are embodied in the TSMM approach.

1.3. Models and surrogates

The idea that something can be learned about a system by studying a different system, or surrogate, is central to all science. The relation between a system and its surrogates is embodied in the concept of a model [51] that can be either abstract or physical.

A mathematical model is an abstract description of a system that uses mathematical language. In biology or medicine, a mathematical model of a biological system is converted into a system of equations that translate all relevant physics of the biological problem. The solution of the equations describes how the biological system behaves spatially and either over time or at equilibrium. A computer model is a particular type of mathematical model where a computer software attempts to simulate an abstract model of a particular system. The software is primarily an equation solver and requires the

detailed physics of the system in order to evaluate its performance. To allow the modeling process to be target-specific, one must also provide a CAD (computer-aided design) model. CAD models are a sub-set of computer models that reproduce the geometry/anatomy of the system under analysis.

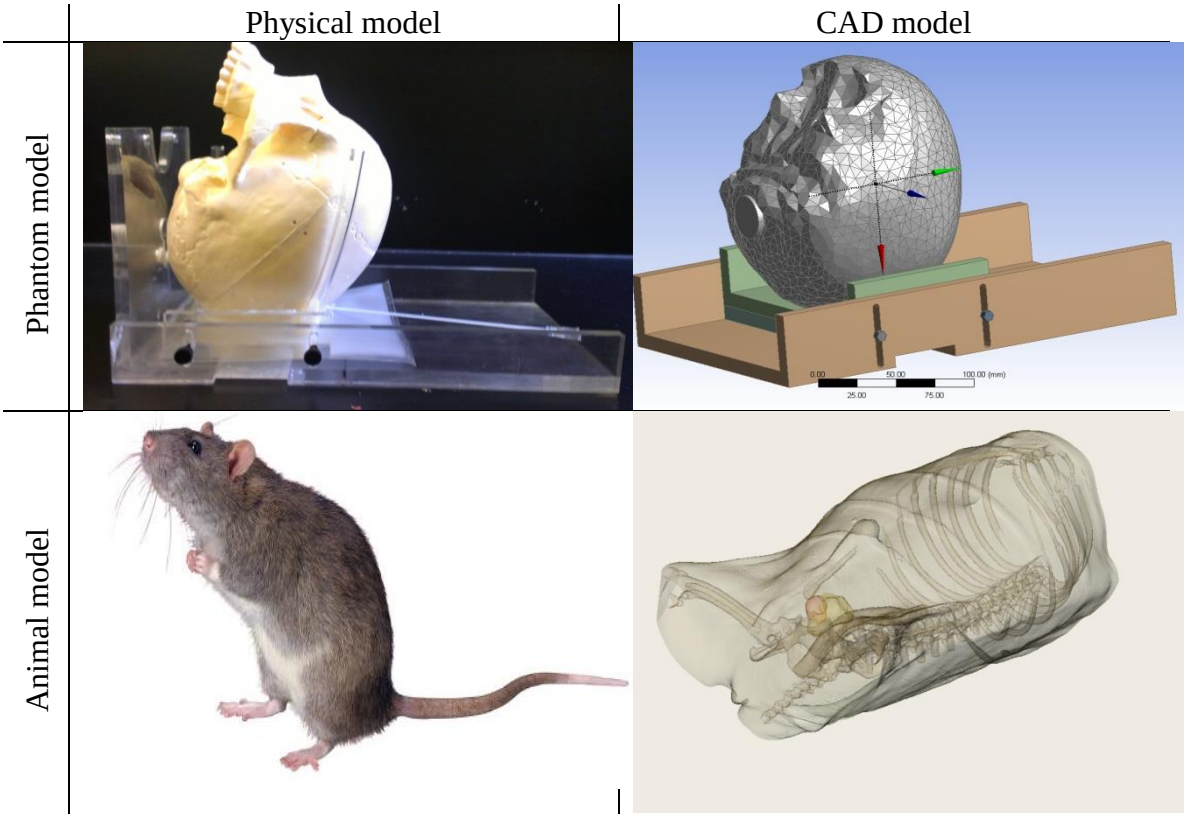

Figure 1.2 – Different models used in the thesis.

Physical models, on the other hand, are physical equivalent representations of a particular system. For the purpose of this thesis, two physical models are addressed: animal and phantom models (Figure 1.2). In medical research, rodents are often used as an animal model due to their availability and reproducibility of results. The second kind – phantom model – is a physical representation of a biological system that can use both organic and inorganic materials: water, sodium chloride, propylene glycol, ethylene glycol [52], vegetable oils [53] and agar [54] are often used. In studies of new applicators and probes in Medicine, both animal and phantom models have in common the target of minimizing the development path to human trials.

In this thesis, the term modeling refers to the process of developing a replica, on a computer, of a physical system so that it can be manipulated in a simulation

environment. The major advantage of computer models is that they allow testing of several "what-if scenarios" limited only by the available computer memory and processor speed. They require validation, however, which is provided by experimental procedures using matching physical models.

1.3.1. Analytical *vs.* numerical models

Computer algorithms solve the set of equations using two broad classes of distinguishable methods – analytical and numerical – to provide solutions for the mathematical problem. An analytical solution refers to an exact or approximate solution that can be obtained using algebra and calculus. They are useful to understand the fundamentals but require a significant simplification of the problem. Thus, analytical models are not usually used to simulate complex biological problems. Numerical solutions are based on approximation and iterative techniques to solve the governing equations. They are more flexible and arise from the need to estimate the performance of systems too complex for analytical methods. This is the reason why numerical models are the base of engineering analysis software [55]. Both approaches are presented in this thesis as well as their advantages and limitations.

1.4. Thesis structure and objectives

This thesis is composed of five chapters. The first chapter has been dedicated to a brief introduction about some applications in thermal medicine – microwave radiometry and hyperthermia – as well as the modeling techniques used to solve specific problems in this field. The research topics developed in this thesis are presented in the chapters 2, 3 and 4. Each chapter is autonomous and presents research published or submitted for international peer-review journals. Thus, the discussion, future studies and conclusions of each research topic are presented in the correspondent chapter. The final chapter presents the concluding remarks over all PhD research work.

There are four main objectives in this thesis interconnected by the key physics in thermal medicine: heat transfer. The first goal is to develop an analytical solution to characterize the heat transfer in a multi-layer perfused tissue. The second objective is the development of a multi-layered physical phantom of the human head to mimic real

temperature distributions in the human head. The third objective is the development of a target-specific radiometric microwave antenna to retrieve brain temperature from human brain. This antenna uses the head physical phantom to validate the antenna performance. The final goal is the development of a target-specific multiphysics model to surrogate in a virtual environment hyperthermia treatments of murine bladder using a target-specific microwave applicator.

In this thesis, we use several analytical and numerical methods. The analytical solution is deduced using the method of separation of variables, Bessel functions, eigenfunctions and eigenvalues. Some of these studies are implemented using Maple software and validated either with literature data or numerical solutions computed in COMSOL Multiphysics that uses the finite element method (FEM). The anatomical models are segmented in Avizo to produce anatomical accurate CAD models that are used to design the antenna or to implement the multiphysics analysis. The CAD structures are composed using ANSYS DesignModeler and imported to HFSS software to compute the electromagnetic simulations required for the antenna design. HFSS uses the finite element method and its solutions are further imported to COMSOL to perform thermo-fluid simulations. The experiments to monitor temperature are semi-automated using algorithms developed in Labview software.

Analytical solutions require a significant simplification of the problem but are essential to understand the fundamentals underlying the key physics of this thesis: heat transfer in biological tissues, commonly named bioheat transfer. In Chapter 2, an analytical solution to the transient and one dimensional (1D) bioheat equation is derived to calculate the heat transfer in a multi-layer perfused tissue. Multi-layer regions with 1D Cartesian, cylindrical and spherical symmetric geometries as well as spatially dependent heat source terms are considered. Boundary conditions of first, second and third kinds to the temperature at the inner and outer surfaces are obtained from an appropriate choice of parameters. The biological model is further enhanced by introducing an important thermoregulation mechanism, namely, the temperature dependent metabolic heat rate.

The analytical solution is not only essential to understand the underlying physics but also the underlying biology associated with thermal medicine problems. Our primary goal, however, is to develop target-specific models that take advantage of numerical methods based on approximation and iterative techniques to solve the governing equations of biological systems that are too complex for analytical methods. For this

reason, numerical models are the base of engineering analysis software. In this thesis, image segmentation and modeling simulation software are used to optimize target-specific non-invasive microwave antennas. Two examples are explored both using antennas in the passive mode for radiometric detection of brain temperature and in the active mode for microwave heating in pre-clinical investigations of bladder hyperthermia.

In Chapter 3, we develop a microwave radiometric sensor for rapid non-invasive feedback of critically important brain temperature during extended surgery of hypothermic patients. The key element of the sensor is a tapered log-spiral antenna. Its design and operating frequency band are optimized based on: i) maximizing the ratio of power received by the radiometric antenna from the target (brain); ii) maximizing frequency bandwidth and impedance match to tissue; and iii) minimizing overlap with typically noisy wireless communications frequencies. To demonstrate performance of the device, we build a realistic phantom model of the human head with separate brain and scalp regions consisting of tissue equivalent liquids circulating at independent temperatures on either side of an intact skull. This life size model of the human head allows simulation of differential surface and deep tissue temperatures. This way, brain temperature is independent from scalp temperature and operating room temperatures, which allows evaluating the sensor sensitivity from changes that occur only in the brain.

In Chapter 4, a new electro-thermo-fluid model is developed and incorporates a temperature-based optimization of murine bladder heating with a water-cooled microwave applicator. We incorporate tissue-specific biological data and use tissue-specific constitutive relationships for blood perfusion and metabolism. These relationships include the inherent temperature dependence of biological properties and account for the impaired thermoregulation due to anesthesia. Accurate environmental conditions are also included in the multiphysics model. The antenna includes a water bolus with controlled temperature to avoid overheating skin. The temperature-based optimization is designed to optimize the input antenna power as well as the temperature of the fluid entering the waveguide to heat the target in the interval [42, 43] °C while sparing the surrounding regions from temperatures higher than 42 °C.

Finally, Chapter 5 presents the concluding remarks and summarizes the main contributions as conclusions presented in detail in each research chapter. Some research works are being finished for further submission to scientific journals.

References

1. Shafirstein G, Feng Y: The role of mathematical modelling in thermal medicine. International Journal of Hyperthermia 2013, 29(4):259-261.

2. Stauffer PR: Evolving technology for thermal therapy of cancer. International Journal of Hyperthermia 2005, 21(8):731-744.

3. Salahi S, Maccarini PF, Rodrigues DB, Etienne W, Landon CD, Inman BA, Dewhirst MW, Stauffer PR: Miniature microwave applicator for murine bladder hyperthermia studies. International Journal of Hyperthermia 2012, 28(5):456-465.

4. Stauffer PR, Snow BW, Rodrigues DB, Salahi S, Oliveira TR, Reudink D, Maccarini PF: Non-Invasive Core Temperature Measurement in Brain: Demonstration in a Head Phantom and Initial Clinical Experience. The Neuroradiology Journal 2013, Submitted.

5. Kennedy JE: High-intensity focused ultrasound in the treatment of solid tumours. Nature Reviews Cancer 2005, 5(4):321-327.

6. El-Sayed IH, Huang X, El-Sayed MA: Selective laser photo-thermal therapy of epithelial carcinoma using anti-EGFR antibody conjugated gold nanoparticles. Cancer Letters 2006, 239(1):129-135.

7. Mehdizadeh M: Microwave/RF Applicators and Probes for Material Heating, Sensing, and Plasma Generation: A Design Guide. Burlington MA, USA: Elsevier; 2010.

8. Gemio J, Parron J, Soler J: Human body effects on implantable antennas for ISM bands applications: models comparison and propagation losses study. Progress in Electromagnetics Research-Pier 2010, 110:437-452.

9. Rodrigues DB, Salahi S, Pereira PJS, Limão-Vieira P, Landon CD, Oliveira TR, Etienne W, Inman BA, Dewhirst MW, Stauffer PR et al: Target-specific multiphysics model for murine bladder heating studies. Physics in Medicine and Biology 2013, Submitted.

10. Lazebnik M, Popovic D, McCartney L, Watkins CB, Lindstrom MJ, Harter J, Sewall S, Ogilvie T, Magliocco A, Breslin TM et al: A large-scale study of the ultrawideband microwave dielectric properties of normal, benign and malignant breast tissues obtained from cancer surgeries. Physics in Medicine and Biology 2007, 52(20):6093-6115.

11. Leroy Y, Bocquet B, Momouni A: Non-invasive microwave radiometry thermometry. Physiol Measurements 1998, 19(127-48).

12. Pozar DM: Microwave Engineering, 2nd edn. New York: John Wiley & sons, Inc.; 1998.

13. Balanis CA: Antenna Theory: Analysis and Design, 3 edn. Hoboken, New Jersey: John Wiley & Sons, Inc.; 2005.

14. Schanda E: Passive Microwave Sensing in Remote Sensing for Environmental Sciences. Berlin, Germany: Springer-Verlag; 1976.

15. Spencer RW, Christy JR: Precise monitoring of global temperature trends from satellites. Science 1990, 247(4950):1558-1562.

16. Kerr YH, Waldteufel P, Wigneron JP, Martinuzzi JM, Font J, Berger M: Soil moisture retrieval from space: The Soil Moisture and Ocean Salinity (SMOS) mission. Ieee Transactions on Geoscience and Remote Sensing 2001, 39(8):1729-1735.

17. Bardati F, Iudicello S: Modeling the visibility of breast malignancy by a microwave radiometer. IEEE Trans Biomed Eng 2008, 55(1):214-221.

18. Camart JC, Despretz D, Prevost B, Sozanski JP, Chive M, Pribetich J: New 434 MHz interstitial hyperthermia system monitored by microwave radiometry: theoretical and experimental results. International Journal of Hyperthermia 2000, 16(2):95-111.

19. Dubois L, Sozanski JP, Tessier V, Camart JC, Fabre JJ, Pribetich J, Chive M: Temperature control and thermal dosimetry by microwave radiometry in hyperthermia. IEEE Trans Microw Theory Tech (USA) 1996, 44(10, pt.2):1755-1761.

20. Jacobsen S, Stauffer PR: Can we settle with single-band radiometric temperature monitoring during hyperthermia treatment of chestwall recurrence of breast cancer using a dual-mode transceiving applicator? Phys Med Biol 2007, 52(4):911-928.

21. Stauffer PR, Jacobsen S, Neuman D: Microwave array applicator for radiometry controlled superficial hyperthermia. In: Thermal Treatment of Tissue: Energy Delivery and Assessment. Edited by Ryan TP, vol. 4247. San Jose: Proceedings of SPIE; 2001: 19-29.

22. Wang SS, VanderBrink BA, Regan J, Carr K, Link MS, Homoud MK, Foote CM, Estes NA, 3rd, Wang PJ: Microwave radiometric thermometry and its potential applicability to ablative therapy. J Interv Card Electrophysiol 2000, 4(1):295-300.

23. Hand JW, Van Leeuwen GMJ, Mizushina S, Van De Kamer JB, Maruyama K, Sugiura T, Azzopardi DV, Edwards AD: Monitoring of deep brain temperature in infants using multi-frequency microwave radiometry and thermal modelling. Phys Med Biol (UK) 2001, 46(7):1885-1903.

24. Maruyma K, Mizushina S, Sugiura T, Van Leeuwen GMJ, Hand JW, Marrocco G, Bardati F, Edwards AD, Azzopardi D, Land D: Feasibility of noninvasive measurement of deep brain temperature in newborn infants by multifrequency microwave radiometry. IEEE Trans Microw Theory Tech (USA) 2000, 48(11, pt.2):2141-2147.

25. Oikonomou A, Karanasiou IS, Uzunoglu NK: Phased-array near field radiometry for brain intracranial applications. Progress in Electromagnetics Research-Pier 2010, 109:345-360.

26. Arunachalam K, Maccarini P, De Luca V, Bardati F, Snow B, Stauffer P: Modeling the detectability of vesicoureteral reflux using microwave radiometry. Phys Med Biol 2010, 55(18):5417-5435.

27. Snow BW, Arunachalam K, De Luca V, Maccarini PF, Klemetsen O, Birkelund Y, Pysher TJ, Stauffer PR: Non-invasive vesicoureteral reflux detection: Heating risk studies for a new device. Journal of Pediatric Urology 2011, 7(6).

28. Stauffer P, Maccarini P, Arunachalam K, Salahi S, De Luca V, Boico A, Klemetsen O, Birkelund Y, Jacobsen S, Bardati F et al: Microwave Radiometry for Non-Invasive Detection of Vesicoureteral Reflux (VUR) Following Bladder Warming In: Proc of SPIE: Edited by Ryan T. SPIE Press, Bellingham WA 2011 PMCID:3409575: 7901OV-7901-7911.

29. Arunachalam K, Maccarini P, De Luca V, Tognolatti P, Bardati F, Snow B, Stauffer P: Detection of vesicoureteral reflux using microwave radiometry-system characterization with tissue phantoms. IEEE Trans Biomed Eng 2011, 58(6):1629-1636.

30. Rodrigues DB, Maccarini PF, Salahi S, Colebeck E, Topsakal E, Pereira PJS, Limao-Vieira P, Stauffer PR: Numerical 3D modeling of heat transfer in human tissues for microwave radiometry monitoring of brown fat metabolism. In: Conference on Energy-Based Treatment of Tissue and Assessment VII: Feb 3-4 2013; San Francisco, CA. SPIE.

31. Jacobsen S, Birkelund Y: Improved resolution and reduced clutter in ultra-wideband microwave imaging using cross-correlated back projection: experimental and numerical results. International journal of biomedical imaging 2010, 2010.

32. Rodrigues DB, Maccarini PF, Salahi S, Oliveira TO, Pereira PJS, Limao-Vieira P, Snow BW, Reudink D, Stauffer PR: Design and optimization of an ultra-wideband and compact microwave antenna for radiometric monitoring of brain temperature. IEEE Transactions on Biomedical Engineering 2013, Submitted.

33. Arunachalam K, Stauffer PR, Maccarini PF, Jacobsen S, Sterzer F: Characterization of a digital microwave radiometry system for noninvasive thermometry using a temperature-controlled homogeneous test load. Physics in Medicine & Biology 2008, 53(14):3883-3901.

34. Klemetsen O, Birkelund Y, Maccarini PF, Stauffer P, Jacobsen SK, Electromagnet A: Design of Small-sized and Low-cost Front End to Medical Microwave Radiometer. Piers 2010 Cambridge: Progress in Electromagnetics Research Symposium Proceedings, Vols 1 and 2 2010:932-936.

35. Klemetsen O, Birkelund Y, Jacobsen SK, Maccarini PF, Stauffer PR: Design of Medical Radiometer Front-End for Improved Performance. Prog Electromagn Res B Pier B 2011, 27:289-306.

36. Schildkopf P, Ott OJ, Frey B, Wadepohl M, Sauer R, Fietkau R, Gaipl US: Biological Rationales and Clinical Applications of Temperature Controlled

Hyperthermia - Implications for Multimodal Cancer Treatments. Current Medicinal Chemistry 2010, 17(27):3045-3057.

37. Hildebrandt B, Wust P, Ahlers O, Dieing A, Sreenivasa G, Kerner T, Felix R, Riess H: The cellular and molecular basis of hyperthermia. Critical Reviews in Oncology Hematology 2002, 43(1):33-56.

38. Pearce JA: Comparative analysis of mathematical models of cell death and thermal damage processes. International Journal of Hyperthermia 2013, 29(4):262-280.

39. Vujaskovic Z, Craciunescu O, Stauffer P, Carroll M, Lan L, Dewhirst M, Inman B: Pilot study of external hyperthermia and intravesical mitomycin-C to treat recurrent bladder cancer after failed standard therapy. In: ASCO Annual Meeting: 2010. Journal of Clinical Oncology.

40. Needham D, Anyarambhatla G, Kong G, Dewhirst MW: A new temperature-sensitive liposome for use with mild hyperthermia: Characterization and testing in a human tumor xenograft model. Cancer Research 2000, 60(5):1197-1201.

41. Ponce AM, Vujaskovic Z, Yuan F, Needham D, Dewhirst MW: Hyperthermia mediated liposomal drug delivery. International Journal of Hyperthermia 2006, 22(3):205-213.

42. Pankhurst QA, Connolly J, Jones SK, Dobson J: Applications of magnetic nanoparticles in biomedicine. Journal of Physics D-Applied Physics 2003, 36(13):R167-R181.

43. Rodrigues DB, Pereira PJS, Limão-Vieira P, Stauffer PR, Maccarini PF: Study of the one dimensional and transient bioheat transfer equation: Multi-layer solution development and applications. International Journal of Heat and Mass Transfer 2013, 62:153-162.

44. Thiesen B, Jordan A: Clinical applications of magnetic nanoparticles for hyperthermia. International Journal of Hyperthermia 2008, 24(6):467-474.

45. Peer AJ, Grimm MJ, Zynda ER, Repasky EA: Diverse immune mechanisms may contribute to the survival benefit seen in cancer patients receiving hyperthermia. Immunologic Research 2010, 46(1-3):137-154.

46. Shen RN, Lu L, Young P, Shidnia H, Hornback NB, Broxmeyer HE: Influence of elevated-temperature on natural-killer-cell activity, lymphokine-activated killer-cell activity and lectin-dependent cytotoxicity of human umbilical-cord blood and adult-blood cells. International Journal of Radiation Oncology Biology Physics 1994, 29(4):821-826.

47. Horsman MR, Overgaard J: Hyperthermia: a potent enhancer of radiotherapy. Clinical Oncology 2007, 19(6):418-426.

48. Frey B, Weiss E-M, Rubner Y, Wunderlich R, Ott OJ, Sauer R, Fietkau R, Gaipl US: Old and new facts about hyperthermia-induced modulations of the immune system. International Journal of Hyperthermia 2012, 28(6):528-542.

49. Jayasundar R, Hall ED, Bleehen NM: Magnetic resonance, hyperthermia and oncology. Current Science 1999, 76(6):794-799.

50. Ahlbom A, Bergqvist U, Bernhardt JH, Cesarini JP, Court LA, Grandofo M, Hietanen M, McKinlay AF, Repacholi MH, Sliney DH et al: Guidelines for limiting exposure to time-varying electric, magnetic, and electromagnetic fields (up to 300 GHz) (vol 74, pg 494, 1998). Health Physics 1998, 75(4):442-442.

51. McGraw-Hill: McGraw-Hill Concise Encyclopedia of Bioscience vol. 1: McGraw-Hill Professional; 2004.

52. Stauffer PR, Rodrigues DB, Salahi S, Topsakal E, Ribeiro TO, Prakash A, Maccarini PF: Stable microwave radiometry system for long term monitoring of deep tissue temperature. In: Conference on Energy-Based Treatment of Tissue and Assessment VII: 2013; San Jose CA, USA. SPIE.

53. Lazebnik M, Madsen EL, Frank GR, Hagness SC: Tissue-mimicking phantom materials for narrowband and ultrawideband microwave applications. Physics in Medicine and Biology 2005, 50(18):4245-4258.

54. Madsen EL, Hobson MA, Shi HR, Varghese T, Frank GR: Tissue-mimicking agar/gelatin materials for use in heterogeneous elastography phantoms. Physics in Medicine and Biology 2005, 50(23):5597-5618.

55. Datta A, Rakesh V: An Introduction to Modeling of Transport Processes: Applications to Biomedical Systems: Cambridge University Press; 2009.

Chapter 2

Study of the one dimensional and transient bioheat transfer equation: multi-layer solution development and applications

Abstract

In this work we derive an analytical solution given by Bessel series to the transient and one-dimensional (1D) bioheat transfer equation in a multi-layer region with spatially dependent heat sources. Each region represents an independent biological tissue characterized by temperature-invariant physiological parameters and a linearly temperature dependent metabolic heat generation. Moreover, 1D Cartesian, cylindrical or spherical coordinates are used to define the geometry and temperature boundary conditions of first, second and third kinds are assumed at the inner and outer surfaces. We present two examples of clinical applications for the developed solution. In the first one, we investigate two different heat source terms to simulate the heating in a tumor and its surrounding tissue, induced during a magnetic fluid hyperthermia technique used for cancer treatment. To obtain an accurate analytical solution, we determine the error associated with the truncated Bessel series that defines the transient solution. In the second application, we explore the potential of this model to study the effect of different environmental conditions in a multi-layered human head model (brain, bone and scalp). The convective heat transfer effect of a large blood vessel located inside the brain is also investigated. The results are further compared with a numerical solution obtained by the Finite Element Method and computed with COMSOL Multiphysics v4.1.

Keywords: Bioheat transfer equation; Method of separation of variables; Eigenfunctions and eigenvalues; Bessel functions; Finite element method; Hyperthermia applications.

CHAPTER 2

This chapter addresses research work carried out on the studies of the one dimensional and transient bioheat transfer equation that have been published as follows:

1. **Rodrigues DB**, Pereira PJS, Limão-Vieira P, Stauffer PR, Maccarini PF: Study of the one dimensional and transient bioheat transfer equation: Multi-layer solution development and applications. International Journal of Heat and Mass Transfer 2013, 62:153-162.
2. **Rodrigues DB**, Pereira PJS, Limão-Vieira PM, Maccarini PF: Analytical Solution to the Transient 1D Bioheat Equation in a Multi-layer Region with Spatial Dependent Heat Sources. In The Eighth IASTED International Conference on Biomedical Engineering; Innsbruck. Edited by Press A. 2011:96-103.

Nomenclature

i	tissue layer index	ρ_i	mass density (kg/m^3)
r^*	spatial coordinate (m)	c_i	specific heat capacity (J/kg/K)
t^*	time (s)	k_i	thermal conductivity (W/m/K)
T_i^*	temperature (K)	ω_{bi}	blood perfusion (1/s)
T_{0i}^*	initial temperature (K)	ρ_b	mass density of blood (kg/m^3)
T_a^*	arterial blood temperature (K)	c_b	specific heat capacity of blood (J/kg/K)
P_i^*	internal heat generation (W/m^3)	Q_{mi}^*	metabolic heat generation (W/m^3)

2.1. Introduction

The heat transfer in living tissues, known as bioheat transfer, is a complex phenomenon that depends on the thermodynamics of the biological system, its thermal constitutive parameters and the thermal response to external stimulus, e.g., electromagnetic or ultrasonic waves used in cancer treatments [1-4].

The study of bioheat transfer is especially relevant to the field of thermal medicine, since experimental temperature data is not extensively available. Temperature measurement techniques are mostly invasive as well as expensive and provide a limited number of measurement points. Non-invasive temperature measurement techniques, such as magnetic resonance thermal imaging, allow volumetric temperature measurements. However, they are limited due to its high cost and low thermal resolution [3, 5].

Several therapeutic applications based on the knowledge of bioheat transfer involve either raising or lowering temperature from normal body temperature, namely, hyperthermia [1-3] and hypothermia [4], respectively. Hyperthermia may be defined as raising the temperature of a certain region of the body above normal for a defined period of time, usually between 30 and 90 minutes [1]. The most common techniques to induce hyperthermia are based on heat deposition from electromagnetic [3, 5] or ultrasound sources [2], where the biological tissues convert the absorbed energy into heat causing a temperature increase. Another approach to heat generation involves injecting magnetic nanoparticles immersed in fluid into the target tissue to absorb energy at a higher rate than the surrounding tissue from an externally applied electromagnetic field [6-9]. This technique is known as magnetic fluid hyperthermia (MFH).

CHAPTER 2

The efficacy of hyperthermia for cancer therapy is dependent on the delivery of well-controlled moderate heating (approximately 42 ^{o}C) to the entire tumor volume without overheating the surrounding critical normal tissues [3, 10]. This technique takes advantage of the rapid neoplastic cell growth, which makes it more sensitive to an increase of temperature [11]. To optimize new hyperthermia based procedures, it is essential to develop a simplified but accurate model to estimate the temperature distribution and highlight the overall effect of the various parameters.

In 1948, Pennes was the first to propose and validate experimentally an analytical bioheat transfer model with a heat loss term due to blood perfusion [12]. Besides perfusion, Pennes' model also accounted for thermal storage, heat conduction and heat generation caused by internal and/or external sources. Other accurate bioheat transfer models have been suggested [13, 14]. However, Pennes' model is the most widely used because of its simplicity and acceptable accuracy if no large thermally significant blood vessels are close to the analyzed heated region [12, 13].

Solutions of the Pennes' bioheat equation were obtained in regions with Cartesian, cylindrical and spherical geometries [6-8, 15-18]. Durkee *et al.* derived an analytical solution of the classical bioheat equation using eigenfunctions for spherical and Cartesian coordinates [15] as well as cylindrical coordinates [16]. In both cases, a constant heat source term was used. In reference [17] Durkee *et al.* used Green functions to solve the classical bioheat equation for time dependent sources. Continuity boundary conditions to the temperature and heat flow were imposed at the interfaces. Moreover, Neumann and Robin boundary conditions at the inner and outer surfaces were assumed, respectively.

Bagaria and Johnson [7] used the method of separation of variables to obtain a transient and 1D solution to estimate the temperature in two concentric spherical regions. They assumed that the tumor was located in the inner region containing magnetic nanoparticles only with a polynomial distribution. On the other hand, a source term described by an exponential function was validated experimentally by Salloum *et al.* [9].

The purpose of this work is to derive an analytical solution to the transient and one-dimensional Pennes' bioheat equation in a multi-layer region with generic spatially dependent heat sources. Each region represents an independent biological tissue (e.g., skin, fat or muscle) characterized by temperature-invariant physiological parameters and

linearly temperature dependent metabolic heat generation. Moreover, 1D Cartesian, cylindrical or spherical coordinates are used to define the geometry and continuity boundary conditions are imposed to the temperature and heat flow between adjacent layers. The inner and outer surfaces satisfy equations with adaptable parameters that allow one to define Dirichlet, Neumann and/or Robin boundary conditions.

This bioheat transfer model, which makes use of a formalism previously described by Rodrigues *et al.* [19], is applied to obtain the theoretical temperature profiles in the tumor bed and surrounding healthy tissue using two spatially dependent heat source terms to simulate a MFH treatment. We further explore the potential of this model to study the effect of different environmental conditions in a multi-layered human head model (brain, bone and scalp). The convective effect of a large blood vessel located inside the brain is also investigated assuming a laminar and fully thermally developed blood flow.

Furthermore, we use two approaches to validate the analytical solution. In the first one, we determine the error associated with the truncated Bessel series that defines the transient solution whereas in the second one we compare the analytical and numerical solutions. These numerical solutions are obtained using the Finite Element Method (FEM) and computed with COMSOL Multiphysics v4.1.

2.2. Mathematical formulation

2.2.1. Pennes bioheat transfer equation

The bioheat transfer equation in a multi-layer region is given by

$$\rho_i c_i \frac{\partial T_i^*}{\partial t^*}\left(r^*,t^*\right) = k_i \nabla^2 T_i^*\left(r^*,t^*\right) + \omega_{bi}\rho_b c_b\left(T_a^* - T_i^*\left(r^*,t^*\right)\right) + Q_{mi}^*\left(r^*,t^*\right) + P_i^*\left(r^*\right) \tag{1}$$

where

$$\nabla^2 T_i^*\left(r^*,t^*\right) = \frac{1}{r^{*G}}\frac{\partial}{\partial r^*}\left(r^{*G}\frac{\partial T_i^*}{\partial r^*}\left(r^*,t^*\right)\right) \tag{2}$$

$$Q_{mi}^*\left(r^*,t^*\right) = Q_{m0i}^* + Q_{msi}^* T_i^*\left(r^*,t^*\right) \tag{3}$$

with $1 \le i \le n$, $r_{i-1}^* \le r^* \le r_i^*$ ($n \in \mathbb{N}$) and G = 0, 1 and 2 for problems with 1D Cartesian, cylindrical and spherical symmetric geometries, respectively. Note that the

mathematical method prescribed here works for a constant $(Q^*_{mi} = Q^*_{m0i})$ or linearly temperature dependent metabolic heat generation given by (3) with a slope denoted by Q^*_{msi} [20].

The tissue temperature described by (1) is controlled by heat storage $(\rho_i c_i (\partial T_i^* / \partial t^*))$, thermal conduction $(k_i \nabla^2 T_i^*)$, dissipation of heat through blood flow $(\omega_{bi} \rho_b c_b (T_a^* - T_i^*))$ and heat generation (P_i^*), which represents the contribution from volumetric heat generation, converted from some other form of energy such as electromagnetic, ultrasonic or other modes of heating. Metabolic heat generation (Q^*_{mi}) is another type of heat input resulting from biochemical conversion of energy within tissue [11, 12].

As example, a region with *n* layers and a spherically symmetric geometry is presented in Figure 2.1. These layers correspond to biological tissues (e.g., skin, fat and muscle) and r_0^* can be equal to zero or $r_0^* > 0$ m to take into account air or liquid body regions as well as catheters like those used in transurethral prostatic microwave thermotherapy [21].

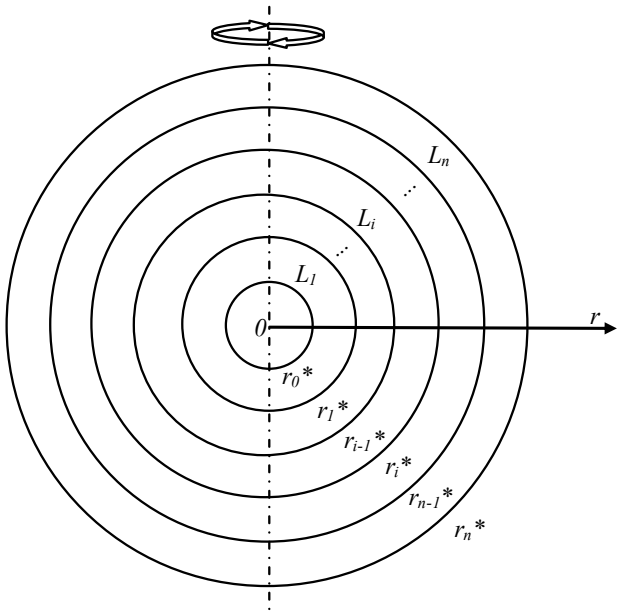

Figure 2.1 – Cross section of a region with *n* layers and a spherical symmetric geometry (L_i - i^{th} tissue layer).

2.2.2. Boundary and initial conditions

Boundary conditions of first, second and third kinds to the temperature at the inner and outer surfaces are assumed (see (4) and (5)). Temperature and heat flow must satisfy continuity boundary conditions at the tissue interfaces (see (6)-(9)). An initial spatially dependent temperature is also considered (see (10)).

- Inner surface of 1st layer ($i = 1$)

(4) $$A_{in}^{*}\frac{\partial T_1^{*}}{\partial r^{*}}\left(r_0^{*},t^{*}\right)+B_{in}^{*}T_1^{*}\left(r_0^{*},t^{*}\right)=C_{in}^{*}$$

- Outer surface of n^{th} layer $(i = n)$

(5) $$A_{out}^{*}\frac{\partial T_n^{*}}{\partial r^{*}}\left(r_n^{*},t^{*}\right)+B_{out}^{*}T_n^{*}\left(r_n^{*},t^{*}\right)=C_{out}^{*}$$

- Inner interface of i^{th} layer $(i \neq 1)$

(6) $$T_i^{*}\left(r_{i-1}^{*},t^{*}\right)=T_{i-1}^{*}\left(r_{i-1}^{*},t^{*}\right)$$

(7) $$k_i\frac{\partial T_i^{*}}{\partial r^{*}}\left(r_{i-1}^{*},t^{*}\right)=k_{i-1}\frac{\partial T_{i-1}^{*}}{\partial r^{*}}\left(r_{i-1}^{*},t^{*}\right)$$

- Outer interface of i^{th} layer $(i \neq n)$

(8) $$T_i^{*}\left(r_i^{*},t^{*}\right)=T_{i+1}^{*}\left(r_i^{*},t^{*}\right)$$

(9) $$k_i\frac{\partial T_i^{*}}{\partial r^{*}}\left(r_i^{*},t^{*}\right)=k_{i+1}\frac{\partial T_{i+1}^{*}}{\partial r^{*}}\left(r_i^{*},t^{*}\right)$$

- Initial condition

(10) $$T_i^{*}\left(r^{*},t^{*}=0\right)=T_{0i}^{*}\left(r^{*}\right)$$

Note that parameters in (4) and (5) can be chosen in order to obtain Dirichlet, Neumann or Robin boundary conditions.

2.2.3. Solution methodology

To obtain the dimensionless bioheat transfer equation the following relations are introduced:

(11) $$T_i\left(r,t\right)=\frac{T_i^*\left(r,t\right)-T_{r0}^*}{T_{r0}^*}$$

(12) $$r=\frac{r^*}{r_n^*}$$

(13) $$t=t^*\omega_{bm}$$

where ω_{bm} is the average perfusion rate within all tissue layers and T_{r0}^* is the initial reference temperature given by

(14) $$T_{r0}^*=\frac{1}{n}\sum_{i=1}^{n}\frac{1}{r_i^*-r_{i-1}^*}\int_{r_{i-1}^*}^{r_i^*}T_{0i}^*\left(r^*\right)dr^*$$

Thus, one can obtain the following equation:

(15) $$\frac{\partial T_i}{\partial t}\left(r,t\right)=\ \alpha_i\nabla^2T_i\left(r,t\right)-\ \beta_iT_i\left(r,t\right)+\sigma_i\left(r\right)$$

with

(16) $$\alpha_i=\frac{k_i}{\rho_ic_i\omega_{bm}\left(r_n^*\right)^2}$$

(17) $$\beta_i=\frac{\rho_bc_b\omega_{bi}-Q_{msi}^*}{\rho_ic_i\omega_{bm}}$$

(18) $$\sigma_i\left(r\right)=\frac{\omega_{bi}\rho_bc_b\left(T_a^*-T_{r0}^*\right)+\ Q_{m0i}^*+Q_{msi}^*T_{r0}^*+\ P_i^*\left(r\right)}{\rho_ic_i\omega_{bm}T_{r0}^*}$$

To solve (15) by the method of separation of variables, the solution of this nonhomogeneous equation is decomposed in two components as follows:

(19) $$T_i\left(r,t\right)=\bar{T}_i\left(r,t\right)+\hat{T}_i\left(r\right)$$

where $\bar{T}_i$ and $\hat{T}_i$ are the transient (homogeneous) and steady state (nonhomogeneous) components, respectively. Note that this analytical method works for linear and homogeneous equations with constant coefficients (see (20)). Thus, we have

(20) $$\frac{\partial \bar{T}_i}{\partial t}\left(r,t\right)=\ \alpha_i\nabla^2\bar{T}_i\left(r,t\right)-\ \beta_i\bar{T}_i\left(r,t\right)$$

(21) $$\alpha_i\nabla^2\hat{T}_i\left(r\right)-\ \beta_i\hat{T}_i\left(r\right)=-\ \sigma_i\left(r\right)$$

2.2.4. Boundary and initial conditions to the transient and steady state problems

The boundary and initial conditions to the transient and steady state equations (see (20) and (21)) can be obtained using (4)-(10) and (19) as well as a dimensionless analysis giving:

- Inner surface of 1st layer $(i=1)$

(22) $$A_{in}\frac{\partial \overline{T}_1}{\partial r}(r_0,t)+B_{in}\overline{T}_1(r_0,t)=0$$

(23) $$A_{in}\frac{d\hat{T}_1}{dr}(r_0)+B_{in}\hat{T}_1(r_0)=C_{in}$$

- Outer surface of n^{th} layer $(i=n)$

(24) $$A_{out}\left(\frac{\partial \overline{T}_n}{\partial r}\right)_{r=r_n}+B_{out}\overline{T}_n(r_n,t)=0$$

(25) $$A_{out}\left(\frac{d\hat{T}_n}{dr}\right)_{r=r_n}+B_{out}\hat{T}_n(r_n)=C_{out}$$

- Inner interface of i^{th} layer $(i\neq 1)$

(26) $$\overline{T}_i(r_{i-1},t)=\overline{T}_{i-1}(r_{i-1},t)$$

(27) $$\hat{T}_i(r_{i-1})=\hat{T}_{i-1}(r_{i-1})$$

(28) $$k_i\left(\frac{\partial \overline{T}_i}{\partial r}\right)_{r=r_{i-1}}=k_{i-1}\left(\frac{\partial \overline{T}_{i-1}}{\partial r}\right)_{r=r_{i-1}}$$

(29) $$k_i\left(\frac{d\hat{T}_i}{dr}\right)_{r=r_{i-1}}=k_{i-1}\left(\frac{d\hat{T}_{i-1}}{dr}\right)_{r=r_{i-1}}$$

- Outer interface of i^{th} layer $(i\neq n)$

(30) $$\overline{T}_i(r_i,t)=\overline{T}_{i+1}(r_i,t)$$

(31) $$\hat{T}_i(r_i)=\hat{T}_{i+1}(r_i)$$

(32) $$k_i\left(\frac{\partial \overline{T}_i}{\partial r}\right)_{r=r_i}=k_{i+1}\left(\frac{\partial \overline{T}_{i+1}}{\partial r}\right)_{r=r_i}$$

(33) $$k_i\left(\frac{d\hat{T}_i}{dr}\right)_{r=r_i}=k_{i+1}\left(\frac{d\hat{T}_{i+1}}{dr}\right)_{r=r_i}$$

- Initial condition to the transient component

(34) $$\bar{T}_i\left(r,t=0\right)=T_{0i}\left(r\right)-\hat{T}_i\left(r\right)$$

where

(35) $$A_{in}=1;\ B_{in}=\frac{B_{in}^{*}\ r_n^{*}}{A_{in}^{*}};\ C_{in}=\frac{C_{in}^{*}\ r_n^{*}}{A_{in}^{*}T_{r0}^{*}}-B_{in}$$

(36) $$A_{out}=1\ ;B_{out}=\frac{B_{out}^{*}\ r_n^{*}}{A_{out}^{*}};\ C_{out}=\frac{C_{out}^{*}\ r_n^{*}}{A_{out}^{*}T_{r0}^{*}}-B_{out}$$

(37) $$T_{0i}\left(r\right)=\frac{T_{0i}^{*}\left(r\right)-T_{r0}^{*}}{T_{r0}^{*}}$$

2.2.5. Analytical solution to the steady state problem

2.2.5.1. Generic solution to the steady state equation

The solution of the linear and nonhomogeneous ordinary differential equation (21) is given by:

(38) $$\hat{T}_i\left(r\right)=H_i\left(r\right)+S_i\left(r\right)$$

where H_i is the solution of the homogeneous equation,

(39) $$\alpha_i\nabla^2 H_i\left(r\right)-\beta_i H_i\left(r\right)=0$$

and S_i is the particular integral of (21).

Solving equation (39), one can obtain

(40) $$H_i\left(r\right)=u_i r^{-\varepsilon(G)}I_{\varepsilon(G)}\left(\gamma_i r\right)+v_i r^{-\varepsilon(G)}K_{\varepsilon(G)}\left(\gamma_i r\right)$$

where $\gamma_i = Im\left(\sqrt{-\beta_i/\alpha_i}\right)$ when $\beta_i > 0$ or $\gamma_i = \sqrt{-\beta_i/\alpha_i}$ when $\beta_i \leq 0$ and $\alpha_i > 0$ as well as $\varepsilon(G) = (G-1)/2$. Note that $Im(z)$ denotes the imaginary part of the complex number z.

In equation (40), u_i and v_i are unknown coefficients and $I_{\varepsilon(G)}$ as well as $K_{\varepsilon(G)}$ are modified Bessel functions of the first and second kinds, respectively. Moreover, the order of these modified Bessel functions is denoted by $\varepsilon(G)$ and given by -1/2, 0 and 1/2 for Cartesian, cylindrical and spherical coordinates, respectively.

One can show in a straightforward manner the following relationship:

$$I_{\varepsilon(G)}(\gamma_i r)\frac{dK_{\varepsilon(G)}}{dr}(\gamma_i r)-K_{\varepsilon(G)}(\gamma_i r)\frac{dI_{\varepsilon(G)}}{dr}(\gamma_i r)=-\frac{1}{r} \tag{41}$$

Using (21), (38), (40) and (41) as well as the method of variation of parameters the particular integral S_i is given by

$$S_i(r)=\frac{r^{-\varepsilon(G)}K_{\varepsilon(G)}(\gamma_i r)}{\alpha_i}\int r^{\varepsilon(G)+1}I_{\varepsilon(G)}(\gamma_i r)\sigma_i(r)dr- \frac{r^{-\varepsilon(G)}I_{\varepsilon(G)}(\gamma_i r)}{\alpha_i}\int r^{\varepsilon(G)+1}K_{\varepsilon(G)}(\gamma_i r)\sigma_i(r)dr \tag{42}$$

2.2.5.2. Calculation of the unknown coefficients u_i and v_i

The function $\hat{T}_i$ satisfies a system of 2*n* equations described by the boundary conditions (23), (25), (27), (29), (31) and (33). This way, the following matricial system is deduced:

$$\begin{bmatrix} u_1 \\ \cdots \\ v_i \\ u_{i+1} \\ \cdots \\ v_n \end{bmatrix} = \begin{bmatrix} \hat{c}_1 & \hat{c}_2 & \cdots & 0 & 0 & 0 & 0 & \cdots & 0 & 0 \\ \cdots & \cdots & \cdots & \cdots & \cdots & \cdots & \cdots & \cdots & \cdots & \cdots \\ 0 & 0 & \cdots & \hat{\phi}_{i1} & \hat{\phi}_{i2} & \hat{\phi}_{i3} & \hat{\phi}_{i4} & \cdots & 0 & 0 \\ 0 & 0 & \cdots & \hat{\omega}_{i1} & \hat{\omega}_{i2} & \hat{\omega}_{i3} & \hat{\omega}_{i4} & \cdots & 0 & 0 \\ \cdots & \cdots & \cdots & \cdots & \cdots & \cdots & \cdots & \cdots & \cdots & \cdots \\ 0 & 0 & \cdots & 0 & 0 & 0 & 0 & \cdots & \hat{c}_4 & \hat{c}_5 \end{bmatrix}^{-1} \begin{bmatrix} \hat{c}_3 \\ \cdots \\ \hat{\Phi}_i \\ \hat{\Omega}_i \\ \cdots \\ \hat{c}_6 \end{bmatrix} \tag{43}$$

where the coefficients of the matrices on the right hand side of (43) are presented in Appendix 2A. To solve this matricial system one can use, e.g., Maple software.

2.2.6. Analytical solution to the homogeneous transient problem

2.2.6.1. Method of separation of variables

To solve (20) by the method of separation of variables, one can assume the following relationship:

$$\overline{T}_i(r,t)=R_i(r)\Psi_i(t) \tag{44}$$

The functions R_i and Ψ_i satisfy the ordinary differential equations,

$$\alpha_i\nabla^2 R_i(r)+\lambda_i^2 R_i(r)=0 \tag{45}$$

(46) $$\frac{d\Psi_i(t)}{dt}+\left(\beta_i+\alpha_i\lambda_i^2\right)\Psi_i(t)=0$$

The solutions of (45) and (46) can be written as follows:

(47) $$R_{im}(r)=a_{im}r^{-\varepsilon(G)}J_{\varepsilon(G)}\left(\lambda_{im}r\right)+b_{im}r^{-\varepsilon(G)}Y_{\varepsilon(G)}\left(\lambda_{im}r\right)$$

(48) $$\Psi_{im}(t)=d_{im}\exp\left(-\left(\beta_i+\alpha_i\lambda_{im}^2\right)t\right)$$

where a_{im}, b_{im} and d_{im} are unknown coefficients and $-\lambda_{im}^2$ is a constant of separation. Note that $J_{\varepsilon(G)}$ and $Y_{\varepsilon(G)}$ are the Bessel functions of the first and second kinds, respectively.

Using the superposition principle the solution of the homogeneous transient equation is defined by

(49) $$\overline{T}_i(r,t)=\sum_{m=1}^{+\infty}R_{im}(r)\Psi_{im}(t)$$

2.2.6.2. Eigenvalue problem

One can prove that the transverse eigenfunction R_{im} satisfies the orthogonality condition

(50) $$\sum_{i=1}^{n}\frac{k_i}{\alpha_i^2}\int_{r_{i-1}}^{r_i}r^G R_{im}(r)R_{il}(r)dr=\begin{cases}0 & if\ m\neq l\\ N_m & if\ m=l\end{cases}$$

with

(51) $$N_m=\sum_{i=1}^{n}\frac{k_i}{\alpha_i^2}\int_{r_{i-1}}^{r_i}r^G R_{im}^2(r)dr$$

The proof of (50) is given in Appendix 2B. From (47) to (49) and the continuity boundary conditions (see (26), (28), (30) and (32)), one can show

(52) $$\lambda_{im}=\sqrt{\frac{\beta_1-\beta_i+\alpha_1\lambda_{1m}^2}{\alpha_i}}$$

(53) $$d_{im}=d_m$$

To determine the eigenvalues λ_{1m} a system of $2n$ equations is defined using the boundary conditions (22), (24), (26), (28), (30), (32) and (47)-(49). To obtain solutions other than the trivial solution, one must impose

$$\begin{vmatrix} \bar{c}_{1m} & \bar{c}_{2m} & \cdots & 0 & 0 & 0 & 0 & \cdots & 0 & 0 \\ \cdots & \cdots & \cdots & \cdots & \cdots & \cdots & \cdots & \cdots & \cdots & \cdots \\ 0 & 0 & \cdots & \bar{\phi}_{i1m} & \bar{\phi}_{i2m} & \bar{\phi}_{i3m} & \bar{\phi}_{i4m} & \cdots & 0 & 0 \\ 0 & 0 & \cdots & \bar{\omega}_{i1m} & \bar{\omega}_{i2m} & \bar{\omega}_{i3m} & \bar{\omega}_{i4m} & \cdots & 0 & 0 \\ \cdots & \cdots & \cdots & \cdots & \cdots & \cdots & \cdots & \cdots & \cdots & \cdots \\ 0 & 0 & \cdots & 0 & 0 & 0 & 0 & \cdots & \bar{c}_{4m} & \bar{c}_{5m} \end{vmatrix} = 0 \tag{54}$$

The coefficients of this determinant can be found in Appendix 2A. To calculate the eigenvalues the complex Newton method is used. The roots number of (54) is confirmed by the Cauchy's argument principle. To reduce the round-off errors all numerical calculations are made with double precision using Maple software.

2.2.6.3. Determination of the coefficients a_{im} and b_{im}

Using the eigenvalues calculated previously and the continuity boundary conditions to the temperature and heat flow (see (30) and (32)), one can establish the following recurrence formula to calculate the coefficients a_{im} and b_{im}:

$$\begin{bmatrix} a_{i+1,m} \\ b_{i+1,m} \end{bmatrix} = \begin{bmatrix} -\bar{\phi}_{i3m} & -\bar{\phi}_{i4m} \\ -\bar{\omega}_{i3m} & -\bar{\omega}_{i4m} \end{bmatrix}^{-1} \begin{bmatrix} \bar{\phi}_{i1m} & \bar{\phi}_{i2m} \\ \bar{\omega}_{i1m} & \bar{\omega}_{i2m} \end{bmatrix} \begin{bmatrix} a_{im} \\ b_{im} \end{bmatrix}, \text{ with } 1 \le i \le n-1 \tag{55}$$

From (22) and (47)-(49) the coefficients a_{1m} and b_{1m} are related by $b_{1m} = -\bar{c}_{1m} a_{1m} / \bar{c}_{2m}$. Note that a_{1m} is arbitrary but any two sets of eigenfunctions obtained with different values of a_{1m} are proportional to each other which are valid solutions to the eigenvalue problem. Furthermore, one does not need to consider a_{1m} in the transient solution since the coefficient d_m can be rewritten as $\tilde{d}_m = d_m a_{1m}$ (see (47)-(49) and (53)).

2.2.6.4. Determination of the coefficient d_m

To determine the layer invariant coefficient d_m the initial condition (34) and (50) are used giving

(56) $$d_m = \frac{1}{N_m}\sum_{i=1}^{n}\frac{k_i}{\alpha_i^2}\int_{r_{i-1}}^{r_i} r^G R_{im}(r)\left(T_{0i}(r)-\hat{T}_i(r)\right)\,dr$$

From (52) the eigenvalues can be real and/or complex numbers for a generic problem. Thus, one should consider the real part of T_i as a final and physically meaningful solution to the biological problem.

To obtain a time evanescent solution to the homogeneous and transient problem for any set of physiological parameters ($\alpha_i > 0$ and $\beta_i > 0$) and assuming real eigenvalues λ_{im}, we consider $-\lambda_{im}^2$ as a constant of separation (see (44)-(49) and (52)). Otherwise, if one chooses λ_{im}^2 as a constant of separation, a different branch structure for the eigenfunctions is obtained. In this case, slightly different forms of these equations are deduced giving

(57) $$R_{im}(r) = a_{im} r^{-\varepsilon(G)} I_{\varepsilon(G)}(\lambda_{im} r) + b_{im} r^{-\varepsilon(G)} K_{\varepsilon(G)}(\lambda_{im} r)$$

(58) $$\Psi_{im}(t) = d_{im}\exp\left(-\left(\beta_i - \alpha_i\lambda_{im}^2\right)\mathrm{t}\right)$$

The transient and homogeneous equation does not include a source term to supply energy for the biological system. Therefore, time evanescent solutions must be obtained. Note that (58) is not a time evanescent solution for any set of physiological parameters α_i and β_i.

2.3. Results and model validation

2.3.1. MFH technique with a polynomial heat source term

To optimize the transient and 1D temperature distribution in the tumor, a spatially dependent heat source term was considered by Bagaria and Johnson [7]. They assumed concentric spherical regions to the tumor and healthy tissue. Magnetic nanoparticles were contained in the inner region (tumor) to simulate a MFH cancer treatment with a source term described by the following polynomial equation:

(59) $$P_1^*\left(r^*\right) = Q_1^* + Q_2^* r^* + Q_3^* r^{*2}$$

To compare our results with those presented by Bagaria and Johnson, the following set of parameters is chosen as in [7]: ρ_1 =1100 kg/m^3, ρ_2 = 1000 kg/m^3, $c_1 = c_2 = c_b = 4200$

J/kg/K, $k_1 = 0.55$ W/m/K, $k_2 = 0.50$ W/m/K, $\rho_b \omega_{b1} = \rho_b \omega_{b2} = 1$ kg/m^3/s, $T_a^* = T_{r0}^* = 310$ K, $Q_{m1}^* = Q_{m2}^* = 0$ W/m^3, $Q_1^* = 1\times10^5$ W/m^3, $Q_2^* = 8\times10^7$ W/m^4, $Q_3^* = -7\times10^9$ W/m^5, $r_0^* = 0$ m, $r_1^* = 0.01$ m and $r_2^* = 0.04$ m. Note that the subscripts 1 and 2 are associated with the tumor and the surrounding tissue, respectively. The boundary conditions to the temperature at the inner and outer surfaces are defined by the following parameters: $A_{in}^* = A_{out}^* = 0\,\text{W/m/K}, B_{in}^* = B_{out}^* = 1\,\text{W/m}^2\text{/K}, C_{in}^* = \hat{C}\ \text{W/m}^2\ (\hat{C} \in \mathbb{R})$ and $C_{out}^* = 310\ \text{W/m}^2$.

After some algebra the particular integral to the steady state nonhomogeneous problem (see (18), (42) and (59)) can be evaluated giving

$$S_1(r) = \frac{\exp(-\gamma_1 r)}{r\,\alpha_1 \gamma_1^4}\begin{pmatrix} -2Q_2 + \left(\sinh(\gamma_1 r) + \cosh(\gamma_1 r)\right)\times \\ \times\left(r\,Q_1\gamma_1^2 + Q_2\left(2 + r^2\gamma_1^2\right) + Q_3\left(6r + r^3\gamma_1^2\right)\right) \end{pmatrix} \tag{60}$$

where $Q_j = (Q_j^* / \rho_1 c_1 \omega_{b1} T_{r0}^*)$, $1 \le j \le 3$.

From Figure 2.2, one can conclude that the eigenvalues of the transient homogeneous problem satisfy approximately a linear distribution for $1 \le m \le 100$ with $m \in \mathbb{N}$. This means that the time decay of the solution to the transient and homogeneous problem is more accentuated as m increases. An advantage of this linear relationship is to avoid further numerical calculations of the eigenvalues. Thus, the computational time decreases significantly.

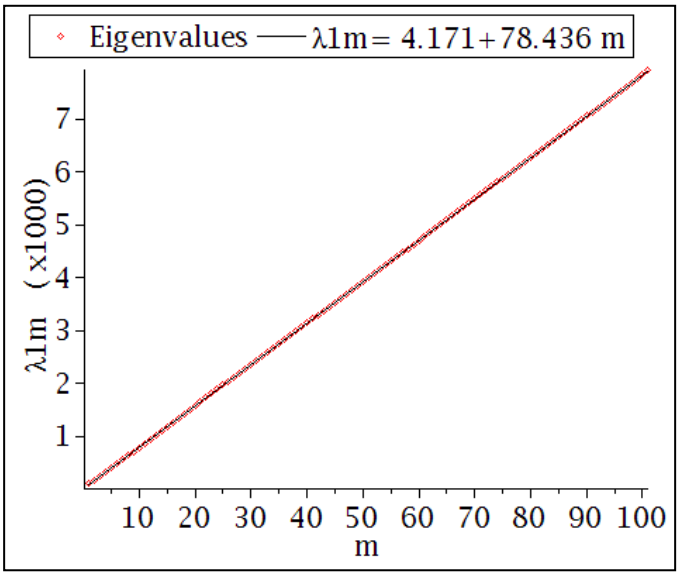

Figure 2.2 – Eigenvalues of the transient solution obtained here.

In Figure 2.3, one can compare the temperature profiles obtained here (denoted by V-solution) with those of Bagaria and Johnson at the time t^* = 100 s and t^* = 300 s. The steady state temperature distributions are also compared. As expected, a good agreement between the temperature profiles is found.

According to Dewey [22], the ideal therapeutic temperature is higher than 42 ^{o}C. In the case studied here, one can see that the temperature of a small part of the spherical tumor (radius 1 cm) is not in the ideal therapeutic range. However, the hyperthermia technique induces a tumor sensitization effect caused by heat. Thus, one can take advantage of the tumor sensitization to enhance the efficacy of other techniques such as radiotherapy and chemotherapy [1, 3].

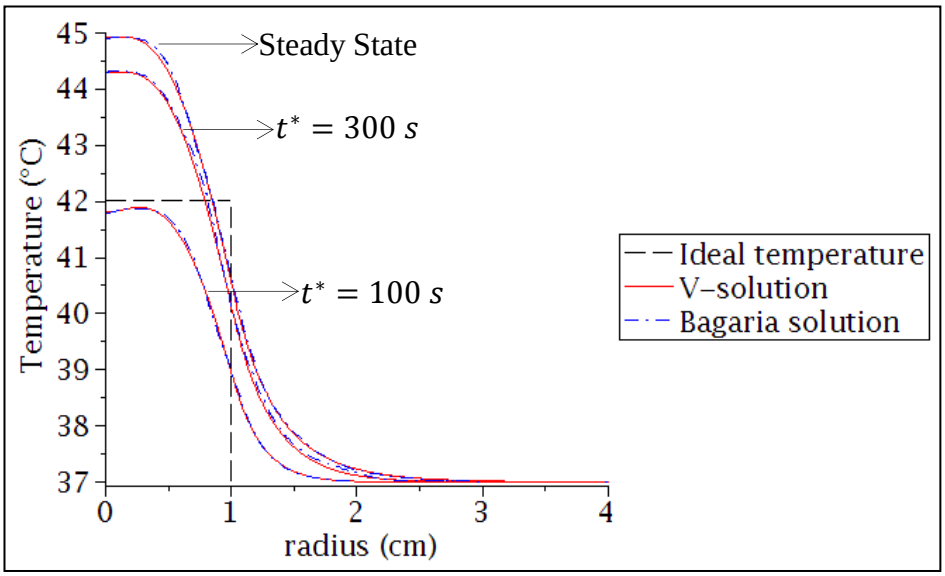

Figure 2.3 – Comparative results between Bagaria *et al.* and those obtained here (V-solution).

Figure 2.4 shows the transient temperature for different locations inside and outside the tumor. In hyperthermia treatments, both therapeutic temperature and treatment time are crucial factors that contribute to cell death. The literature clearly shows that significant cell killing as well as sensitization to radiation and/or chemotherapy occurs when cells are heated to temperatures higher than 42 ^{o}C for one hour or more [1, 22].

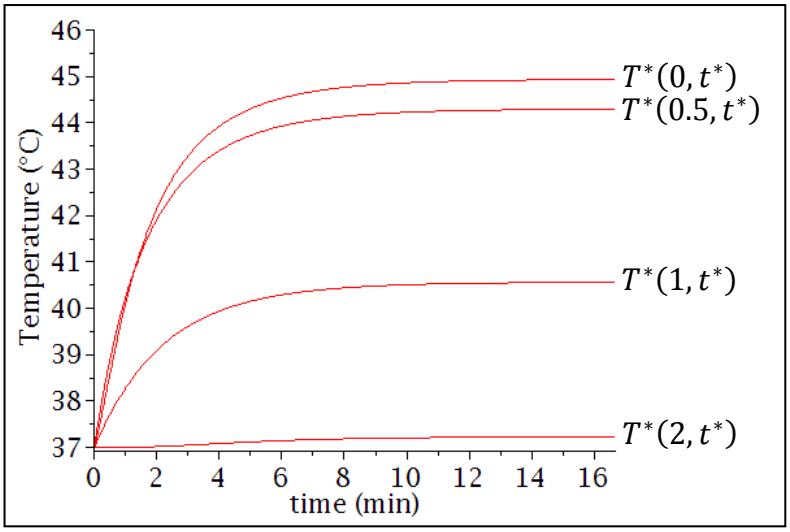

Figure 2.4 – Temperature profiles inside and outside the tumor obtained here at different radius values (cm).

2.3.1.1. Error analysis

The transient solution is given by an infinite Bessel series (see (49)) and must be truncated at some order say $m = M$ to obtain an approximate solution. Consequently, a truncation error $\varepsilon(r,t;M)$ must be evaluated, which is defined by the expression:

(61) $$\bar{T}_i(r,t) = \sum_{m=1}^{M} R_{im}(r)\Psi_{im}(t) + \varepsilon_i(r,t;M)$$

From Figure 2.2, one can conclude that the eigenvalues increase with increasing m and since the time dependent function Ψ_{im} must be time evanescent (see (48) and (53)) the maximum truncation error occurs at $t = 0$. From (34) we have $\bar{T}_i(r,t=0) = T_{0i}(r) - \hat{T}_i(r)$. Thus, one can write

(62) $$\left|\varepsilon_i(r,t;M)\right| \le \left|\varepsilon_i(r,0;M)\right|$$

where $\varepsilon_i(r,0;M)$ can be rewritten as follows:

(63) $$\varepsilon_i(r,0;M) = T_{0i}(r) - \hat{T}_i(r) - \sum_{m=1}^{M} d_m R_{im}(r)$$

In Figure 2.5, one can observe the absolute value of the truncation error $|\varepsilon_i(r^*,0;M)|$ as a function of the radius (cm) in both layers. From this figure, one can conclude that $|\varepsilon_i(r^*,0;M)|$ has a global maximum at $r^* = r_0^*$, which is caused due to the imposition that temperature must be bounded at this point. Since this error function is a result of

combined Bessel functions with particular integral given by (60), a decay rate of $|\varepsilon_i(r^*,0;M)|$ with distance is observed. However, since we impose continuity boundary conditions at $r^* = r_1^*$, the error increases and as a result we find two relative maximums at both sides of this interface. Moreover, as the order *M* increases more Bessel functions with different arguments are combined and the number of zeros increases. As expected, as the order of the Bessel series *M* increases the error decreases. Thus, the value of *M* can be chosen depending on the accuracy required.

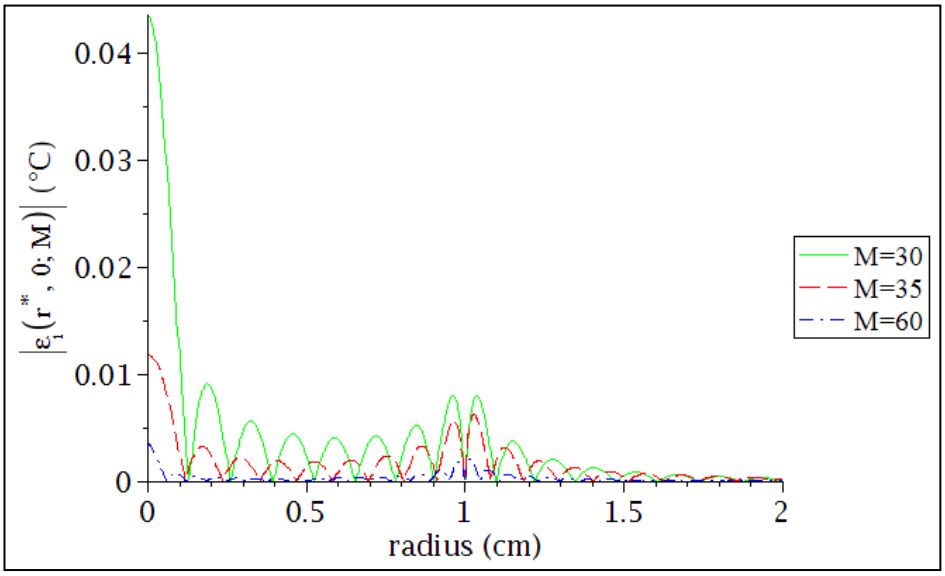

Figure 2.5 – Error analysis for the transient temperature solution at $t^* = 0\,s$.

2.3.2. MFH technique with an exponential heat source term

Salloum *et al.* measured the temperature elevation in the muscle tissue of rat hind limbs induced by intramuscular injections of magnetic nanoparticles during *in vivo* MFH experiments [9]. Instead of a polynomial distribution, they proposed a Gaussian distribution for the internal source term:

$$P_1^*\left(r^*\right) = A_1^* \exp\left(-r^{*2} / r_\varnothing^{*2}\right) \tag{64}$$

where $r_\varnothing^*$ is a parameter that determines how far nanoparticles spread from the injection site and A_1^* represents the maximum strength of the volumetric heat generation. These parameters were calculated using an inverse heat transfer analysis and the bioheat equation.

Similar to Salloum *et al.* [9], we choose the following set of parameters: $A_1^* = 169180$ W/m^3, $r_\varnothing^* = 0.0078$ m, $\rho_{np} = 5240$ kg/m^3, $\rho_b = \rho_2 = 1000$ kg/m^3, $c_{np} = 670$ J/kg/K, $c_2 = 4180$ J/kg/K, $k_1 = k_2 = 0.5$ W/m/K, $Q_{m1}^* = Q_{m2}^* = 0$ W/m^3, $\omega_{b1} = \omega_{b2} = 0.00129$ (1/s) and $T_a^* = T_{r0}^* = 308.3$K. Note that the subscripts 1 and 2 refer to the muscle tissue with and without nanoparticles, respectively. The nanoparticles index is *np* and a constant thermal conductivity is taken into account.

Moreover, a homogeneous conical geometry was used to model rat hind limbs in [9]. However, in this work we assume a cylindrical geometry with two distinct regions. The radius of the inner and outer regions are $r_1^* = 0.0078$ m and $r_2^* = 0.0212$ m, respectively. In this case $r_\varnothing^* = r_1^*$ and $r_0^* = 0$ m.

Here, the mass density and the specific heat capacity of the inner region are given by [8]

(65) $$\rho_1 = \varphi\rho_{np} + (1-\varphi)\rho_2$$

(66) $$c_1 = \varphi c_{np} + (1-\varphi)c_2$$

where $\varphi = 0.0033$ is the volume fraction of nanoparticles in the tissue, which is calculated using the data given in [9].

The boundary conditions to the temperature at the inner and outer surfaces are defined by the following parameters: $A_{in}^* = 0$ W/m/K, $B_{in}^* = 1$ W/m^2/K, $C_{in}^* = \hat{C}$ W/m^2 ($\hat{C} \in \mathbb{R}$), $A_{out}^* = k_2$, $B_{out}^* = h_{air}$, $C_{out}^* = h_{air}T_{air}^*$, $T_{air}^* = 302.5$K and $h_{air} = 13$ W/m^2/K.

One can show in a straightforward manner the following relationships ($m \in \mathbb{N}_0$):

(67) $$W_m(r) = \int r^{2m+1} P_1(r)\, dr = -\frac{P_1(r)}{2}\sum_{k=0}^{m}\frac{m!}{k!} r_\varnothing^{2m+2-2k}\, r^{2k}$$

(68) $$\int \frac{W_m(r)}{r}\, dr = \frac{A_1 r_\varnothing^{2m+2}\, m!}{4} Ei\left(1, r^2/r_\varnothing^2\right) + \frac{r_\varnothing^{2m+2} P_1(r)}{4}\sum_{k=1}^{m}\sum_{l=0}^{k-1}\frac{(m!)}{k(l!)}\left(\frac{r}{r_\varnothing}\right)^{2l}$$

where the function denoted by *Ei* is the exponential integral, $P_1(r) = A_1 \exp(-(r_2^* r / r_1^* r_\varnothing)^2)$, $A_1 = (A_1^* / \rho_1 c_1 \omega_{b1} T_{r0}^*)$ and $r_\varnothing = r_\varnothing^* / r_1^*$.

From (18), (42), (64), (67) and (68) the particular integral of the steady state nonhomogeneous problem is deduced giving

$$S_1(r)=\frac{K_0(\gamma_1 r)}{\alpha_1}\sum_{m=0}^{+\infty}\frac{\gamma_1^{2m}}{4^m(m!)^2}W_m(r)- \\ -\frac{I_0(\gamma_1 r)}{\alpha_1}\sum_{m=0}^{+\infty}\frac{\gamma_1^{2m}}{4^m(m!)^2}\left[W_m(r)\left(\Gamma_d(m+1)-ln\left(\frac{\gamma_1 r}{2}\right)\right)+\int\frac{W_m(r)}{r}dr\right] \quad (69)$$

where Γ_d is the digamma function.

In Figure 2.6, the steady state temperature distribution derived here is compared with that of Salloum *et al.* [9] obtained by experimental measurements. From the symmetry of the problem, the steady state temperature is an even function and it is presented as a function of the distance between medial and lateral skin of the limb. The graph of this even function is translated of r_2^* units to the right in the abscissas axis in order to correctly describe this skin-to-skin distance. A good agreement between the analytical and experimental results is achieved in the full region of analysis.

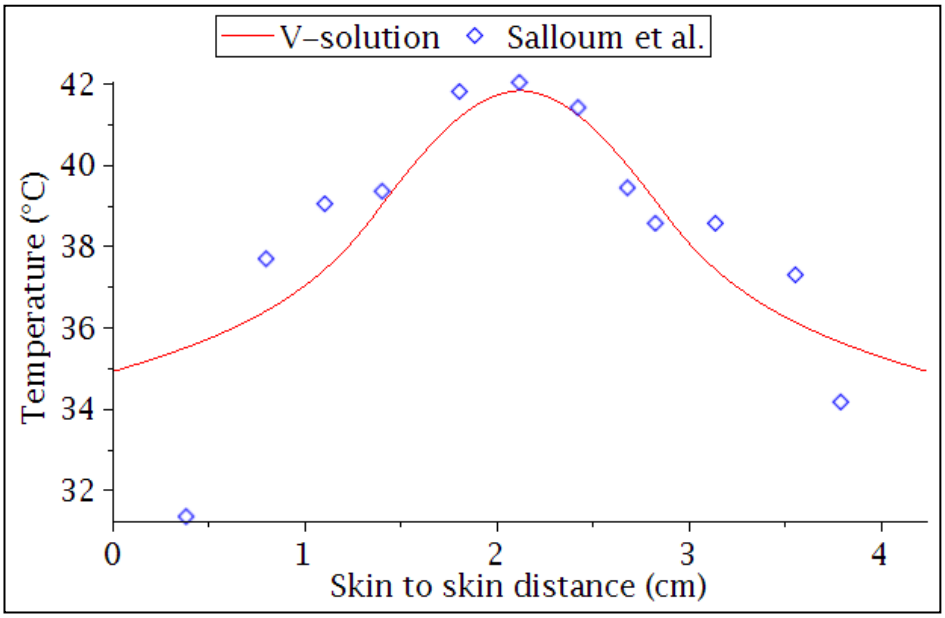

Figure 2.6 – Salloum *et al.* experimental data [9] versus the analytical solution obtained here (V-solution).

The results of Figures 2.3 and 2.6 suggest that the temperature distribution associated with the exponential and polynomial heat source terms can be similar for a certain set of parameters (see (59) and (64)). In order to obtain similar temperature profiles, we recalculate Bagaria's parameters (see (59)) since these were obtained from a theoretical analysis [7]. As criteria, we impose here that the strength of the volumetric heat

generation at r_0^* and r_1^* as well as the average power per unit of area ($r_0^* \le r^* \le r_1^*$) of both heat sources are the same. Using these criteria we have: $Q_1^* = 169180\,\mathrm{W/m^3}$, $Q_2^* = -5.53\times10^6\,\mathrm{W/m^4}$ and $Q_3^* = -1.05\times10^9$ W/m^5. This way, one can show that the temperature curves almost coincide for all $r_0^* \le r^* \le r_2^*$.

From (4) and the values of the parameters A_{in}^*, B_{in}^* and C_{in}^* of both source terms, the inner surface boundary conditions are defined such that the temperature is bounded at $r^* = r_0^*$. Therefore, the v_1 coefficients in (40) are obtained imposing that the limit of the steady state and nonhomogeneous solutions (see (38)) as r^* approaches r_0^{*+} exists and is finite.

2.3.3. Temperature distribution in a multi-layered human head with the effect of large blood vessels

In this final example, the model developed in this work is used to study the steady state temperature distribution in the human head. The analytical solution is compared with a FEM numerical solution implemented in COMSOL Multiphysics v4.1 using a parallel sparse direct linear solver (PARDISO) with a mesh constituted by 4090 elements (maximal element size of 91.3 μm). Four layers are considered: brain white matter ($r_1^* = 6.7$ cm), brain grey matter ($r_2^* = 8.5$ cm), bone ($r_3^* = 8.9$ cm) and scalp ($r_4^* = 9.3$ cm). The outer surface is surrounded by air at $T_{air}^* = 302.5$ K and different convection coefficients h_{air} are compared: 0, 5 and 15 W/m^2/K. From these parameters we can deduce the outer boundary condition from $B_{out}^* = h_{air}$, $C_{out}^* = h_{air}T_{air}^*$ and $A_{out}^* = k_{scalp}$, where $k_{scalp} = 0.49$ W/m/K is the thermal conductivity of the scalp [23].

To further explore the potential of this model, we also study the convective effect of a large blood vessel located inside the brain with radius $r_{bl} = 0.17$ cm. In this case, the inner radius r_0^* has to be the same as r_{bl} in order to account for the presence of the vessel. A constant convective heat transfer coefficient is assumed at the vessel surface and the blood is considered to be at 37 °C, which corresponds to body core temperature.

Assuming a laminar and fully thermally developed blood flow, the convective heat transfer coefficient is given by the following expression [24]:

$$h_{bl} = \frac{1.83 k_{bl}}{r_{bl}} \tag{70}$$

where $k_{bl} = 0.5\,\text{W/m/K}$ is the thermal conductivity of blood. All the other physical and physiological properties of the biological tissues can be found in [23].

The three cases shown in Figure 2.7 model three distinguishable typical daily situations: an isolated environment as when we use an insulating hat ($h_{air} = 0$ W/m^2/K), an interior room environment with low but steady air circulation, e.g., an operating room ($h_{air} = 5$ W/m^2/K) and a windy exterior environment ($h_{air} = 15$ W/m^2/K). A first conclusion that can be drawn is the ability of the human head to preserve the brain temperature at 37 °C regardless of the air convection coefficients used here.

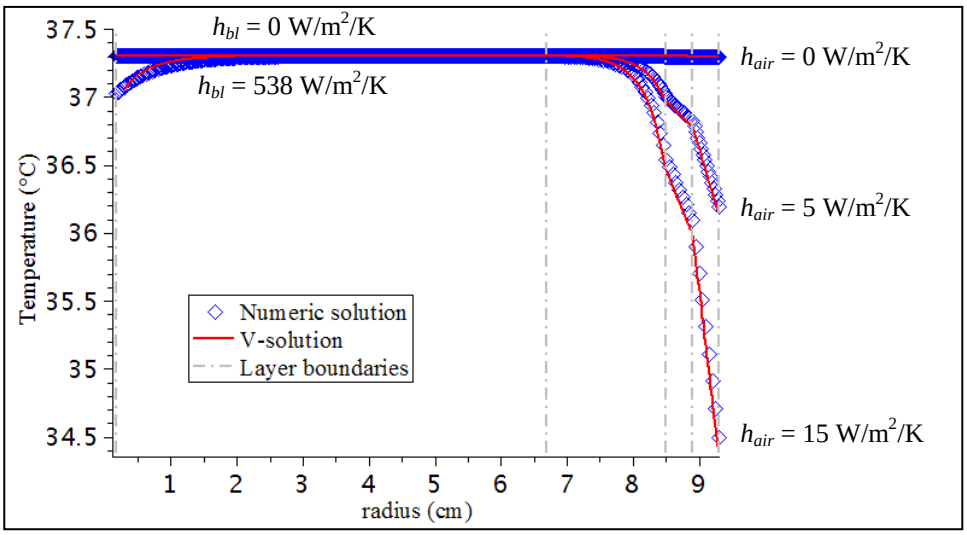

Figure 2.7 – Temperature in a multi-layered model of the head with different air and blood convection coefficients, where the layers correspond to: brain white matter (0-6.7 cm), brain gray matter (6.7-8.5 cm), bone (8.5-8.9 cm) and scalp (8.9-9.3 cm).

The inclusion of a large vessel in this model provides the opportunity to analyze the effect of convection from blood vessels that are larger than arterioles and venules. This is not accounted in the classic Pennes' model. The steady state temperature of white matter is 37.3 °C without the presence of large blood vessels (see Figure 2.7). Moreover, the presence of the blood vessel of r_{bl} = 0.17 cm located in the center of the brain,

causes that the temperature near the wall drops down to 37 °C. This model aims to study the effect of a single vessel and not the complex blood vessel network in the brain [25]. However, the uniform white matter temperature of 37.3 °C (without the blood vessel) and the drop of 0.3 °C near the blood vessel, suggest that the highly vascularized brain should be at 37 °C. This conclusion agrees with the results presented in Konstas [23].

From Figure 2.7, one can observe a good agreement between analytical and FEM numerical solutions. In general, numerical solutions have enough accuracy and can be developed for more complex geometries. The geometry flexibility and no development of complex mathematical formalisms are perhaps the major advantages of this kind of solutions. However, there are cases where convergence and stability problems arise leading to the divergence and blow-up of these solutions. It is well known that the violation of a CFL (Courant-Friedrichs-Lewy) type condition leads to unstable modes [26]. In some situations, one can avoid these problems by increasing the number of iterations, *i.e.*, smaller mesh element sizes and time steps are required. Thus, the computational time increases accordingly. This may imply a non-acceptable running time of numerical algorithms. These unstable modes may also be intrinsic to the partial differential equations or caused by more complex geometries especially with steepest gradients. Note that the spatial and time dependence as well as the type of some terms or coefficients in the equations can modify the nature, *i.e.*, the convergence and stability as well as the linearity of the heat transfer system. Therefore, these divergent and unstable modes cannot be avoided in some more complex problems for all space and time domain.

Moreover, the numerical solutions are approximate in its nature, meaning quantitative, and do not provide qualitative information about the problem. From a mathematical point of view, both quantitative and qualitative analysis of solutions are preferable for more understanding of complex problems. In fact, the analytical solutions allow the study of both quantitative and qualitative response of the biological system to a given heat source term or coefficient in the partial differential equations. This is highlighted, e.g., in the equations (60) and (69) where the temperature response to a polynomial and exponential heat sources is given by a combination of explicit and well defined mathematical functions. On the other hand, analytical solutions also allow real and space-time dependences of temperature and its gradients. These insights are given by an

analytical approach and ultimately lead to a better understanding of the biological problem.

2.4. Conclusions and future work

An analytical solution to the Pennes' bioheat equation is derived to calculate the heat transfer in a multi-layer perfused tissue. Multi-layer regions with 1D Cartesian, cylindrical and spherical symmetric geometries as well as spatially dependent heat source terms are considered. Boundary conditions of first, second and third kinds to the temperature at the inner and outer surfaces are obtained from an appropriate choice of parameters. The biological model is further enhanced by introducing an important thermoregulation mechanism, namely, the temperature dependent metabolic heat rate.

The complexity of the problem presented here is highly reduced by the layer-independent coefficient d_m, and by the dependence of all eigenvalues on the one associated with the first layer. These eigenvalues also show a linear dependence on the order of the infinite Bessel series denoted by m. This linear dependence reduces the computational time since no numerical computation is required. Moreover, the mathematical formalism developed here shows that the full solution is defined by two branches, where one is time evanescent and the other is not. We stress that time evanescent solutions must be obtained since the transient and homogeneous equation does not have an external heat source term to supply energy to the biological system. Thus, the number of branches is reduced from two to one. This means that after a long time the full solution does not depend on time and is given approximately by the solution of the steady state (nonhomogeneous) equation which only depends on the spatial coordinate.

The derived solution is applied to study two distinct spatially dependent heat sources that characterize the heating induced by magnetic nanoparticles subjected to an electromagnetic field. The closed-form of the analytical solution for such polynomial and exponential heat sources is deduced. A good agreement is achieved between the results provided by these analytical solutions and those obtained theoretically and experimentally by other authors. It is proved that the polynomial and exponential profiles can be interchanged by choosing the correct parameters associated with these

source terms. We can conclude that these polynomial and exponential functions are equivalent and valid to describe the heat source in magnetic fluid hyperthermia.

In hyperthermia treatments, both therapeutic temperature and treatment time are crucial factors in establishing cell death. The spatial transient model developed here is suitable for analyzing both these physical quantities. It is difficult to achieve an ideal temperature profile within the entire tumor and its healthy tissue surroundings, but tumor sensitization can still be induced. Thus, one can take advantage of the tumor sensitization to apply other techniques, e.g., radiotherapy or chemotherapy, in order to obtain efficacious cancer therapy. The inability to generate and maintain ideal temperature distributions in heterogeneous perfused tissue is the reason why hyperthermia is considered as an adjuvant rather than standalone cancer therapy.

The versatile inner and outer boundary conditions introduced here are used to study different environmental conditions as well as the effect of a large blood vessel inside a human brain, which complements the classical bioheat model. This study shows the ability of the human head to preserve the brain temperature around 37 °C in a wide range of environmental conditions. The blood vessel could only be accounted due to the flexible inner boundary condition, which allows to have $r_0 = 0$ m or $r_0 > 0$ m.

As future work one can model a problem with an inner surface to simulate a hyperthermia or ablation catheter immersed in a diseased tissue to study the efficacy of different heating techniques. This one dimensional and transient bioheat transfer model is being currently developed to be applied to problems with higher dimensions as well as spatial and time dependent heat sources.

Acknowledgements

The author Dário Barros Rodrigues is gratefully acknowledged for the support of this work by Portuguese Foundation for Science and Technology under the PhD grants SFRH/BD/42305/2007 and SFRH/BD/73215/2010. This work also forms part of the EU/ESF COST Action Nanoscale Insights into Ion Beam Cancer Therapy (Nano-IBCT) MP1002.

Appendix 2A - Definition of the coefficients in the equations (43) and (54)

The coefficients of the matrices on the right hand side of (43) are defined by

(A.1) $$\hat{c}_1 = A_{in}\left(r^{-\varepsilon(G)} I_{\varepsilon(G)}(\gamma_1 r)\right)'_{r=r_0} + B_{in} r_0^{-\varepsilon(G)} I_{\varepsilon(G)}(\gamma_1 r_0)$$

(A.2) $$\hat{c}_2 = A_{in}\left(r^{-\varepsilon(G)} K_{\varepsilon(G)}(\gamma_1 r)\right)'_{r=r_0} + B_{in} r_0^{-\varepsilon(G)} K_{\varepsilon(G)}(\gamma_1 r_0)$$

(A.3) $$\hat{c}_3 = C_{in} - A_{in}\left(S_1(r)\right)'_{r=r_0} - B_{in} S_1(r_0)$$

(A.4) $$\hat{c}_4 = A_{out}\left(r^{-\varepsilon(G)} I_{\varepsilon(G)}(\gamma_n r)\right)'_{r=r_n} + B_{out} r_n^{-\varepsilon(G)} I_{\varepsilon(G)}(\gamma_n r_n)$$

(A.5) $$\hat{c}_5 = A_{out}\left(r^{-\varepsilon(G)} K_{\varepsilon(G)}(\gamma_n r)\right)'_{r=r_n} + B_{out} r_n^{-\varepsilon(G)} K_{\varepsilon(G)}(\gamma_n r_n)$$

(A.6) $$\hat{c}_6 = C_{out} - A_{out}\left(S_n(r)\right)'_{r=r_n} - B_{out} S_n(r_n)$$

(A.7) $$\hat{\phi}_{i1} = r_i^{-\varepsilon(G)} I_{\varepsilon(G)}(\gamma_i r_i)$$

(A.8) $$\hat{\phi}_{i2} = r_i^{-\varepsilon(G)} K_{\varepsilon(G)}(\gamma_i r_i)$$

(A.9) $$\hat{\phi}_{i3} = -r_i^{-\varepsilon(G)} I_{\varepsilon(G)}(\gamma_{i+1} r_i)$$

(A.10) $$\hat{\phi}_{i4} = -r_i^{-\varepsilon(G)} K_{\varepsilon(G)}(\gamma_{i+1} r_i)$$

(A.11) $$\hat{\Phi}_i = S_{i+1}(r_i) - S_i(r_i)$$

(A.12) $$\hat{\omega}_{i1} = k_i\left(r^{-\varepsilon(G)} I_{\varepsilon(G)}(\gamma_i r)\right)'_{r=r_i}$$

(A.13) $$\hat{\omega}_{i2} = k_i\left(r^{-\varepsilon(G)} K_{\varepsilon(G)}(\gamma_i r)\right)'_{r=r_i}$$

(A.14) $$\hat{\omega}_{i3} = -k_{i+1}\left(r^{-\varepsilon(G)} I_{\varepsilon(G)}(\gamma_{i+1} r)\right)'_{r=r_i}$$

(A.15) $$\hat{\omega}_{i4} = -k_{i+1}\left(r^{-\varepsilon(G)} K_{\varepsilon(G)}(\gamma_{i+1} r)\right)'_{r=r_i}$$

(A.16) $$\hat{\Omega}_i = k_{i+1}\left(S_{i+1}(r)\right)'_{r=r_i} - k_i\left(S_i(r)\right)'_{r=r_i}$$

where the prime symbol denotes differentiation with respect to *r*.

The coefficients of the determinant in (54) are given by

(A.17) $$\bar{c}_{1m} = A_{in}\left(r^{-\varepsilon(G)} J_{\varepsilon(G)}(\lambda_{1m} r)\right)'_{r=r_0} + B_{in} r_0^{-\varepsilon(G)} J_{\varepsilon(G)}(\lambda_{1m} r_0)$$

(A.18) $$\bar{c}_{2m} = A_{in}\left(r^{-\varepsilon(G)} Y_{\varepsilon(G)}(\lambda_{1m} r)\right)'_{r=r_0} + B_{in} r_0^{-\varepsilon(G)} Y_{\varepsilon(G)}(\lambda_{1m} r_0)$$

(A.19) $$\bar{c}_{4m} = A_{out}\left(r^{-\varepsilon(G)}J_{\varepsilon(G)}\left(\lambda_{nm}r\right)\right)'_{r=r_n} + B_{out}r_n^{-\varepsilon(G)}J_{\varepsilon(G)}\left(\lambda_{nm}r_n\right)$$

(A.20) $$\bar{c}_{5m} = A_{out}\left(r^{-\varepsilon(G)}Y_{\varepsilon(G)}\left(\lambda_{nm}r\right)\right)'_{r=r_n} + B_{out}r_n^{-\varepsilon(G)}Y_{\varepsilon(G)}\left(\lambda_{nm}r_n\right)$$

(A.21) $$\bar{\phi}_{i1m} = r_i^{-\varepsilon(G)}J_{\varepsilon(G)}\left(\lambda_{im}r_i\right)$$

(A.22) $$\bar{\phi}_{i2m} = r_i^{-\varepsilon(G)}Y_{\varepsilon(G)}\left(\lambda_{im}r_i\right)$$

(A.23) $$\bar{\phi}_{i3m} = -r_i^{-\varepsilon(G)}J_{\varepsilon(G)}\left(\lambda_{i+1,m}r_i\right)$$

(A.24) $$\bar{\phi}_{i4m} = -r_i^{-\varepsilon(G)}Y_{\varepsilon(G)}\left(\lambda_{i+1,m}r_i\right)$$

(A.25) $$\bar{\omega}_{i1m} = k_i\left(r^{-\varepsilon(G)}J_{\varepsilon(G)}\left(\lambda_{im}r\right)\right)'_{r=r_i}$$

(A.26) $$\bar{\omega}_{i2m} = k_i\left(r^{-\varepsilon(G)}Y_{\varepsilon(G)}\left(\lambda_{im}r\right)\right)'_{r=r_i}$$

(A.27) $$\bar{\omega}_{i3m} = -k_{i+1}\left(r^{-\varepsilon(G)}J_{\varepsilon(G)}\left(\lambda_{i+1,m}r\right)\right)'_{r=r_i}$$

(A.28) $$\bar{\omega}_{i4m} = -k_{i+1}\left(r^{-\varepsilon(G)}Y_{\varepsilon(G)}\left(\lambda_{i+1,m}r\right)\right)'_{r=r_i}$$

Appendix 2B - Proof of the orthogonality condition (50)

Let R_{im} and R_{il} (m, $l \in \mathbb{N}$) be transverse eigenfunctions satisfying equation (45). Thus, we have

$$\frac{1}{r^G}\frac{d}{dr}\left(r^G\frac{dR_{im}}{dr}\right)+\frac{\lambda_{im}^2}{\alpha_i}R_{im}=0 \tag{B.1}$$

$$\frac{1}{r^G}\frac{d}{dr}\left(r^G\frac{dR_{il}}{dr}\right)+\frac{\lambda_{il}^2}{\alpha_i}R_{il}=0 \tag{B.2}$$

Multiplying (B.1) by R_{il} and (B.2) by R_{im} and subtracting, we obtain

$$\frac{R_{il}}{r^G}\frac{d}{dr}\left(r^G\frac{dR_{im}}{dr}\right)-\frac{R_{im}}{r^G}\frac{d}{dr}\left(r^G\frac{dR_{il}}{dr}\right)+\left(\frac{\lambda_{im}^2}{\alpha_i}-\frac{\lambda_{il}^2}{\alpha_i}\right)R_{il}R_{im}=0 \tag{B.3}$$

Multiplying (B.3) by r^G and integrating from r_{i-1} to r_i, one can show

$$\int_{r_{i-1}}^{r_i}R_{il}\frac{d}{dr}\left(r^G\frac{dR_{im}}{dr}\right)dr-\int_{r_{i-1}}^{r_i}R_{im}\frac{d}{dr}\left(r^G\frac{dR_{il}}{dr}\right)dr+\int_{r_{i-1}}^{r_i}r^G\left(\frac{\lambda_{im}^2}{\alpha_i}-\frac{\lambda_{il}^2}{\alpha_i}\right)R_{il}R_{im}\,dr=0 \tag{B.4}$$

Applying the method of integration by parts twice in the first integral of (B.4), the following expression is obtained:

$$\left[r^GR_{il}\frac{dR_{im}}{dr}-r^GR_{im}\frac{dR_{il}}{dr}\right]_{r_{i-1}}^{r_i}+\int_{r_{i-1}}^{r_i}r^G\left(\frac{\lambda_{im}^2}{\alpha_i}-\frac{\lambda_{il}^2}{\alpha_i}\right)R_{il}R_{im}dr=0 \tag{B.5}$$

Multiplying the above equation by k_i and summing over all i ($1 \le i \le n$), one can deduce

$$\sum_{i=1}^{n}\left[k_i\,r^GR_{il}\frac{dR_{im}}{dr}-k_i\,r^GR_{im}\frac{dR_{il}}{dr}\right]_{r_{i-1}}^{r_i}+\sum_{i=1}^{n}\frac{k_i}{\alpha_i}\left(\lambda_{im}^2-\lambda_{il}^2\right)\int_{r_{i-1}}^{r_i}r^GR_{im}R_{il}dr=0 \tag{B.6}$$

From (B.6) and applying interface boundary conditions (26), (28), (30) and (32) as well as (47)-(49), we have

$$\left[k_n\,r^GR_{nl}\frac{dR_{nm}}{dr}-k_n\,r^GR_{nm}\frac{dR_{nl}}{dr}\right]_{r=r_n}-\left[k_1\,r^GR_{1l}\frac{dR_{1m}}{dr}-k_1\,r^GR_{1m}\frac{dR_{1l}}{dr}\right]_{r=r_0}+$$
$$+\sum_{i=1}^{n}\frac{k_i}{\alpha_i}\left(\lambda_{im}^2-\lambda_{il}^2\right)\int_{r_{i-1}}^{r_i}r^GR_{im}R_{il}dr=0 \tag{B.7}$$

From the outer surface boundary condition (24) and (47)-(49), we obtain

$$\left[A_{out}\frac{dR_{nm}}{dr}+B_{out}R_{nm}\right]_{r=r_n}=0 \tag{B.8}$$

(B.9) $$\left[A_{out} \frac{dR_{nl}}{dr} + B_{out} R_{nl} \right]_{r=r_n} = 0$$

Multiplying (B.8) by $k_n r_n^G R_{nl}(r_n)$ and (B.9) by $k_n r_n^G R_{nm}(r_n)$ and subtracting, one can show

(B.10) $$A_{out} k_n r_n^G \left[R_{nl} \frac{dR_{nm}}{dr} - R_{nm} \frac{dR_{nl}}{dr} \right]_{r=r_n} = 0$$

Now, different cases can be analyzed. If $A_{out} \neq 0$ (B.10) can be rewritten as follows:

(B.11) $$k_n r_n^G \left[R_{nl} \frac{dR_{nm}}{dr} - R_{nm} \frac{dR_{nl}}{dr} \right]_{r=r_n} = 0$$

Note that (B.11) is valid for $A_{out} \neq 0$ and $B_{out} \neq 0$ as well as $A_{out} \neq 0$ and $B_{out} = 0$. Moreover, if $A_{out} = 0$ and $B_{out} \neq 0$, one can obtain $R_{nm}(r_n) = 0$ and $R_{nl}(r_n) = 0$ using (B.8) and (B.9), respectively. Thus, (B.11) is also valid for this last case.

A similar methodology can be applied using the inner surface boundary condition (22) and (47)-(49), giving

(B.12) $$k_1 r_0^G \left[R_{1l} \frac{dR_{1m}}{dr} - R_{1m} \frac{dR_{1l}}{dr} \right]_{r=r_0} = 0$$

Finally, one can use equations (B.7), (B.11) and (B.12) to obtain

(B.13) $$\sum_{i=1}^{n} \frac{k_i}{\alpha_i} \left(\lambda_{im}^2 - \lambda_{il}^2 \right) \int_{r_{i-1}}^{r_i} r^G R_{im} R_{il} dr = 0$$

From (52) and a similar expression to λ_{il}, one can show

(B.14) $$\lambda_{im}^2 - \lambda_{il}^2 = \frac{\alpha_1}{\alpha_i} \left(\lambda_{1m}^2 - \lambda_{1l}^2 \right)$$

Note that $\lambda_{1m}^2 - \lambda_{1l}^2 \neq 0$ for $m \neq l$. Using this last result as well as (B.13) and (B.14), one can deduce the orthogonality condition (50) giving

(B.15) $$\sum_{i=1}^{n} \frac{k_i}{\alpha_i^2} \int_{r_{i-1}}^{r_i} r^G R_{im}(r) R_{il}(r) \, dr = 0 \qquad (m \neq l)$$

References

1. Habash RWY, Krewski D, Bansal R, Alhafid HT: Principles, applications, risks and benefits of therapeutic hyperthermia. Frontiers in bioscience (Elite edition) 2011, 3:1169-1181.

2. Sheu TWH, Solovchuk MA, Chen AWJ, Thiriet M: On an acoustics-thermal-fluid coupling model for the prediction of temperature elevation in liver tumor. International Journal of Heat and Mass Transfer 2011, 54(17-18):4117-4126.

3. Craciunescua OI, Stauffer PR, Soher BJ, Wyatt CR, Arabe O, Maccarini P, Das SK, Cheng KS, Wong TZ, Jones EL et al: Accuracy of real time noninvasive temperature measurements using magnetic resonance thermal imaging in patients treated for high grade extremity soft tissue sarcomas. Medical Physics 2009, 36(11):4848-4858.

4. Wang YJ, Zhu L, Rosengart AJ: Targeted brain hypothermia induced by an interstitial cooling device in the rat neck: Experimental study and model validation. International Journal of Heat and Mass Transfer 2008, 51(23-24):5662-5670.

5. Gellermann J, Wlodarczyk W, Feussner A, Fahling H, Nadobny J, Hildebrandt B, Felix R, Wust P: Methods and potentials of magnetic resonance imaging for monitoring radiofrequency hyperthermia in a hybrid system. International Journal of Hyperthermia 2005, 21(6):497-513.

6. Giordano MA, Gutierrez G, Rinaldi C: Fundamental solutions to the bioheat equation and their application to magnetic fluid hyperthermia. Int J Hyperthermia 2010, 26(5):475-484.

7. Bagaria HG, Johnson DT: Transient solution to the bioheat equation and optimization for magnetic fluid hyperthermia treatment. Int J Hyperthermia 2005, 21(1):57-75.

8. Lin CT, Liu KC: Estimation for the heating effect of magnetic nanoparticles in perfused tissues. Int Commun Heat Mass Transf 2009, 36(3):241-244.

9. Salloum M, Ma RH, Zhu L: An in-vivo experimental study of temperature elevations in animal tissue during magnetic nanoparticle hyperthermia. International Journal of Hyperthermia 2008, 24(7):589-601.

10. Schildkopf P, Ott OJ, Frey B, Wadepohl M, Sauer R, Fietkau R, Gaipl US: Biological Rationales and Clinical Applications of Temperature Controlled Hyperthermia - Implications for Multimodal Cancer Treatments. Current Medicinal Chemistry 2010, 17(27):3045-3057.

11. Song C, Choi I, Nah B, Sahu S, Osborn J: Microvasculature and perfusion in normal tissues and tumors. In: Thermoradiotherapy and thermochemotherapy. Edited by Seegenschmiedt Mh FPVCCe, vol. Volume 1, Biology, Physiology and Physics. Berlin, New York: Springer-Verlag; 1995: 139-159.

12. Pennes HH: Analysis of tissue and arterial blood temperatures in the resting human forearm. Journal of Applied Physiology 1948, 1(2):93-122.

13. Stanczyk M, Telega J: Modelling of heat transfer in biomechanics - a review, part.I soft tissues. Acta of bioengineering and biomechanics 2002, 4(1):31-61.

14. Fan J, Wang L: A general bioheat model at macroscale. International Journal of Heat and Mass Transfer 2011, 54(1-3):722-726.

15. Durkee JW, Antich PP, Lee CE: Exact-solutions to the multiregion time-dependent bioheat equation .1. Solution development. Phys Med Biol 1990, 35(7):847-867.

16. Durkee JW, Antich PP: Characterization of bioheat transport using an exact solution to the cylindrical geometry, multiregion, time-dependent bioheat equation. Phys Med Biol 1991, 36(10):1377-1406.

17. Durkee JW, Antich PP: Exact-solutions to the multiregion time-dependent bioheat equation with transient heat-sources and boundary-conditions. Phys Med Biol 1991, 36(3):345-368.

18. Okajima J, Maruyama S, Takeda H, Komiya A: Dimensionless solutions and general characteristics of bioheat transfer during thermal therapy. J Therm Biol 2009, 34(8):377-384.

19. Rodrigues DB, Pereira PJS, Limão-Vieira PM, Maccarini PF: Analytical Solution to the Transient 1D Bioheat Equation in a Multilayer Region with Spatial Dependent Heat Sources. In: The Eighth IASTED International Conference on Biomedical Engineering: 2011; Innsbruck. 2011: 96-103.

20. Rai KN, Rai SK: Heat transfer inside the tissues with a supplying vessel for the case when metabolic heat generation and blood perfusion are temperature dependent. Heat and Mass Transfer 1999, 35(4):345-350.

21. Zhu L, Xu LX, Chencinski N: Quantification of the 3-D electromagnetic power absorption rate in tissue during transurethral prostatic microwave thermotherapy using heat transfer model. IEEE Trans Biomed Eng 1998, 45(9):1163-1172.

22. Dewey WC: Arrhenius relationships from the molecule and cell to the clinic. International Journal of Hyperthermia 2009, 25(1):3-20.

23. Konstas A, Neimark M, Laine A, Pile-Spellman J: A theoretical model of selective cooling using intracarotid cold saline infusion in the human brain. Journal of Applied Physiology 2007, 102(4):1329-1340.

24. Lagendijk JJW: The influence of bloodflow in large vessels on the temperature distribution in hyperthermia. Physics in Medicine and Biology 1982, 27(1):17-23.

25. Netter FH: Atlas of Human Anatomy, 4th edition edn. Philadelphia: Elsevier; 2006.

26. Lopes ND, Pereira PJS, Trabucho L: A numerical analysis of a class of generalized Boussinesq-type equations using continuous/discontinuous FEM. International Journal for Numerical Methods in Fluids 2012, 69(7).

Chapter 3

Design and optimization of an ultra-wideband and compact microwave antenna for radiometric monitoring of brain temperature

Abstract

We present the modeling efforts on antenna design and frequency selection to monitor brain temperature during prolonged surgery using non-invasive microwave radiometry. We choose a tapered log-spiral antenna design due to its wideband characteristics that allow higher power collection from deep brain. Parametric analysis with HFSS is used to optimize antenna performance for deep brain temperature sensing. Radiometric antenna efficiency (η) is evaluated in terms of the ratio of the power collected from brain to the total power received by the antenna. Anatomical information extracted from several adult computed tomography (CT) scans is used to determine parameters for an accurate layered 3D tissue phantom. This head phantom presents separate brain and scalp regions, consisting of tissue equivalent liquids circulating at independent temperatures on either side of intact skull. The optimized frequency band is [1.1, 1.6] GHz producing an average antenna efficiency of 50.3% from a 2 turn log-spiral antenna. The entire sensor package is contained in a lightweight and low profile 2.8 cm diameter by 1.5 cm high assembly that can be held in place over the skin with an electromagnetic interference (EMI) shielding adhesive patch. The calculated radiometric equivalent brain temperature tracks within 0.4 °C of measured brain phantom temperature when the brain phantom is lowered 10 °C and then returned to original temperature over a 4.6 hour experiment. A clinical case confirms our ability to non-invasively monitor temperature in deep brain that correlates loosely with core measurements in rectum and nasopharynx. The numerical and experimental results demonstrate that a [1.1, 1.6] GHz radiometric sensor with 2.5 cm diameter log-spiral antenna is an appropriate tool for non-invasively monitoring of deep brain temperature.

CHAPTER 3

Keywords: Antenna design, Optimization, Log-spiral antenna, Noninvasive brain temperature monitoring and Microwave radiometry.

This chapter addresses research work carried out on the studies of antenna design for radiometric monitoring of deep tissue temperature, and has been published/submitted for publication as follows:

1. **Rodrigues DB**, Maccarini PF, Salahi S, Oliveira TR, Pereira PJS, Limão-Vieira P, Snow BW, Reudink D, Stauffer PR: Design and optimization of an ultra-wideband and compact microwave antenna for radiometric monitoring of brain temperature. IEEE Transactions on Biomedical Engineering 2013, Submitted.
2. Stauffer PR, Snow BW, **Rodrigues DB**, Salahi S, Oliveira TR, Reudink D, Maccarini PF: Non-Invasive Core Temperature Measurement in Brain: Demonstration in a Head Phantom and Initial Clinical Experience. The Neuroradiology Journal 2013, Submitted.
3. **Rodrigues DB**, Stauffer PR, Ribeiro TO, Salahi S, Pereira PJS, Limão-Vieira P, Maccarini PF: Design of 3D conical log-spiral antenna for focused radiometric deep temperature readings. In: 2013 Society of Thermal Medicine Annual Meeting: April 17-21; Aruba: Edited by Mercer J. 2013.
4. **Rodrigues DB**, Maccarini PF, Salahi S, Colebeck E, Topsakal E, Pereira PJS, Limao-Vieira P, Stauffer PR: Numerical 3D modeling of heat transfer in human tissues for microwave radiometry monitoring of brown fat metabolism. In: Conference on Energy-Based Treatment of Tissue and Assessment VII: Feb 3-4 2013; San Francisco, CA. SPIE.
5. Stauffer PR, **Rodrigues DB**, Salahi S, Topsakal E, Ribeiro TO, Prakash A, Maccarini PF: Stable microwave radiometry system for long term monitoring of deep tissue temperature. In: Conference on Energy-Based Treatment of Tissue and Assessment VII: 2013; San Jose CA, USA. SPIE.
6. Stauffer PR, **Rodrigues DB**, Ribeiro TO, Topsakal E, Maccarini PF: Microwave Radiometry System for Non-invasive Long Term Monitoring of Deep Tissue Temperature. In: 2013 Society of Thermal Medicine Annual Meeting: April 13-16; Aruba: Edited by Mercer J. 2013.

7. Stauffer PR, Maccarini PF, **Rodrigues DB**, Salahi S, Craciunescu O, Yuan Y, Das S: Towards Integration of Treatment Monitoring with Thermal Modeling for Improved Control of Heat Treatments. In: The 11th International Congress of Hyperthermic Oncology: August 28-31; Kyoto, Japan. 2012.

Award:

2013 New Investigator Travel Award (Society for Thermal Medicine) sponsored by National Institutes of Health (NIH)

CHAPTER 3

3.1. Introduction

Prolonged surgeries use general anesthesia that impairs thermoregulation processes in the human body and is often associated with hypothermia, *i.e.*, when core temperature is below 36 °C [1-3]. In some surgeries hypothermia is actually forced – patients are cooled 5-18 °C below normal body temperature – in order to reduce sensitivity of critical brain tissues to ischemia [4]. In either case it is critical to safely and rapidly rewarm the patient to normal body core temperature (37 °C) before the end of surgery to avoid potential complications such as: triple the risk of morbid myocardial outcomes [5], triple the risk of surgical wound infection [1, 6], increase blood loss [7-9], increase transfusion requirements [7-9], prolong surgical recovery [10] and extend the duration of hospitalization [6].

Readily available non-invasive measurements include axillary and forehead surface thermometers which vary with contact, movement, perspiration, and environment, producing an unreliable prediction of temperature deep in the body core [11, 12]. Infrared thermography can non-invasively sense thermal energy emitted from tissue close to the surface, but those measurements do not reflect temperatures within deep regions of the body. In particular, temperature measurement of the temporal artery takes advantage of high perfusion in the region which could reflect core temperature, but calibration of such readings is highly dependent on skin emissivity, perspiration, and environment which vary greatly for typical operating room conditions [11, 12]. Infrared measurements of the tympanic membrane have the potential to reflect core body temperature accurately but in clinical practice are less reliable due to the tortuous anatomy of the ear canal and presence of cerumen [11, 13].

Invasive measurements of core temperature are generally accomplished either with intracavitary devices like rectal, Foley, oropharyngeal, endotracheal and esophageal probes, or with temperature probes placed interstitially in the pulmonary artery [11, 13-15]. Placement of internal temperature probes is uncomfortable, may require sedation or anesthesia, and is not without risk. The accuracy of these invasive probes depends on many factors [11, 16]. For instance, the position of nasopharyngeal temperature probes placed under anesthesia is uncertain and the amount of mouth breathing or endotracheal tube air leakage affects the readings significantly. Rectal probes work best if the probe tip is located against the perfused rectal wall rather than inside feces, but this is difficult

to ensure and if partially insulated from the rectal wall there may be significant delays in reading of body temperature. Accuracy of bladder thermometry depends on urine production, bladder volume and probe location within the bladder. Like rectal measurements, Foley probes generally exhibit significant time delays in reading actual core body temperature, especially when the temperature is varied rapidly with external heating or cooling source.

The most invasive temperature probe is a pulmonary artery catheter which is passed through a vein, the right atrium of the heart, the right ventricle and finally into the pulmonary artery. This is currently considered to be the best core body temperature measurement [13]. However, only severely ill or high risk surgical patients warrant pulmonary artery monitoring due to the potential risks of such invasive procedure. Also, because of their status, these patients often receive large amounts of room temperature intravenous (IV) fluids as well as refrigerated blood products that reduce the accuracy of this core temperature reading. As an alternative, we present in this paper a monitoring approach based on non-invasive and entirely passive microwave radiometry. We choose to monitor core temperature inside the brain rather than in alternative sites due to the critical nature of this organ and its central role in thermoregulation [16, 17].

Radiometry is a non-invasive technique that collects thermal radiation (electromagnetic noise) emitted in the overall frequency spectrum by any material above the absolute zero temperature. The thermal radiation is received by an antenna and converted, with proper calibration, into a measure of absolute temperature taken from a weighted average of its radiation pattern [18-20]. Microwave radiometers operate in a range of frequencies where photons can travel several centimeters through biological tissue [21]. This technique contrasts with infrared thermometry that collects thermal radiation at higher frequencies ([0.3, 430] THz), where photons travel only a few millimeters through skin. There have been many reports of medical applications of microwave radiometry, including the detection of breast cancer [22], monitoring and control of superficial and deep hyperthermia applicators [23-27], measurement of brain temperature in infants [28, 29] or adult brain phantoms [30], vesicoureteral reflux detection in young children [31-34] and more recently monitoring of brown fat metabolism [35]. In the particular case of monitoring adult brain temperature, there are no reports to our knowledge of an antenna that is small enough to conform to the human head during prolonged surgery; present a stable reading over several hours; and offer an

accuracy <0.5 °C, which is the smallest difference that has been associated with hypothermia-induced complications [8, 16].

The major challenge in microwave radiometry lies on the nature of thermal noise itself which is characterized by extremely low power levels (10^{-14} W/MHz at 37 °C). To maximize power collection, wideband antennas are generally used to collect thermal noise over a wide frequency range. We previously demonstrated that small (7 cm diameter) log-spiral antennas are sensitive in a wideband to temperature variations in deep-seated targets [31-34]. We then choose the log-spiral design as a base for our radiometric sensor but in order to be conformal with the human head we move to a smaller size, approximately 2.5 cm diameter. Though small antennas (relative to the wavelength) are not as efficient at collecting low frequency emissions, high frequency waves do not penetrate as far in tissue due to high attenuation losses. So for each microwave antenna and target there is an optimal frequency band to collect maximum energy emitted from the target tissue.

The key innovation of this project is the integration of two critical components: a small (2.5 cm diameter) receive antenna specifically optimized with electromagnetic simulation software (HFSS v15 - Ansys, Canonsburg, PA) for temperature measurement of deep regions in the human head; and a high performance [1.1, 1.6] GHz microwave radiometer with miniature chip components soldered in a printed circuit board that is mounted on the back of the antenna. The radiometer circuit achieves high sensitivity and noise rejection using a dual-matched and ultra-low noise high gain amplifier. The receive antenna is connected directly with the front stage amplifier for high sensitivity while providing a time sequenced comparison to internal temperature reference for long term stable calibration (see Figure 3.1). The entire sensor package is contained in a lightweight and low profile 2.8 cm diameter by 1.5 cm high assembly that can be held in place over the skin with an electromagnetic interference (EMI) shielding adhesive patch and/or elastic strap.

In this paper we focus on the theory and modeling efforts for the design of the 2.5 cm receive antenna and frequency selection for radiometric brain temperature monitoring. Description of radiometer electronics [18-20, 36] and clinical implementation [37] can be found elsewhere. To validate and demonstrate performance of this sensor, we build a realistic model (phantom) of the human head with separate brain and scalp regions consisting of tissue equivalent liquids circulating at independent temperatures on either

side of an intact skull phantom. This life size model of the human head allows simulation of differential surface and deep tissue temperatures and thus can mimic real temperature gradients that exist throughout the head during surgery.

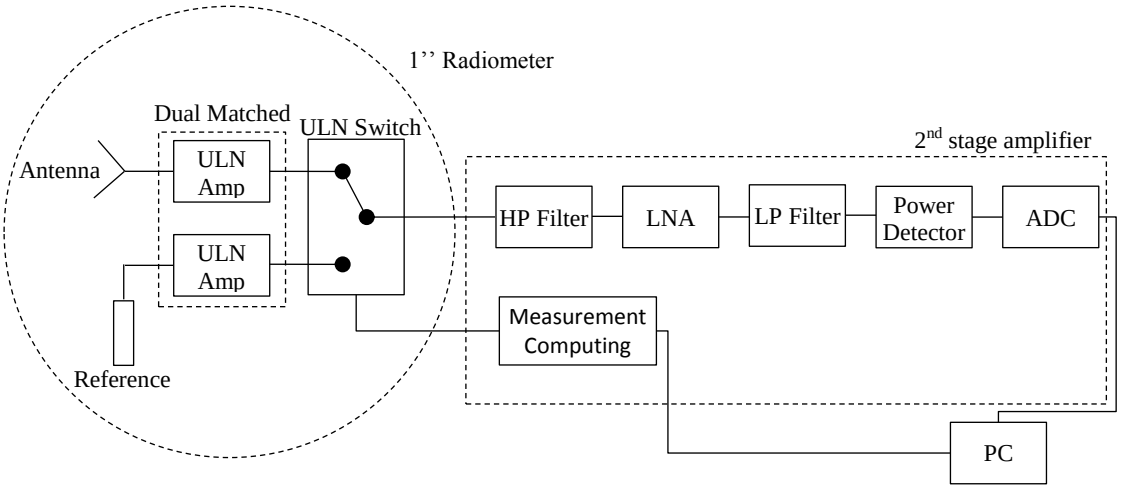

Figure 3.1 – Block diagram of the radiometer. ULN Amp = ultra-low noise amplifier, LNA = low-noise amplifier, HP = high pass, LP = low pass and ADC = analog-to-digital converter.

3.2. Methods

3.2.1. Log-spiral antenna design

Rumsey's principle [38] states that the impedance and pattern properties of an antenna will be frequency-independent if the antenna shape is specified only in terms of angles. Logarithmic spiral (log-spiral) antennas fit these requirements and present frequency-independent properties over a wide bandwidth Δf determined by the finite physical dimensions of the antenna [39, 40]. The log-spiral design here explored consists of a single arm curved surface limited by edges ρ_{e0} (inner) and ρ_{e1} (outer) defined by

$$\begin{cases} \rho_{e0} : \rho = \rho_0 e^{a\theta} \\ \rho_{e1} : \rho = \rho_1 e^{a\theta} \end{cases} \quad (1)$$

where (ρ, θ) are polar coordinates; $\rho_0 = 0.25$ mm and $\rho_1 = 0.75$ mm are the initial ($\theta = 0$) inner and outer radius, respectively, determined by the coaxial feed port; and a is the spiral growth rate coefficient defined by the number of log-spiral turns (N) allowable within the surface described by ρ_{e0} and ρ_{e1}. The end of the spiral arm is tapered (see Figure 3.2) to minimize reflections at lower frequencies and improve impedance

matching [41]. Due to clinical restrictions on size, the outermost radius (ρ_{ext}) of the tapered spiral surface is fixed at 12.5 mm. The growth rate coefficient can then be defined as a function of the log-spiral turns as follows:

$$a(N) = \frac{\ln\left(\rho_{ext}/\rho_0\right)}{2\pi N} \tag{2}$$

where $2\pi N$ corresponds to the maximum angle (θ_{max}) of rotation in the spiral design.

The second design principle for frequency-independent antennas is the use of self-complementary structures since they present a constant input impedance [40]. For the log-spiral design this condition occurs when the shape of the spiral is equal to the shape formed by the space between the spiral metal trace. In our particular design, the feed point determined by ρ_0 and ρ_1 does not allow a perfect self-complementary structure, but it can still be approximated to obey this second principle. By equating the area of the spiral surface – extracted from equations (1) and (2) – and its complement within the radius ρ_{ext}, the result is N = 1.8 turns. Instead of using this theoretical result, we will perform a parametric analysis over N to assess the chosen principles underlying the antenna design and also study its effect on the antenna's radiation pattern.

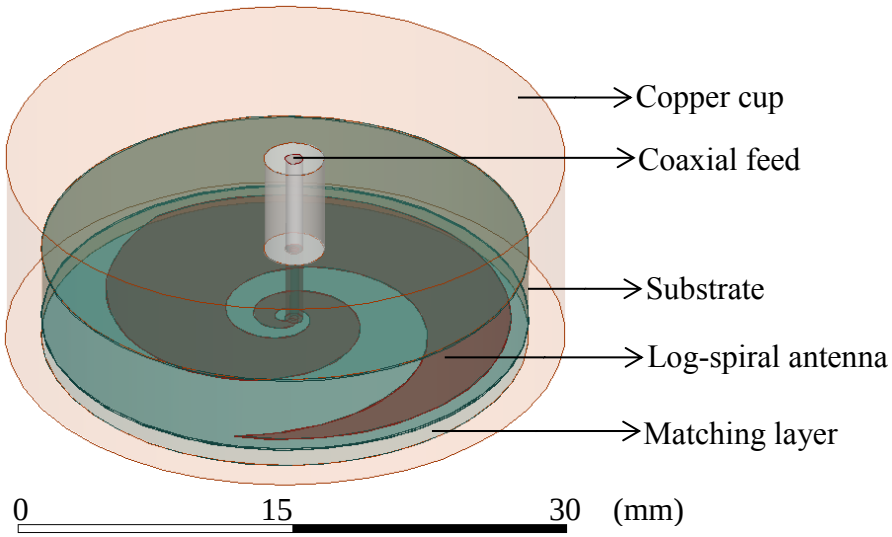

Figure 3.2 – Radiometric receive antenna: microstrip log-spiral patch design with tapered ends.

The final design principle relies on the desired nonlinear polarization pattern of the antenna. Since the function of the antenna is to collect thermal radiation, which is randomly polarized, it is desirable for the antenna to have circular or elliptical rather

than linear polarization. When the antenna arm length is shorter than one wavelength, polarization is linear. As the arm length is increased (or frequency increased) the polarization becomes nonlinear [39, 42]. To be an efficient radiator, the spiral length must be at least similar to the wavelength. The arm length $L(N)$ must be determined over the line defined by ρ_{e0} (equation (1)), which is given by

$$L(N) = \left(\rho_{ext} - \rho_0\right)\frac{\sqrt{1+a^2(N)}}{a(N)} \tag{3}$$

The planar log-spiral antenna structure presents a bidirectional radiation pattern [41, 43], where it collects energy from both its surface normals. By placing an absorbing material in the cavity behind the spiral antenna trace, the antenna would exhibit a unidirectional pattern [41]. Using this method, however, the antenna is no longer sensitive in one of its surfaces. Instead of using an absorber, our design includes a hydrocarbon ceramic substrate of 4.45 mm thickness that is used to refocus the outward beam towards the target (brain). Three different substrates are chosen from the RO3000© series (Rogers Corp., USA) due to availability, easiness of construction, non-dispersive high dielectric permittivity and, more important, ultralow loss (see Table 3.1) that is desirable for radiometric applications.

Table 3.1 – Ceramic substrates used in the antenna design.

Substrate	**Permittivity ε_r**	**Conductivity σ (S/m)**
RO3003©	3.00	2.93×10^{-4}
RO3006©	6.15	9.23×10^{-4}
RO3010©	10.20	1.68×10^{-3}

The presence of a high dielectric substrate in the back of the antenna will affect the wavelengths detectable by the log-spiral trace and thus the antenna's operating bandwidth Δf. According to Kaiser's *ring theory* [44], the lower cut-off frequency f_L is a function of the circumference length with radius ρ_{ext} ($2\pi\rho_{ext}$) and the higher cut-off frequency f_H is dependent on the fineness of the construction at the feed point (ρ_1 - ρ_0):

$$\begin{cases} f_H = \dfrac{c}{2\pi\left(\rho_1 - \rho_0\right)\sqrt{\varepsilon_{r,eff}}} \\ f_L = \dfrac{c}{2\pi\rho_{ext}\sqrt{\varepsilon_{r,eff}}} \end{cases} \quad (4)$$

where c = 299792458 m/s is the speed of light and $\varepsilon_{r,eff}$ is the effective permittivity that affects the wavelengths detected by the antenna.

The final element of the antenna is a thin matching layer (coverlay) placed between the antenna and load (human head). The intention is to improve antenna match impedance to tissue and isolate the metal from the conductive skin. Its dielectric properties and thickness (δ) as well as the log-spiral turns will be subject to a parametric analysis (Table 3.2) to assess the influence of these parameters on the antenna performance. We choose the Eccostock® HiK500F series (Emmerson&Cumming, Randolph, MA, USA) for the same reasons pointed out for the substrate.

Table 3.2 – Log-spiral antenna parameters for parametric analysis.

Property	**Parametric analysis**
Coverlay permittivity $\varepsilon_{r,coverlay}$	5, 10, 15, 20, 25, 30, 35 and 40
Log-spiral turns N	0.25, 0.5, 0.75, 1, 1.25, 1.5, 1.75, 2, 2.25, 2.5 and 2.75
Coverlay thickness $\delta_{coverlay}$ (mm)	0, 0.5, 1, 2, 3 ,4 and 5

3.2.2. Radiometry antenna efficiency

From the reciprocity theorem [45], the received pattern of the antenna is proportional to the power deposition in the target that is a function of the electric field (***E***-field). The ***E***-field maintained by the antenna is calculated by solving the wave equation derived from Maxwell's equations assuming a time-harmonic electric field $\boldsymbol{E}_i(\boldsymbol{r},t)=\boldsymbol{E}_{0i}(\boldsymbol{r})\exp(j\omega t)$, which is given by

$$\nabla^2\boldsymbol{E}_{0i}\left(\boldsymbol{r}\right)+\omega^2\mu_0\varepsilon_0\varepsilon_{ci}\boldsymbol{E}_{0i}\left(\boldsymbol{r}\right)=\boldsymbol{0} \quad (5)$$

where

$$\nabla^2\boldsymbol{E}_{0i}\left(\boldsymbol{r}\right)=\nabla^2E_{0ix}(\boldsymbol{r})\boldsymbol{e}_x+\nabla^2E_{0iy}(\boldsymbol{r})\boldsymbol{e}_y+\nabla^2E_{0iz}(\boldsymbol{r})\boldsymbol{e}_z \quad (6)$$

and that is solved using the finite element method (FEM) in HFSS. In equation (5) ε_0 and μ_0 are free space dielectric permittivity (8.854×10^{-12} F/m) and magnetic permeability (1.257×10^{-6} N/A^2), respectively, $\varepsilon_{ci} = \varepsilon_{ri} - j\sigma_i/(\omega\varepsilon_0)$ is the complex dielectric permittivity that is modeled to be homogeneous within each medium and $\omega = 2\pi f$ is the angular frequency (Hz). Moreover E_{0il} ($l = x,y,z$) are the components of the electric field $\boldsymbol{E}_{0i}$. Note that equation (5) is only valid for non-magnetic materials (e.g., biological tissues or plastic phantom materials) where magnetic permeability is approximated to μ_0 [46]. The subscript i represents each individual region ($1 \leq i \leq n$, $n \in \mathbb{N}$ with n the number of regions) in the computational domain that includes both the antenna and mouse. For convenience, we drop the subscript i throughout this chapter except in the numbered equations.

A typical microwave (MW) radiometer collects thermal radiation from biological tissues using an antenna in the lower spectrum of microwaves ([1, 5] GHz). In this MW band, thermal emissions received at the antenna input of the radiometer are small, with power spectral density of the order of 10^{-14} W/MHz, and have to be amplified and processed by low loss, low noise and high gain MW components to retrieve the temperature of the target tissue [31, 33, 34, 47]. When connected to a radiometric receiver and loaded by a non-isothermal and lossy medium (human tissue), the MW antenna will measure an equivalent temperature (T_B) determined from the weighted volumetric average temperature within the sense region of the antenna. The power collected by the antenna (P_{ant}) is directly proportional to T_B and is given by [45]

$$P_{ant} = Gk_BT_B\Delta f \tag{7}$$

where k_B is the Boltzmann constant (1.381×10^{-23} J/K) and G is the radiometer total gain.

The temperature measured by the radiometer in the band Δf is given by

$$T_B = \left(1-|\Gamma|^2\right)\left(\sum_{i=1}^{n}\left(\int_{V_i} W_i(\boldsymbol{r})T_i(\boldsymbol{r})\,dV_i\right)+T_{EMI}\right)+|\Gamma|^2\,T_{REC} \tag{8}$$

where $T(\boldsymbol{r})$ is the physical temperature in the human tissue located at the position $\boldsymbol{r}$ within a sensing volume V, T_{REC} is the radiometer receiver noise temperature, T_{EMI} is the electromagnetic interference collected by the antenna from the surrounding environment, and $|\Gamma|^2$ is the power reflection coefficient due to mismatch at the interface between the antenna and lossy media (load). Moreover W is defined as follows:

$$W_i(\boldsymbol{r}) = \frac{P_{di}(\boldsymbol{r})}{\int_{V_i} P_{di}(\boldsymbol{r})\, dV_i} \text{ with } \sum_{i=1}^{n}\left(\int_{V_i} W_i(\boldsymbol{r})\, dV_i\right) = 1 \tag{9}$$

$$P_{di}(\boldsymbol{r}) = \frac{1}{2}\sigma_i \left|\boldsymbol{E}_{0i}(\boldsymbol{r})\right|^2 \tag{10}$$

W is a weighting function and is determined from the power loss density P_d (W/m^3) that is the same as the received power density from reciprocity theorem [45]. The power loss density depends on both the electrical conductivity σ (S/m) and the electric field $\boldsymbol{E}_0$ (V/m) inside the sensing volume V. The goal of the radiometer is to retrieve target temperature $T(\boldsymbol{r})$ while reducing the contribution of external electromagnetic interference (T_{EMI}) by proper EMI shielding and low noise MW components to reduce T_{REC}. The radiometric sensor includes a copper cup (Figure 3.2) that completely surrounds the antenna and guides the received pattern from deeper tissue, thereby shielding out EMI or extraneous received signal around the antenna. The copper cup also shields out EMI from the radiometer front stage electronics which is located in the cavity behind the antenna ground plane [31]. The design of the antenna must also minimize the mismatch (S_{11}) between antenna and tissue load as well as maximize the antenna's efficiency. The S_{11} values are here given in decibels as follows:

$$S_{11}(dB) = 20\log_{10}\left(\left|\Gamma\right|\right) \tag{11}$$

where Γ is the input voltage reflection coefficient [48]. Efficiency is here evaluated in terms of the ratio of power received from the brain to the total power received by the antenna:

$$\eta = \frac{\int_{V_{Brain}} P_{d,Brain}(\boldsymbol{r})\, dV_{brain}}{\sum_{i=1}^{n}\left(\int_{V_i} P_{di}(\boldsymbol{r})\, dV_i\right)}, \quad V_{BRAIN} \subset V \tag{12}$$

A final parameter to be optimized is the antenna's bandwidth Δf (Table 3.3). As mentioned, increasing the bandwidth will maximize the power collection of thermal noise from tissue. For convenience, we define $\eta_{\Delta f}$ as the average efficiency over Δf where $S_{11} \leq$ -10 dB. This function ($\eta_{\Delta f}$) will be used to compare different parametric analyses.

Table 3.3 – Log-spiral antenna optimization goal functions.

Function	Goal
Efficiency η	Maximization
Bandwidth Δf	Maximization

Furthermore, some frequency bands must be avoided due to excessive environmental background interference. These parasitic signals reside on the bands allocated by the Federal Communications Commission (FCC) and include wireless local area networks, mobile phones, and pagers that are regularly found in hospitals [49, 50]. Ideally, reception at these frequencies can be shielded or filtered to minimize EMI contamination of the radiometric signal from target. Table 3.4 presents all constraints associated with the optimization problem where we define a maximum power reflection coefficient of -10dB.

Table 3.4 – Log-spiral antenna optimization constraints.

Parameter	Constraint
S_{11}	$\leq$ -10dB
Initial spiral inner radius ρ_0	0.25 mm
Initial spiral outer radius ρ_1	0.75 mm
Outermost spiral radius ρ_{ext}	12.5 mm
FCC allocated frequencies	[0.81, 0.96], [1.71, 1.99] and [2.4, 2.5] GHz

3.2.3. Experimental human head phantom model

The antenna design optimization requires a specific-target head phantom model. From analysis of x-ray computed tomography (CT) scans of an unidentified patient head, we determined realistic values for the thickness of scalp, bone, and brain tissues for our physical model. Measurements show that scalp thickness varies from 4.2 mm (forehead) to 8 mm (temporal lobe), and the thickness average of skull bone is 6.7 mm in both regions. Based on these dimensions, an experimental model of the human head is constructed (Figure 3.3) around an artificial human skull (Life Size Skull, www.anatomywarehouse.com).

To model the thermodynamics of scalp which is a mixture of skin, muscle and fat tissues, an adjustable thickness ([6, 16] mm) compartment was sealed against the outer surface of the skull and filled with circulating distilled water that is temperature controlled. To simulate brain, a mixture of propylene glycol (46%) and deionized water (54%) is used to approximate the electrical properties of mixed grey and white matter. The brain liquid phantom is circulated vigorously with a peristaltic pump through a latex balloon that fills the interior of the skull; temperature is controlled with a heat exchanger. Temperatures of the scalp and brain compartments are controlled independently to obtain realistic differential temperature of surface and deep tissues as in surgery. The circulation velocity is 1.7 liter/min in both liquid phantoms to ensure homogeneous "brain" and "scalp" temperatures.

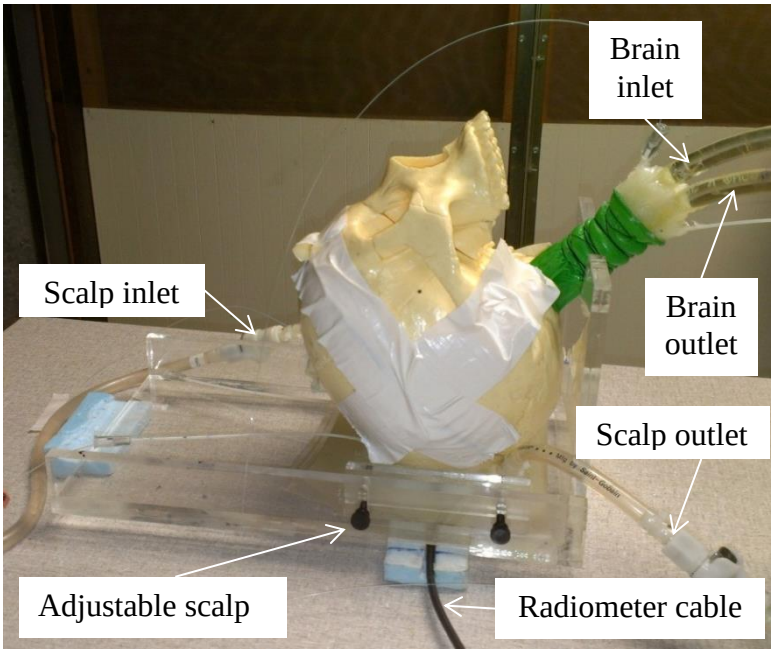

Figure 3.3 – Human head model with variable brain liquid phantom temperature. This liquid circulates through a balloon that fills the inside of the skull. The scalp liquid phantom is also temperature controlled and circulates in a region under the skull with adjustable thickness. The black cable leads to a radiometric antenna sensor that is coupled to scalp.

Electrical properties (relative permittivity ε_r and electrical conductivity σ) for both liquid phantoms are characterized at normothermic temperatures for scalp (32 °C) and brain (37 °C) using a coaxial dielectric probe (E85070C, Agilent Technologies, Santa Rosa CA) connected to a network analyzer (E5071C, Agilent Technologies). Figure 3.4 shows the measured electrical properties of the phantom materials (dotted lines) along

with corresponding human tissue properties (solid lines) taken from the literature [51]. The electrical properties of the scalp phantom could be approximated to human properties by using an appropriate mixture of ethylene glycol and water [52]. However, ethylene glycol deteriorates both tubing and air bubble traps used in the circulation system. In our closed-system setup, air bubble traps are essential to avoid accumulation of air bubbles in critical regions of the model that affect radiometric sensing.

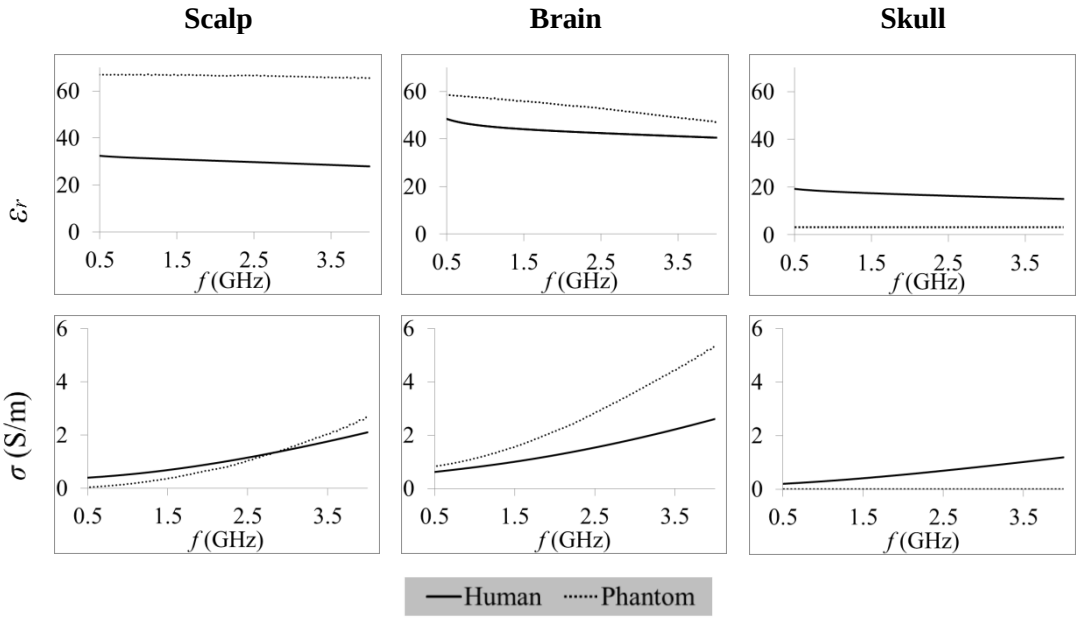

Figure 3.4 – Frequency dependent electrical properties (relative permittivity and electrical conductivity) of both phantom and human tissues. Liquid phantoms are measured at normothermic temperatures: 32 °C for scalp phantom and 37 °C for brain phantom. The dielectric property of plastic skull is practically constant over the temperature range of interest.

3.2.4. Virtual human head computational model

The physical phantom is translated into an anatomically accurate CAD (computer-aid design) model. CT images of the plastic skull are acquired and segmented using Avizo (Visualization Sciences Group, Burlington, MA). The resulting 3D surfaces of the surrogate skull are assumed to be the outer boundary of a uniform volume of tissue. The remaining objects are created in Ansys DesignModeler (Ansys Inc., Philadelphia PA) with accurate geometry and dimensions. The final virtual phantom (Figure 3.5a) is then imported into HFSS and coupled with the antenna to perform a simulation-based optimization. The antenna is placed under the occipital region of the skull with a thin layer of mylar (0.1 mm thickness) between the antenna and the scalp liquid phantom (Figure 3.5b).

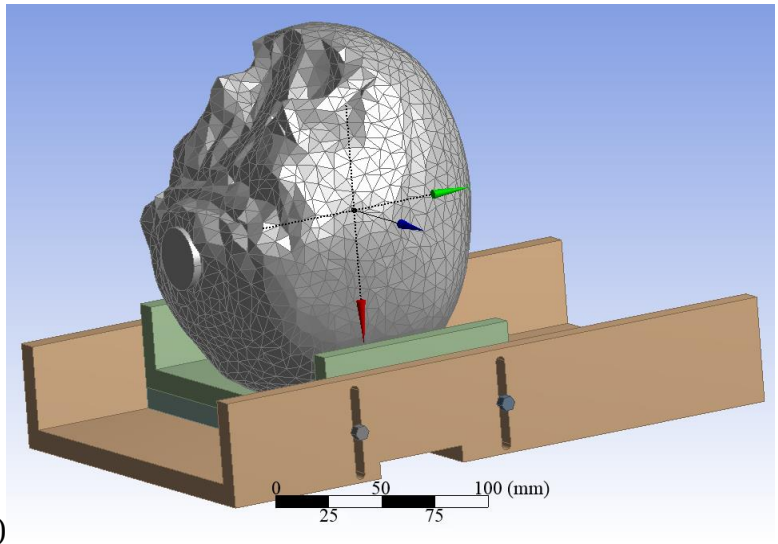

a)

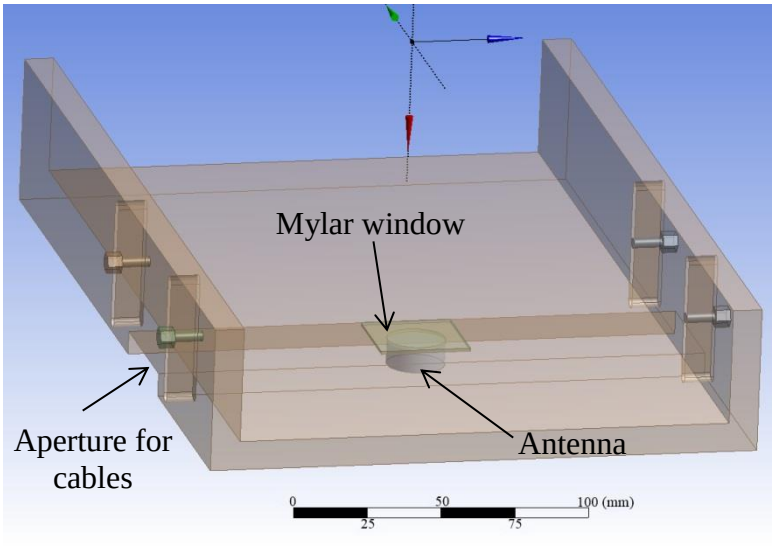

b)

Figure 3.5 – Computational model of the multilayered human head phantom used for antenna optimization (a) and isolated 3D view for the Mylar and microwave antenna location (b).

The measured electrical properties of the liquid phantoms (Figure 3.4), that are frequency dependent, are assigned to the corresponding objects in the model. The electrical properties for each solid object are practically non dispersive and presented in Table 3.5.

Table 3.5 – Electrical properties of the solid materials used in the phantom and antenna setup.

Material	**Usage**	ε_r	σ **(S/m)**
Mylar	Antenna/scalp interface	2.8	1.68×10^{-3}
Plexiglass	Supporting structures	2.6	2.65×10^{-3}
PVC	Bolus bag	3.2	3.24×10^{-3}
Copper	Antenna trace/cup	1.0	5.80×10^{7}

A discrete frequency sweep is used with a 0.05 GHz step to simulate ***E***-field. The solutions at the remaining frequency points are interpolated. The computational model is meshed automatically by HFSS and consists of approximately 120 thousands tetrahedral elements. We use a tangential element basis function of the first order to interpolate field values from both nodal values at vertices and on edges. First order basis functions use 20 unknowns per tetrahedron with quadratic interpolation. In HFSS the initial edge length l_t of each tetrahedral element is determined from the material's relative permittivity ε_r and operating frequency f using $l_t = c/(3 \cdot f \cdot (\varepsilon_r)^{1/2})$. The mesh is then automatically refined based on the computed ***E***-field to obey a maximum deltaS = 0.02, where deltaS is the change in the magnitude of the scattering parameters (S_{11}) between two consecutive iterations. We surround the virtual head phantom with an air domain to study the possibility of developing ***E***-fields surrounding the antenna. An absorbing boundary condition (named radiation boundary in HFSS) is imposed at the boundaries of the full computational domain. This boundary condition guarantees that none of the wave propagating to the boundary is reflected back into the computational domain [48]. This computational method has been validated experimentally in similar antennas [31, 33, 34, 47].

3.2.5. Antenna measurements

Once the design optimization is complete, the antenna is manufactured, connected with the radiometer electronics (see Figure 3.1) [18-20] and tested in the physical phantom. An initial steady state condition is established in the head phantom by circulating 32 °C scalp liquid phantom through the bolus covering the skull surface and 37 °C brain liquid phantom through the latex balloon filling the skull's interior. Circulation is maintained for approximately 50 min with the head at thermal equilibrium and the radiometer stable. After this plateau, the temperature of the circulating brain phantom is abruptly decreased by 10 °C while maintaining the scalp at constant 32 °C for approximately 90 min. We maintain the scalp constant to ensure that the radiometric reading is independent from scalp. Radiometric power (P_{ant}) is measured continuously and converted into equivalent temperature (T_B) as discussed previously in equations (7)-(10). Through a calibration algorithm developed by Maccarini *et al.* [36], brain temperature is extracted from the complete T_B signal. This procedure has been derived from previous

methodology reported in the literature [29, 53]. To demonstrate the accuracy and stability of radiometric readings over an extended time, such as a long open heart surgeries that can last up to 7 hours or more, the circulating brain temperature is increased abruptly of 10 °C back to its original baseline (37 °C) and maintained steady for an additional 2 hours. Temperatures of both phantom tissues are continuously monitored using fiber optic probes (Luxtron 3100, LumaSense Technologies, Santa Clara, CA) for comparison with the radiometric readings.

3.2.6. Error and statistical analyses

The radiometric signal is smoothed using a 200-point moving median in order to eliminate the short-term amplitude fluctuations from EMI environmental noise. The accuracy of the radiometer is determined by the measurement error, defined by the difference between brain temperature measured by the fiber optic and the radiometric sensor. The statistical analysis of the error is implemented in each segment of the experiment: (a) initial steady state at 37 °C; (b) cooling from 37 °C to 27 °C; (c) steady state plateau at 27 °C; (d) rewarming from 27 °C to 37 °C; and (e) a final steady state plateau at 37 °C. The minimum, maximum, amplitude, average and standard deviation (SD) values of the difference between radiometer and fiber optic measured brain temperatures are presented for each segment and for the entire experiment. The amplitude of the error function corresponds to half the peak-to-peak variation between minimum and maximum values of error.

3.2.7. Clinical Correlation

Under an IRB (Institutional Review Board) approved protocol, a radiometric sensor is placed on the temple of a one-year-old male patient undergoing a mitral valvulotomy surgery in order to monitor radiometric measure of brain temperature. Scalp and brain temperatures are monitored continuously throughout the 120 minute surgical procedure while the patient is cooled approximately 6 °C and subsequently rewarmed. The calculated radiometric brain core temperature is compared with nasopharyngeal and rectal core temperatures recorded manually by the anesthesiologist during the procedure. As is typical in this operating room, the body temperatures are charted with 1

°C precision at, approximately, 15 min intervals, providing a general reference for changes in body temperature during the 2-hour surgery. The radiometer setup protocol to be used by physicians or nurses can be found in the Appendix 3.

3.3. Results

3.3.1. Antenna bandwidth simulations

From simulations we can conclude that both the S_{11} and efficiency (η) are independent of coverlay permittivity in the range $\varepsilon_{r,coverlay}$ = [5,40]. Thus, we choose $\varepsilon_{r,coverlay}$ = 30 due to availability. In the following simulations we fix $\delta_{coverlay}$ = 1 mm [54] since this parameter is not as critical as $\varepsilon_{r,substrate}$ or the log-spiral turns N. Thus, once chosen the optimal $\varepsilon_{r,substrate}$ and N, a parametric analysis for $\delta_{coverlay}$ will be implemented in order to refine the results.

Figure 3.6 presents the operating bandwidth Δf for which $S_{11} \leq$ -10 dB and compares the results for the three substrates under analysis: RO3010 ($\varepsilon_{r,substrate}$ = 10.2), RO3006 ($\varepsilon_{r,substrate}$ = 6.15) and RO3003 ($\varepsilon_{r,substrate}$ = 3). Increasing substrate permittivity improves the operating bandwidth but this increase is not linear over the number of log-spiral turns (Figure 3.6a). Best results are achieved for N = 2 (RO3010) and N = 2.25 (RO3006 and RO3003). Substrate RO3010 achieves the overall 530 MHz maximum bandwidth in the range [1.1, 1.6] GHz (Table 3.6), which is outside the FCC allocated frequency bands. Average efficiency along Δf denoted by $\eta_{\Delta f}$ is presented in Figure 3.6b: substrates RO3010 and RO3006 present similar efficiency over N and, overall, increasing substrate permittivity improves the efficiency of the antenna. Combining the high efficiency and large bandwidth we choose $\varepsilon_{r,substrate}$ = 10.2 (RO3010) and N = 2 as nominal values for the remaining simulations.

a) 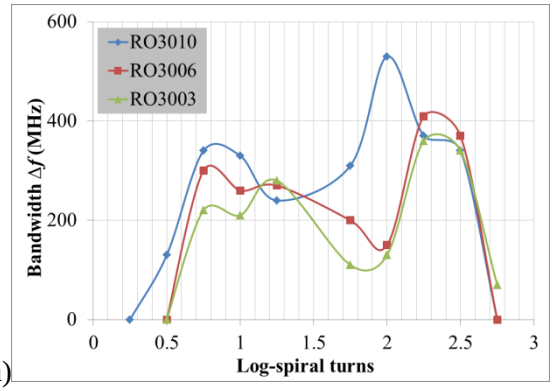

b) 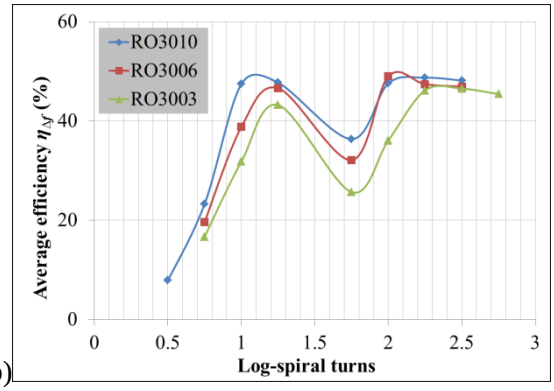

Figure 3.6 – Determination of the operating frequency bandwidth Δf where $S_{11} \leq$ -10 dB for substrates RO3010 ($\varepsilon_{r,substrate}$ = 10.2), RO3006 ($\varepsilon_{r,substrate}$ = 6.15) and RO3003 ($\varepsilon_{r,substrate}$ = 3): a) Δf *vs*. log-spiral turns and b) average antenna efficiency $\eta_{\Delta f}$ *vs*. log-spiral turns. Nominal values: $\delta_{coverlay}$ = 1 mm and $\varepsilon_{r,coverlay}$ = 30.

For convenience, we define f_l and f_h as the upper and lower frequency limits of the operating bandwidth Δf where $S_{11} \leq$ -10 dB. Please note that the cut-off frequencies f_L and f_H defined in equation (4) are not limited to the condition $S_{11} \leq$ -10 dB and occur outside Δf, yielding $f_L < f_l$ and $f_H > f_h$. Table 3.6 presents f_l and f_h frequencies for all the bandwidths presented in Figure 3.6.

Table 3.6 – Lower f_l and upper f_h frequencies for which $S_{11} \leq$ -10 dB for different log-spiral turns.

	RO3010		**RO3006**		**RO3003**	
N	f_l (GHz)	f_h	f_l (GHz)	f_h	f_l (GHz)	f_h
0.5	2.64	2.77	-	-	-	-
0.75	1.60	1.94	1.70	2.00	1.84	2.06
1	1.27	1.6	1.41	1.67	1.54	1.75
1.25	1.18	1.42	1.20	1.47	1.26	1.54
1.75	1.52	1.83	1.64	1.84	1.77	1.88
2	1.13	1.66	1.23	1.38	1.61	1.74
2.25	1.17	1.54	1.16	1.57	1.25	1.61
2.5	1.22	1.56	1.16	1.53	1.19	1.53
2.75	-	-	-	-	1.18	1.25

The next two figures show the antenna reflection coefficient (S_{11}) and efficiency of the tapered log-spiral antenna over [0.5, 3.0] GHz for different parametric analysis: number

of log-spiral turns (Figure 3.7) and substrate permittivity (Figure 3.8). These plots are representative examples of all the studies presented in Table 3.6. One can observe that increasing the number of log-spiral turns leads to an overall decrease of both f_l and f_h; increasing substrate permittivity has the same effect. The lower cut-off frequency can be extrapolated from these plots and corresponds to the frequency where S_{11} decreases abruptly: f_L is 0.98 GHz and independent on the number of log-spiral turns (Figure 3.7a), but varies from 0.98, 1.05 to 1.09 GHz (Figure 3.8a) while changing substrate permittivity $\varepsilon_{r,substrate}$ = 10.2, 6.15 and 3.0, respectively. Although efficiency results in specific bands can present significant changes (Figure 3.6b), the efficiency within the implemented parametric analysis does not present significant differences along frequency (Figures 3.7b and 3.8b).

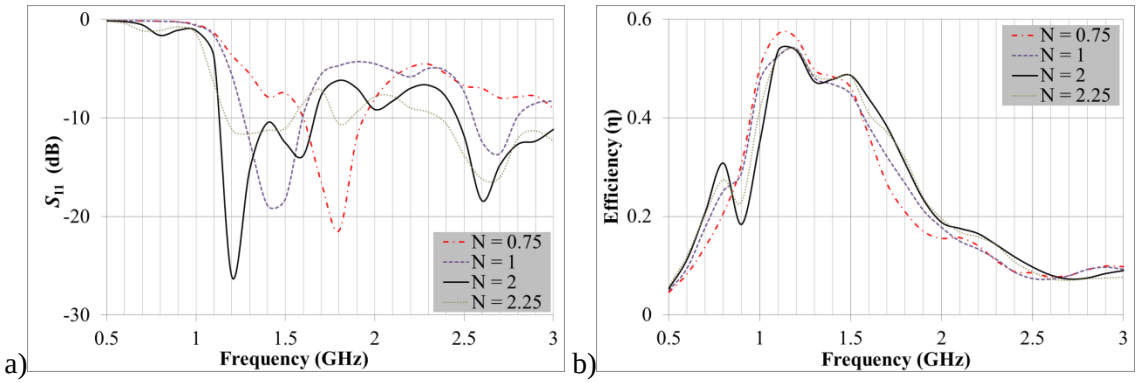

Figure 3.7 – Log-spiral turns (N) parametric analysis over frequency for a) S_{11} and b) efficiency (η). Nominal values: $\varepsilon_{r,substrate}$ = 10.2, $\delta_{coverlay}$ = 1 mm and $\varepsilon_{r,coverlay}$ = 30.

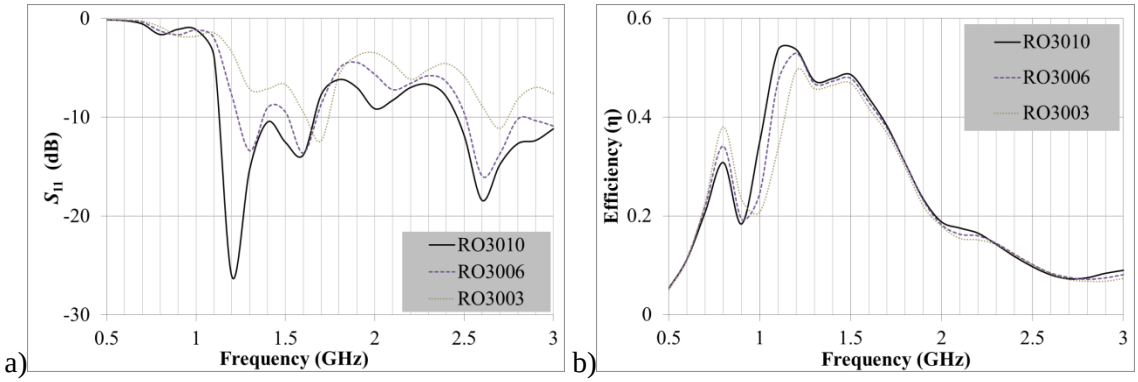

Figure 3.8 – Substrate permittivity parametric analysis over frequency for a) S_{11} and b) efficiency (η). Substrate permittivities are $\varepsilon_{r,substrate}$ = 10.2 (RO3010), $\varepsilon_{r,substrate}$ = 6.15 (RO3006) and ε_r = 3 (RO3003). Nominal values: N = 2, $\delta_{coverlay}$ = 1 mm and $\varepsilon_{r,coverlay}$ = 30.

From the previous results we chose substrate RO3010 ($\varepsilon_{r,substrate}$ = 10.2) and N = 2. The parametric analysis for $\delta_{coverlay}$ is then chosen to refine the previous results. Figure 3.9 presents the parametric analysis results of the tapered log-spiral antenna over [0.5, 3.0] GHz for different coverlay thicknesses. The S_{11} parameter is presented in Figure 3.9a and efficiency (η) in Figure 3.9b. Simulations are implemented with substrate RO3010, N = 2 and $\varepsilon_{r,coverlay}$ = 30. The frequency range where $S_{11} \leq$ -10 dB is not as sensitive to the coverlay thickness (Figure 3.9a) as it is to the substrate permittivity or the log-spiral turns (Figures 3.7 and 3.8). The average efficiency over the operating bandwidth correspondent to $S_{11} \leq$ -10 dB is fairly constant ($\pm$1 %) in the interval $\delta_{coverlay}$ = [1, 5] mm (Table 3.7). The maximum efficiency $\eta_{\Delta f}$ = 51.4% is obtained for a thick coverlay of $\delta_{coverlay}$ = 3 mm but the correspondent bandwidth is only 420 MHz, whereas the 1 mm coverlay allows 530 MHz and $\eta_{\Delta f}$ = 50.3% (Table 3.7). The 1 mm coverlay is then the best tradeoff and is chosen to fabricate the antenna. This configuration leads to an [1.1, 1.6] GHz operating band.

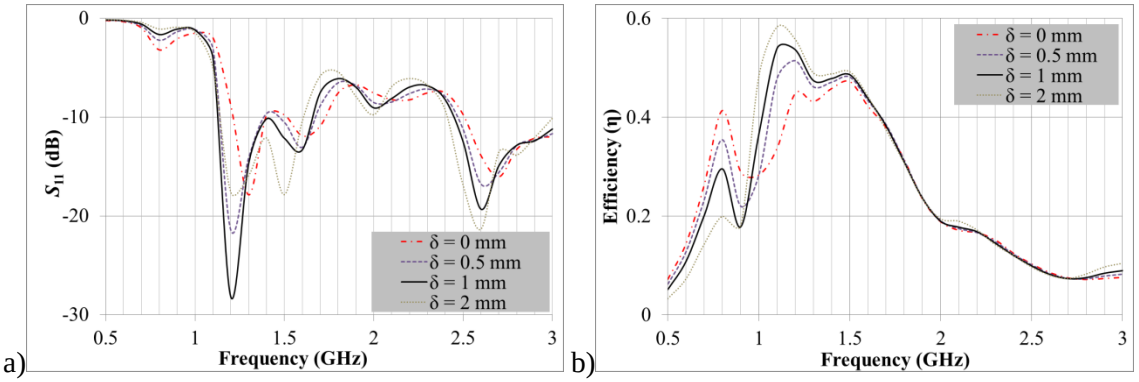

Figure 3.9 – Coverlay thickness (δ) parametric analysis to improve impedance matching at the interface between antenna and human head. a) S_{11} *vs.* frequency and b) antenna efficiency *vs.* frequency. Nominal values: N = 2, $\varepsilon_{r,coverlay}$ = 30 and $\varepsilon_{r,substrate}$ = 10.2.

Table 3.7 – Effect of coverlay thickness on the lower f_l and upper f_h frequencies for which $S_{11} \leq$ -10 dB as well as for the average efficiency over [f_l, f_h].

$\delta_{coverlay}$ (mm)	f_l (GHz)	f_h (GHz)	Δf (GHz)	$\eta_{\Delta f}$ (%)
0	1.21	1.39	180	44.6
0.5	1.14	1.38	240	48.1
1	1.13	1.66	530	50.3
2	1.14	1.61	470	50.9
3	1.16	1.58	420	51.4
4	1.19	1.54	350	50.0
5	1.27	1.48	210	49.7

3.3.2. Simulated radiation patterns

Figure 3.10 shows the power loss density P_d (W/m^3) of the optimized tapered log-spiral antenna at the center frequency (1.35 GHz), extremes (1.1 and 1.6 GHz) and outside the optimized radiometric band [1.1, 1.6] GHz, *i.e.*, 1.0 and 2.0 GHz. The efficiency η (%) is also shown for these values of frequency. Within the range [1.1, 1.6] GHz, simulations demonstrate that although the radiometer is sensitive to scalp temperature, a significant portion of the microwave energy is received from deep brain regions. As expected, there is little power deposited in (or received from) the bone due to its very low electrical conductivity. Below 1.0 GHz the antenna is inefficient because of the limited size compared to the wavelength. This improves EMI immunity from parasitic frequencies at [810, 960] MHz. At higher frequencies (2.0 GHz), the energy received by the antenna is collected mainly from the scalp.

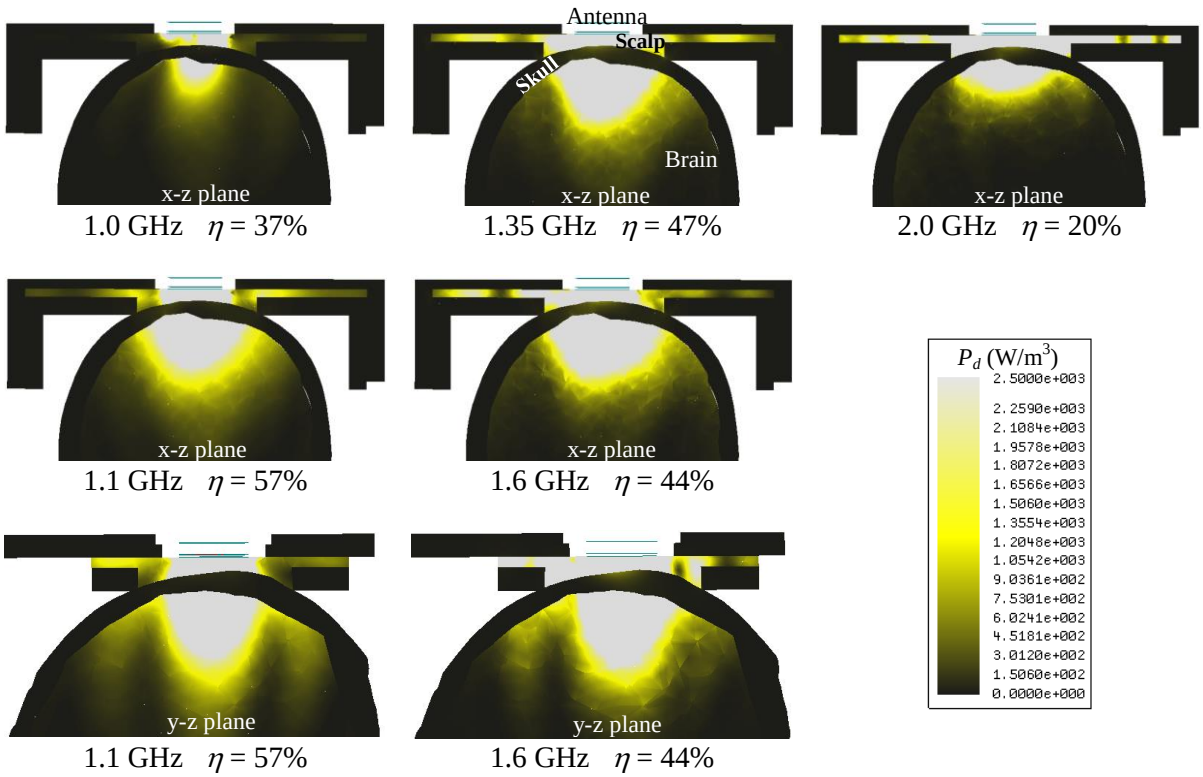

Figure 3.10 – HFSS-simulated receive pattern for the 2.5 cm log-spiral antenna when placed on the heterogeneous multilayer human head model. The receive pattern is shown for five specific radiometric sensing frequencies, *i.e.*, 1.0, 1.1, 1.35, 1.6 and 2.0 GHz. Radiometric antenna efficiency η (%) is evaluated in terms of the ratio of the power collected from brain to the total power received by the antenna and thus intrinsically normalized.

The depth profile of power loss density (MW/m^3), calculated at the same frequencies as Figure 3.10 (1.0, 1.1, 1.35, 1.6 and 2.0 GHz), is shown in Figure 3.11. Increasing frequency corresponds directly to a higher power collection from scalp. On the other end, the same behavior does not occur for the power collected from brain. In this case, after an initial increase, the power loss density starts to decrease above 1.6 GHz (Figures 3.11 and 3.12). At 2.0 GHz (Figure 3.11) one can observe more power collection from brain than at 1.0 GHz, but that does not imply that the antenna is more efficient. Moreover, at 2.0 GHz the antenna collects significantly more power from scalp than at 1.0 GHz. However, the antenna efficiency is higher at 1.0 GHz than at 2.0 GHz (Figures 3.10 and 3.11).

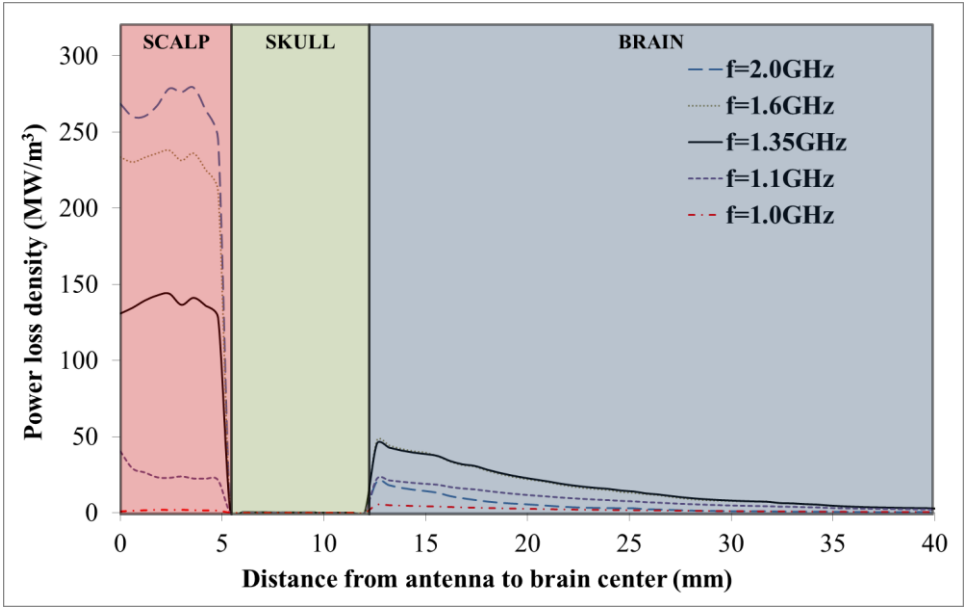

Figure 3.11 – Profile of the calculated power loss density pattern *vs.* distance from antenna to brain center of a 2.5 cm diameter log-spiral antenna coupled to the virtual human head phantom. The antenna has different sensing volumes at each frequency, with deepest penetration in the [1.1, 1.6] GHz range.

Figure 3.12 presents the absolute power collected from different structures over frequency. One can observe that the antenna receives energy mainly from scalp and brain over the computed frequency range [0.5, 3.0] GHz. The remaining energy is collected from skull (<0.3 %), mylar and plexiglass used to support the head phantom (<1.5 %) and the antenna materials including the substrate and coverlay (<2.3 %).

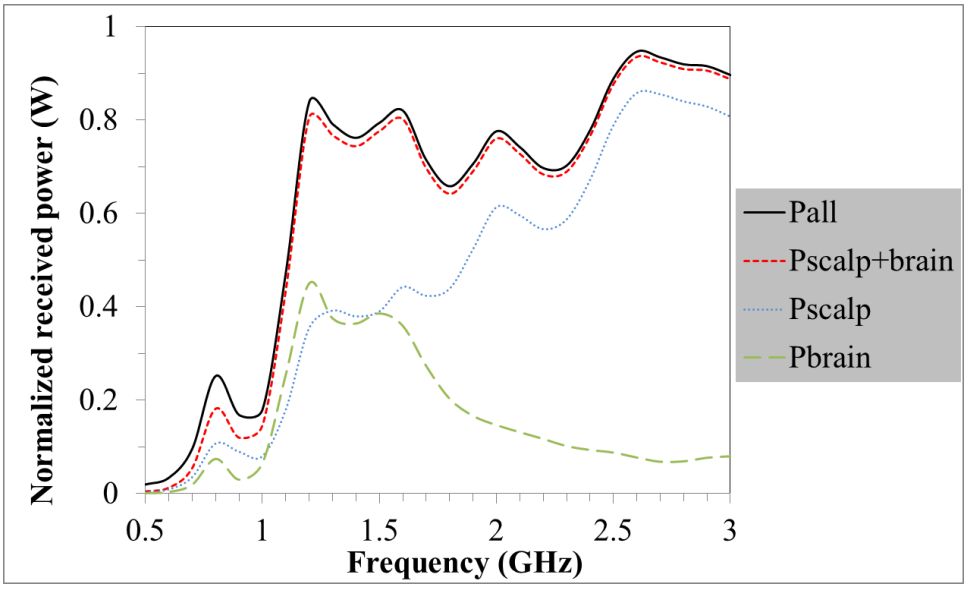

Figure 3.12 – Normalized received power (W) *vs.* frequency from brain (Pbrain), scalp (Pscalp), sum of power from scalp and brain (Pscalp+brain) and from all computational objects composed of air, scalp, skull, brain and structural plastics (Pall).

3.3.3. Simulated electric field

Figure 3.13 presents the square of modulus of $\boldsymbol{E}_0$ ($|\boldsymbol{E}_0|^2$) which provides the regions where the 2.5 cm antenna collects radiation. The antenna is particularly sensitive in the air regions (above and below) surrounding the antenna cup. This shows where the receive antenna can collect external EMI that is responsible for deteriorating the radiometric output signal. Figure 3.13 also reinforces the sensitivity of the antenna in deep brain regions where we can also observe the electric field wave behavior and its attenuation.

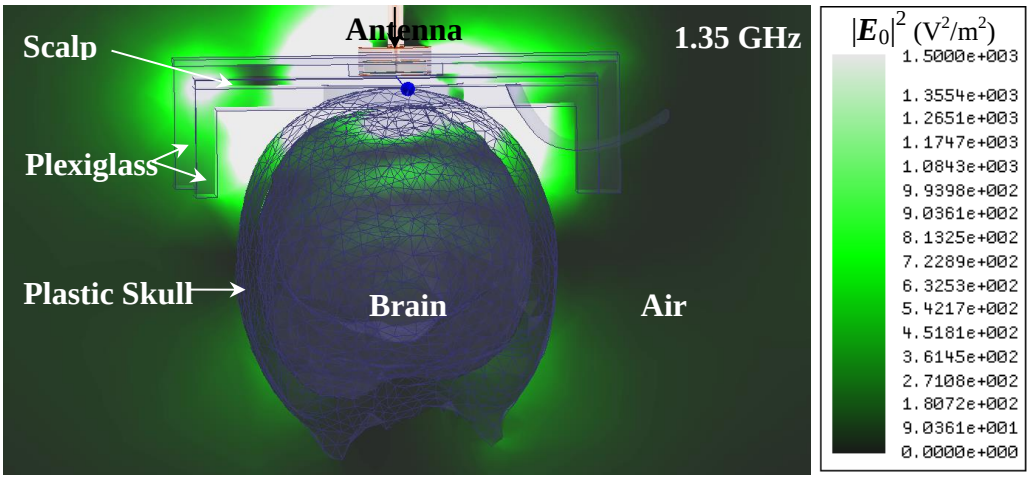

Figure 3.13 – Square of modulus of $\boldsymbol{E}_0$ ($|\boldsymbol{E}_0|^2$) over a sectional cut of the computational domain at 1.35 GHz for the 2.5 cm planar log-spiral antenna.

3.3.4. Antenna implementation and phantom results

Based on the simulation results, the 2.5 cm diameter log-spiral antenna is encapsulated together with the miniature front stage of the radiometer inside a cylindrical copper tube with 1 mm wall thickness (Figure 3.14). The conducting arm of the microstrip log-spiral antenna is constructed on a 0.25 mm thickness of a ceramic material (RO3003, Rogers Corp., USA) with 35 μm thickness rolled copper. This structure is glued to a hydrocarbon ceramic substrate (RO3010, Rogers Corp., USA) with 4.45 mm thickness and $\varepsilon_{r,substrate}$ = 10.2 and $\sigma_{substrate}$ = 1.68×10^{-3} S/m. The coverlay consists of an ultra-low loss dielectric matching disk of 1 mm thickness (Eccostock® HiK500F, Emmerson& Cumming, Randolph, MA, USA) with $\varepsilon_{r,coverlay}$ = 30 and $\sigma_{coverlay}$ = 4.50×10^{-3} S/m.

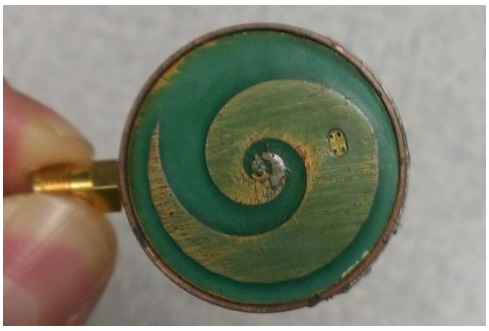

Figure 3.14 – The 2.5 cm log-spiral antenna encapsulated together with radiometer printed circuit inside a cylindrical copper tube with 1 mm wall thickness.

Figure 3.15 presents the radiometer response to serial 10 °C changes in brain phantom temperature (37 °C, 27 °C, 37 °C) while holding the superficial scalp region constant at 32 °C. The constant temperature scalp guarantees that the radiometric signal variation is independent from the power collected in the scalp region. The radiometric signal from brain (black curve) includes a 74 second delay caused by the 200-point median calculation applied in real time to the raw data giving by the radiometer. Although scalp temperature is maintained constant over the entire experiment, the radiometric sensor is able to track changes of brain phantom inside the skull within $\pm$0.4 °C and during the 4.6-hour experiment. The radiometric equivalent temperature follows correctly the brain phantom temperature as it is reduced by 10 °C for one hour and as it is returned back to its initial temperature (as would be done during a cardiac surgery).

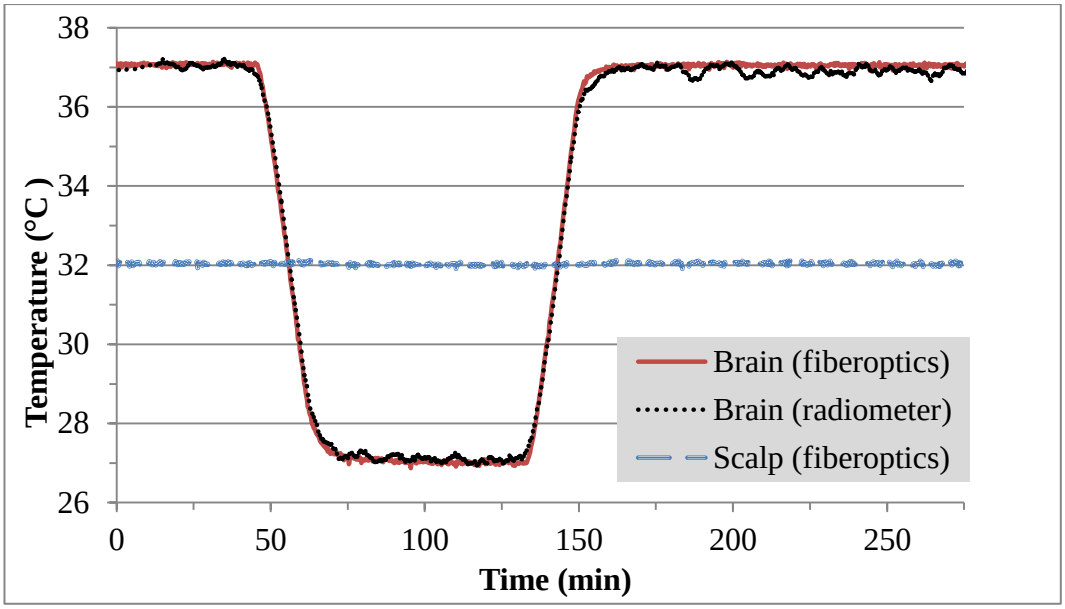

Figure 3.15 – Effective brain temperature derived from total power measurements of the non-invasive radiometric sensor (black curve) closely mirrors the actual temperature of the circulating brain phantom (red curve). Blue curve shows the measured scalp temperature, with no significant drift error during the 4.6 hour period of monitoring.

The accuracy and stability of the radiometric signal during a 4.6-hour experiment is shown in Figure 3.16. This figure presents the difference between the temperature measured by the radiometer and fiber optic probe. The maximum difference between these temperatures during the entire experiment is 0.4 °C. Table 3.8 shows a more detailed analysis of this error including some relevant statistical parameters for each segment of the experiment. The temperature error during cooling (0.38 °C) and rewarming (0.36 °C) is higher than the error obtained during the three steady state periods (0.21 °C, 0.24 °C and 0.27 °C).

Table 3.8 – Statistical analysis of the difference between radiometer and fiber optic measured brain temperatures over each segment of study: minimum (Min), maximum (Max), amplitude (Amp), average (Ave) and standard deviation (SD).

Segment	**Time (min)**	**Min (°C)**	**Max (°C)**	**Amp (°C)**	**Ave (°C)**	**SD (°C)**
Constant at 37°C	[0, 44]	-0.22	0.21	0.21	0.02	0.08
Cooling	[44, 72]	-0.38	0.32	0.35	-0.07	0.15
Constant at 27°C	[72, 129]	-0.35	0.14	0.24	-0.07	0.08
Rewarming	[129, 160]	-0.36	0.36	0.36	0.05	0.18
Constant at 37°C	[160, 275]	-0.12	0.43	0.28	0.13	0.11
Full experiment	[0, 275]	-0.38	0.43	0.40	0.04	0.14

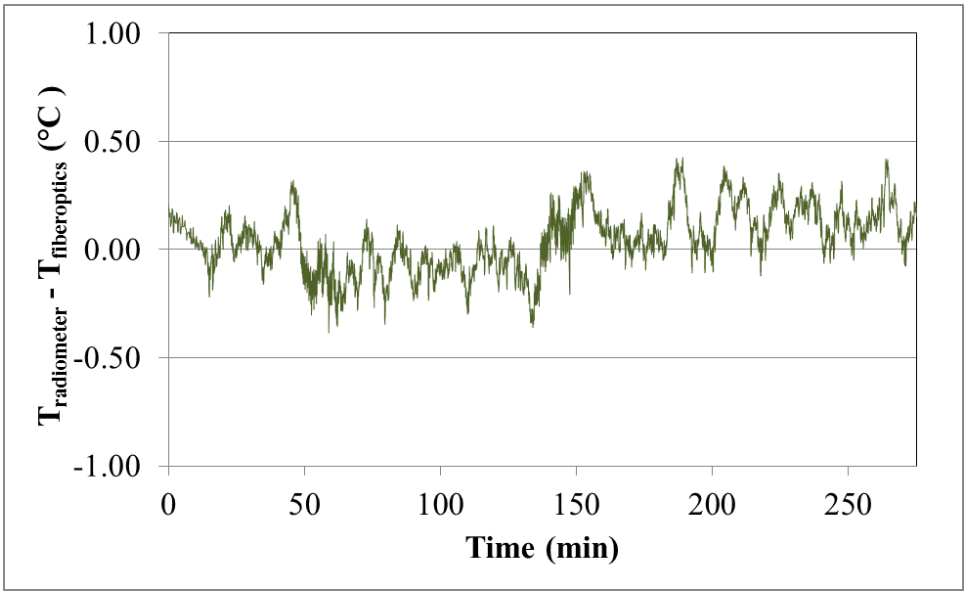

Figure 3.16 –Temperature difference between the equivalent radiometric brain temperature and the temperature measured with the fiber optic probe in the brain phantom.

3.3.5. Human experimental results

The S_{11} results for three different locations in a human head subject (male, age 42 and body mass index BMI = 30 kg/m^2) are presented in Figure 3.17 for the manufactured receive antenna. In general, S_{11} results are significantly better when the antenna is in contact with human skin than with the developed human phantom. These S_{11} results have similar profiles to the ones simulated in the phantom occipital region with two significant differences: there is a frequency shift to the right and S_{11} values are overall 5 dB lower. This latter result is an indication that, although the band is shifted from the optimized band [1.1, 1.6] GHz to [1.25, 1.7] GHz (blue region), the match impedance is improved.

Figure 3.18 shows the radiometric effective brain temperature (T_{brain}) of a one-year-old male patient along with measured rectal (T_{rectum}) and nasopharyngeal (T_{naso}) temperatures during a 2-hour surgery. The brain temperature measured by the radiometer (solid black curve) results from a 400-point median which corresponds to 5 minutes of raw data. Rectal and nasopharyngeal temperature measurements are shown for comparison and recorded every 15 minutes. Within this uncertainty, a close correlation of falling and rising temperatures is seen between all core temperature measurements. While the radiometric brain temperature remains [1, 2] °C higher than other core temperatures throughout the 2-hour surgery, the nasopharyngeal and rectal

measures exhibit a time delay in returning back to normothermia. This time delay produces a higher temperature differential between brain and rectal or nasopharyngeal temperature during patient rewarming. The difference in core temperature measurements $T_{brain} - T_{rectum}$ ranges from 0 °C to 3.9 °C, around 55 min and 80 min surgery, respectively. Similarly, the difference $T_{brain} - T_{naso}$ ranges from 1 °C to 4.9 °C at the beginning of surgery and at the time of peak temperature in brain following reheating of the patient, respectively.

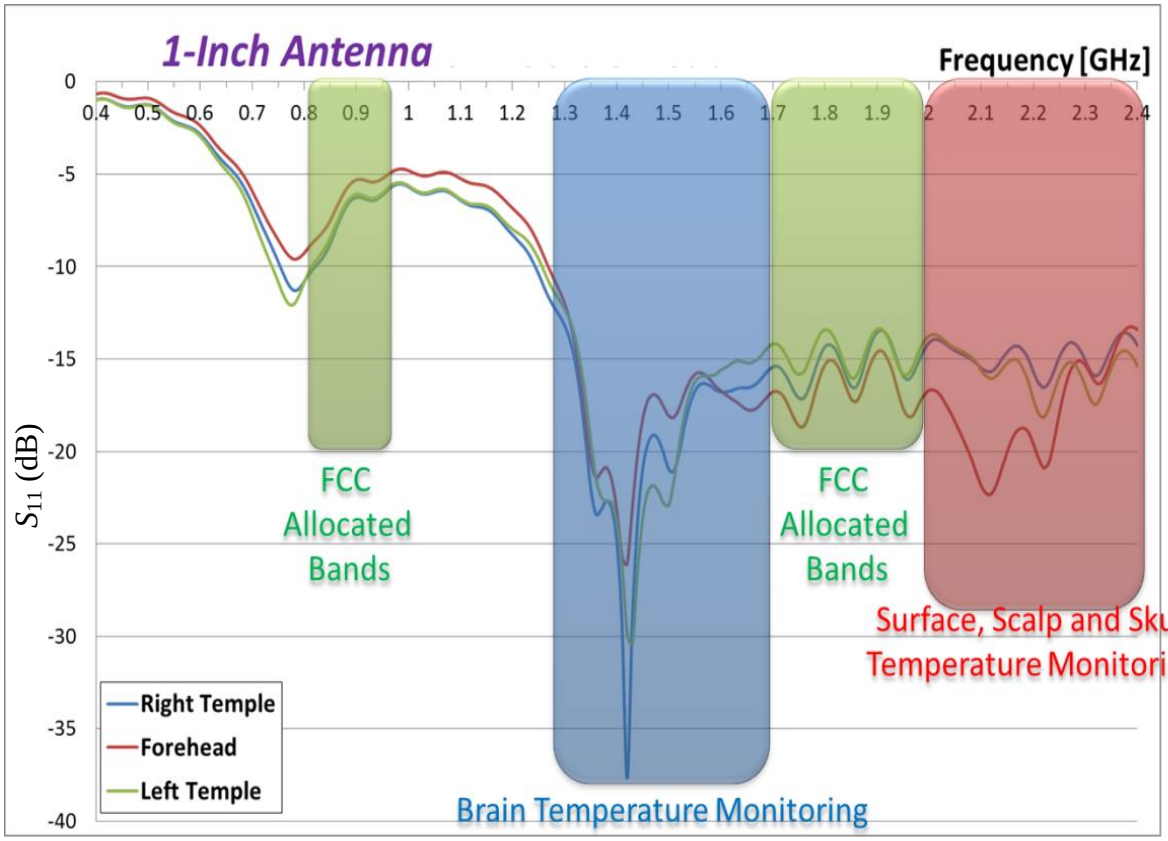

Figure 3.17 – Antenna mismatch of the manufactured receive antenna in three different locations (right temple, forehead and left temple) in a human head subject (male, age 42 and BMI=30 kg/m^2).

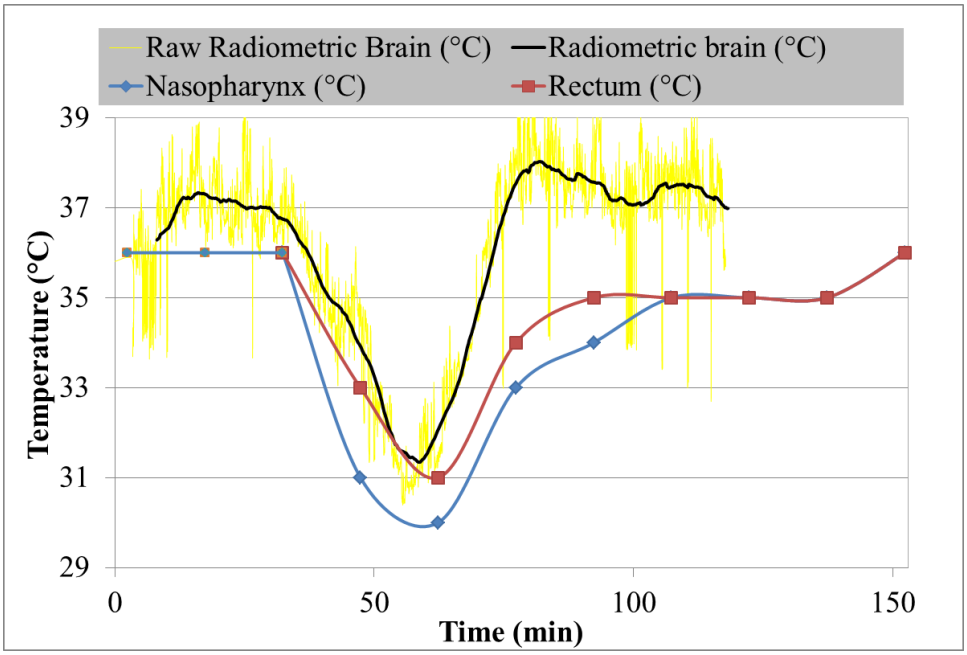

Figure 3.18 – Equivalent brain temperature (black curve) from 400-point median calculations of raw radiometric readings (yellow curve) during surgery of pediatric patient, correlated with manually recorded rectal (red points) and nasopharyngeal (blue points) core temperature measurements.

3.4. Discussion

There is strong clinical evidence that measuring core body temperature has significant benefit to the patient in terms of speed of recovery and reduction of potential post-surgical complications. Moreover, core temperature should return quickly to the normothermic range after surgery. Currently, core temperature measurement is of most benefit in the patient recovery from hypothermic events such as cardiac surgery with bypass perfusion, resuscitation of near drowning victims or other severe hypothermia exposure. During these acute situations, the ability to provide rapid and accurate feedback of critically important core temperature, as the one determined from the most vital tissue (brain), would be invaluable to treating physicians.

To achieve such goal, a new computational model is established to simulate power collected from a human head phantom and received by an ultra-wideband antenna located at the tissue surface. The model is based on Planck's principle that thermal energy radiates from living tissue with a measurable amount of power in the microwave frequency band. This thermal radiation can be collected with a microwave receive antenna, amplified, filtered and quantified with a sensitive power detector. With

appropriate electronics and software processing, the received power can be correlated directly with temperature of tissue located within the radiation field of the antenna. The design and optimization of a 2.5 cm diameter radiometric antenna based on tapered log-spiral geometry is the main subject of this study.

The parametric analysis presented in Figure 3.6, and complemented in Table 3.6, provides the basis for determining the optimum frequency band of operation while attempting to avoid sensitivity to external EMI at the noisiest frequencies near 0.85, 1.85 and 2.45 GHz. The best compromise between good match impedance ($S_{11} \leq$ -10 dB) and avoiding regions with high EMI is found in the range [1.1, 1.6] GHz, and is obtained for N = 2, $\delta_{coverlay}$ = 1 mm, $\varepsilon_{r,coverlay}$ = 30 and $\varepsilon_{r,substrate}$ = 10.2 (RO3010). This particular arrangement allows a theoretical bandwidth Δf = 530 MHz that fits the standard for ultra-wideband (UWB) designation [45]. This band presents an average antenna efficiency of 50.3% meaning that half of the power collected by the microwave antenna is derived from the target brain region.

Self-complementary structures have frequency-independent input impedance [55] which improves S_{11} and consequently increases the bandwidth. As previously discussed, 1.8 log-spiral turns would result in a self-complementary tapered log-spiral antenna within the constrained ρ_{ext}, ρ_0 and ρ_1. Although the manufactured feed point does not allow a perfect self-complementary structure, the optimized 2 log-spiral turns (RO3010) is still close to the theoretical estimation. Thus, the self-complementary principle is a valid approach for the log-spiral design.

In Figure 3.7a the lower cut-off frequency f_L is constant at 0.98 GHz and independent on the number of log-spiral turns. From equation (4) we deduce f_L = 1.20 GHz replacing $\varepsilon_{r,eff}$ by $\varepsilon_{r,substrate}$ = 10.2. This result indicates that the substrate dictates the wavelength attenuation of the electromagnetic waves that are detected by the spiral antenna. This is expected since the substrate is on direct contact with the spiral metal trace and it is the thicker element on the multilayered antenna environment. Also, Figure 3.8a shows that decreasing $\varepsilon_{r,substrate}$ from 10.2 to 6.15 and 3, leads to an increase of f_L from 0.98 to 1.05 and 1.09 GHz, respectively; this behavior agrees with the one from equation (4) and the relation $\varepsilon_{r,eff} \sim \varepsilon_{r,substrate}$. Using the same equation (4) one can estimate the detectable wavelengths by the spiral antenna to be in the interval [48.1, 70.0] mm along the band [1.1, 1.6] GHz. These values are higher but of the same order than the spiral length 41.2

mm (N = 2), where the spiral length is determined from equation (3). The radiation patterns on Figure 3.10 (x-z and y-z planes) for the lower (1.1 GHz) and upper (1.6 GHz) frequencies of the operating band show a slightly more focused radiation pattern in the y-z plane which indicates an elliptical polarization. This nonlinear polarization is more adequate than linear polarization for MW radiometry, as discussed previously.

The use of a matching layer (coverlay) is introduced into the design to improve the electromagnetic coupling between the load and antenna. By adding the coverlay, both the matching impedance and antenna efficiency are improved (Figure 3.9 and Table 3.7). Best results for S_{11} are achieved for $\delta_{coverlay}$ = 1 mm, while efficiency does not vary significantly for $\delta_{coverlay}$ in [1, 5] mm (Table 3.7). Thus, in order to manufacture the antenna we choose $\delta_{coverlay}$ = 1 mm since it presents the widest bandwidth. It is interesting to note, however, that changing the coverlay permittivity within the range [5, 40] does not change either the impedance match or antenna efficiency. We suspect that this is related to the small coverlay thickness (1 mm) compared to any of the wavelengths in the analyzed range [48.1, 70.0] mm. Therefore, we chose a readily available ultra-low loss dielectric matching disk with 1 mm thickness (Eccostock® HiK500F, Emmerson& Cumming, Randolph, MA, USA) with $\varepsilon_{r,coverlay}$ = 30 and $\sigma_{coverlay}$ = 4.50×10^{-3} S/m.

Antenna efficiency results (Figures 3.7b, 3.8b and 3.9b) do not vary dramatically within the range of parametric analysis used (Table 3.2). In fact, the efficiency is higher than 40% across the band [1.1, 1.6] GHz for all simulations, with the exception of the zero thickness matching layer (Figure 3.9b). These results prove that the log-spiral antenna design fits our specific problem (brain monitoring) and is indeed focused towards brain, as intended, collecting energy even in regions located at several centimeters depth as seen in Figures 3.10 and 3.11. From these analyses, one can observe a trade-off between the high power collection from scalp region at higher frequencies and low received power at lower frequencies as the antenna frequency approaches the lower cut-off frequency. This trade-off is clearly visible in Figure 3.12 where the normalized received power is plotted for different structures. The power collected from brain is higher in the optimized band [1.1, 1.6] GHz which justifies the better efficiency results at this particular band. These results also explain why so many attempts to use microwave radiometry for long term monitoring of brain temperature have proven to be inadequate

[22, 28, 56-59]. These radiometers operated at higher frequencies (>2.5 GHz) which did not allow an efficient power collection from brain, as shown in our simulations.

Knowledge of the electric field within the surrounding environment of the load allows to predict which regions are more susceptible to collect parasitic signals (FCC allocated bands). In Figure 3.13, we can observe that the antenna becomes sensitive in the air regions between the plexiglass structure and the plastic skull as well as above the antenna. Air electrical conductivity is of the order 10^{-15} S/m and when multiplied by $|\boldsymbol{E}_0|^2$ to obtain power loss density P_d (equation (10)) the result is of the order 10^{-12} W/m^3. Thus, power collected from air is negligible, unless there are parasitic signals from environmental EMI noise. In order to reduce the influence of EMI during experiments we use an EMI shielding cloth that attenuates parasitic signals by 30 dB. Figure 3.13 also reinforces the sensitivity of the antenna in deep brain regions where the wave behavior and wave attenuation of the electric field are clear.

The *a priori* understanding of relative amounts of energy from each domain, as provided by the simulations in this work, allows the development of a calibration algorithm that converts total power received by the antenna (P_{ant}) into temperature (T_B) using $P_{ant} = Gk_BT_B\Delta f$ (equation (7)). The averaged brain temperature (T_{brain}) can then be extracted from T_B using an algorithm similar to those described in [29, 53] and recently improved for this application by Maccarini *et al.* [36].

A complete [1.1, 1.6] GHz radiometer sensor is built accordingly to the optimized parameters (Figure 3.14). The lightweight entire sensor package has a low profile 2.8 cm diameter by 1.5 cm high. This sensor can be held over the head's skin with an EMI shielding adhesive patch and/or elastic strap. The sensor is further tested in a realistic head phantom experiment that simulates brain temperature variations during surgery during 4.6 hours. The maximum difference between the measured temperature (fiber optic) and the equivalent radiometric brain temperature is 0.38 °C during the rapid temperature changes when cooling (-0.35 °C/min) and rewarming (0.32 °C/min) the brain phantom. This occurs due to the 74 s delay in measurements due to the moving median calculations. However, the temperature rates of patients undergoing surgery are at least 10 times slower than the cooling/rewarming rates implemented in our study [60]. Thus, the transient temperature errors during rapid cooling and rewarming periods do not appear relevant. In fact these temperature errors should be much less than the ones

associated with typical time delays of reading core temperature from remote sites like esophagus and rectum.

The 0.4 °C experimental error fits the current clinical need of <0.5 °C that is the smallest difference that has been associated with hypothermia-induced complications [8, 16]. During the periods where temperature is constant (Figure 3.15), the calculated radiometric temperature has a small cyclic variation of 0.27 °C. The repetitive nature of these variations suggests that they may be the result of the peristaltic pump-induced convection currents within the balloon, and thus correspond to actual small temperature variations in the brain phantom rather than external EMI. It is important to note that the scalp is maintained constant at 32 °C so we can demonstrate clearly that the radiometric power variation is only due to the intracranial temperature variation. The data also demonstrate our ability to track temperature changes of brain (core temperature) during long time periods, such as open heart bypass surgery, enabling the physician to carefully monitor the patient's temperature to return to normothermic temperature quickly at the end of a long procedure.

This experimental model of the human head accounts for the major physiological and anatomical parameters but has some limitations. Phantoms never reproduce the actual clinical situation precisely. Brain, in particular, is a complex organ with spatial and temporal temperature variations that cannot be predicted and may degrade the accuracy of clinical measurements. The intracranial sensing region of the optimized microwave antenna is high (50.3 %) and the average temperature of this region should approximate true core temperature. The simulated results are valid only for the occipital region. However, placing the antenna in the temporal or frontal areas would require a new study. In any case, this phantom serves its dual purpose to validate the computational method employed to manufacture the microwave antenna and to test the radiometric system linked to the antenna.

Although the receive antenna was optimized for a human phantom head, we decide to to test its performance in humans. Figure 3.17 measured S_{11} with the manufactured antenna in the temple and forehead region of an adult human. Along frequency, we observe that S_{11} curves have less oscillations in the phantom head (Figure 3.9a) than in the human head (Figure 3.17), due to the higher multilayered environment in the latter. Note that the human skin-to-brain region is composed by: epidermis, scalp (skin, connective tissue, galea aponeurotica layer, loose areolar connective tissue layer and pericranium),

skull (outer middle and inner table layers), meninges (dura matter, arachnoid matter and pia matter), cerebrospinal fluid and brain parenchyma (white and grey matter) [61]. The good S_{11} values over a wideband [1.25, 2.40] GHz also open the possibility for thermal profiling. The band [1.25, 1.70] GHz (blue region in Figure 3.17) allows to acquire brain temperature while the band [2.0, 2.4] GHz (red region in Figure 3.17) can be used to extract scalp averaged temperature. Note that these are widebands ($\geq$400 MHz) and avoid parasitic signals (green regions in Figure 3.17). If we add a thermistor to the antenna, we can also measure skin temperature and these three distinguishable regions allow to create a thermal profile from outer skin to inner core brain.

As an initial step to introduce this technology into clinical usage, this work reports the first clinical case of monitoring deep brain temperature during a 2-hour pediatric surgery (Figure 3.18). Although no gold standard measurement of brain temperature is available, a good correlation is seen between falling and rising temperatures inside the brain with the ones measured in rectum and nasopharynx. During the 2-hour surgery the calculated radiometric brain temperature remains at least [1, 2] °C higher than the other core temperature surrogates (rectum and nasopharynx); reaching a difference up to 4.9 °C in the cooling/rewarming regions. One of the reasons for these differences is the contribution of the surgical lightheads that are closer to the radiometer than the ones used with the phantom in the test room. We use a network analyzer (E5071C, Agilent Technologies) to compare the environmental thermal noise in the surgical room and in the test room (data not recorded). We confirm that the higher EMI contribution is derived from surgical lightheads. The second contribution for the experimental error is the time delay exhibited by the temperature core surrogates when returning back to normothermia: this explains the higher temperature difference during patient rewarming (up to 4.9 °C). The time delays observed in Figure 3.18 are not feasible to validate the radiometric device. A true brain core surrogate is required by using an invasive thermistor in a convenient artery – dependent on the surgery – during open brain surgeries.

A new computational model is under development (Figure 3.19). The base is an accurate CAD anatomical human head geometry with frequency-dependent electrical properties assigned to each specific tissue region. The optimization method will be reassessed in the occipital, temporal and frontal regions. These optimization studies will determine the best region in terms of match impedance and efficiency. Figure 3.17

already shows that the S_{11} results in humans are similar to those in the human phantom. However, efficiency in the human head should be different due to the irregular anatomy in the skull, variable scalp thickness and different electrical properties (Figure 3.4). The manufactured antenna may require a redesign to be used in clinic. However, the antenna developed in this work proved to measure the temperature successfully in the target (brain phantom). A full clinical investigation will confirm the utility of this new 2.5 cm log-spiral antenna coupled with the radiometric sensor to measure the core brain temperature of surgical patients.

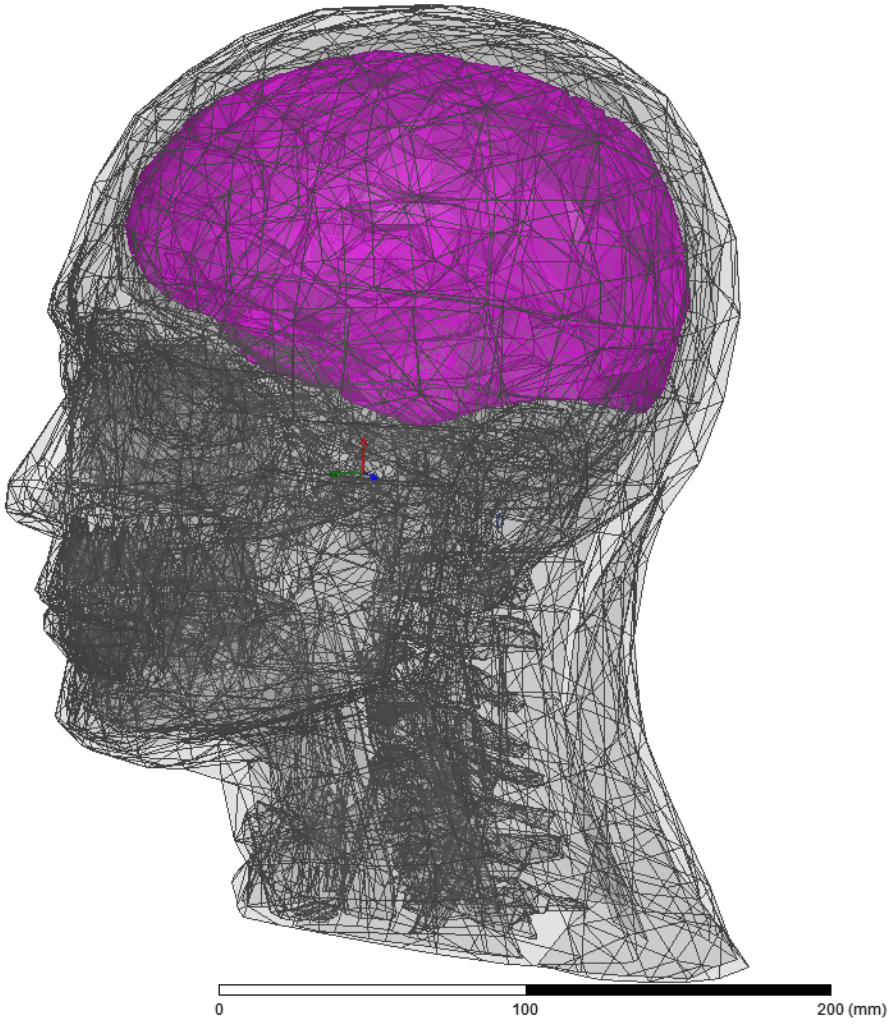

Figure 3.19 – Human head CAD model with brain highlighted in magenta.

3.5. Conclusions

A microwave radiometric sensor is developed for rapid non-invasive feedback of critically important brain temperature. The key element of the sensor is a tapered 2.5 cm log-spiral antenna. Its design and operating frequency band are optimized based on: maximization of the power ratio received by the radiometric antenna from the target (brain); maximization of the bandwidth and impedance match ($S_{11}\leq$-10 dB); and avoid noisy wireless communications frequencies. The parametric analysis over the desired frequency band presents a complex behavior, which is elucidated with the physics of microwave signals. The optimized antenna design with N = 2, $\delta_{coverlay}$ = 1 mm, $\varepsilon_{r,coverlay}$ = 30 and $\varepsilon_{r,substrate}$ = 10.2 (RO3010) has an average antenna efficiency of 50.3 % in the desired [1.1, 1.6] GHz band. This particular arrangement allows a theoretical bandwidth Δf = 530 MHz that fits the standard for ultra-wideband (UWB) designation. The simulations demonstrate the different received energy contributions from scalp, skull and brain tissues, which pave the way for temperature profiling in the human head including core temperature (brain). The materials chosen allow to manufacture a 2.5 cm log-spiral antenna embedded in a 2.8 cm low-cost radiometric sensor with sufficiently small size to be conformal with the human head during surgery. The sensor is tested on a full scale multilayer tissue phantom of the human head. During a 4.6-hour experiment, the maximum error associated with the calculated radiometric brain temperature is 0.4 °C which fits the current clinical need of <0.5 °C. The usage of a specific-target computational model (physical phantom) coupled with the antenna model proves to be useful to optimize the antenna design for brain temperature monitoring. We anticipate that this newly developed sensor can help reducing surgical complications, thereby reducing overall costs and improving clinical outcomes for patients in recovery from post-surgical hypothermia.

Acknowledgements

The authors would like to acknowledge support from NIH R21-DK092912 and Thermimage Corp. Special gratitude to ANSYS and COMSOL for the continuous software support. Dário Barros Rodrigues acknowledges the Portuguese Foundation for Science and Technology (FCT-MEC) for a post-graduate scholarship SFRH/BD/73215/2010 and together with Pedro Pereira and Paulo Limão-Vieira the grant PEst-OE/FIS/UI0068/2011.

Appendix 3 – Radiometer Setup Protocol

Materials:

1) Laptop (PC)
2) Radiometer Cup
3) 2nd module radiometer (Accutemp module)
4) Power supply (12V)
5) Cables
    a) HDMI cable
    b) USB cables (2)
    c) SMA cable
    d) BNC cable (12V)

Procedure:

1. Register the time of anesthesia (format hh:mm:ss).
2. Connect the cables (see Figure below):
    a. Left side USB connector of the PC ↔ **USB cable** ↔ Back of Accutemp module: label "Power" (Power Sensor)
    b. Right side USB connector of the PC ↔ **USB cable** ↔ Lateral side of Accutemp module: label "ADC" (measuring computing)
    c. Radiometer cup ↔ **SMA cable (blue)** ↔ Front side of Accutemp module
    d. Radiometer cup ↔ **HDMI cable** ↔ Front side of Accutemp module
    e. Power Supply ↔ **BNC cable** ↔ Lateral side of Accutemp module: label "12V"

2) Place the radiometer in the patient and secure it with a band. Register the time of placement (format hh:mm:ss).
3) Turn on the computer.
4) Double click on *ClinicalRadiometer.vi*
5) Press run

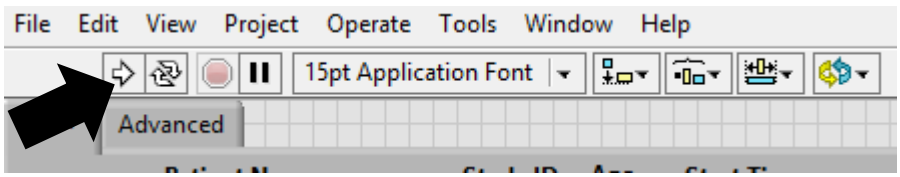

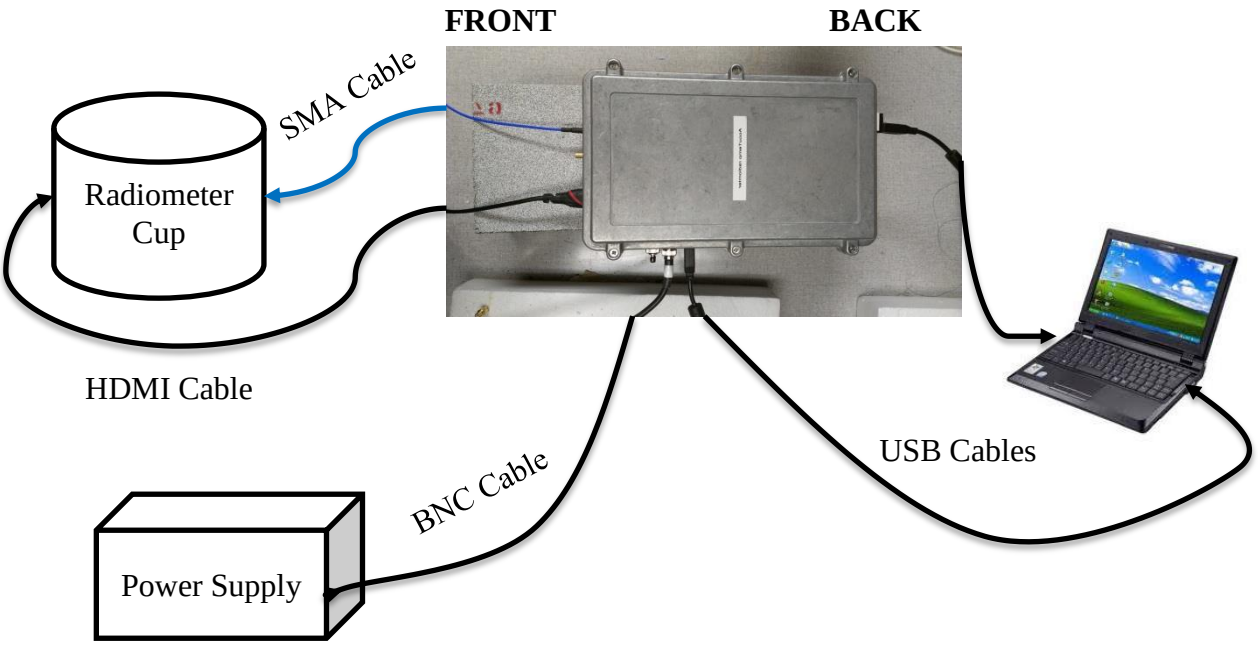

3. Type or choose from options:
    a. Name of the patient
    b. Medical Record
    c. Type of surgery
    d. Study ID
    e. Trial Site
    f. Age
    g. Sex
    h. Sensor location
    i. Weight
    j. Height
    k. Units
4. Press **Begin**.
5. Allow the skin temperature to stabilize. A message will pop up “The radiometer is now ready for calibration”. Press **OK**.
6. **Type the core temperature** from the intracavitary thermometer reference. Press **Calibrate**.

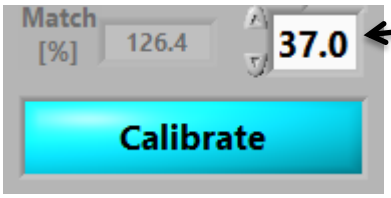

Type core temperature here.

7. When surgery is finished press **STOP MEAS**.

8. Turn off computer and unplug all cables.
9. Attach data from intracavitary thermometer reference.

References

1. Polderman KH: Mechanisms of action, physiological effects, and complications of hypothermia. Critical Care Medicine 2009, 37(7):S186-S202.

2. Hannenberg AA, Sessler DI: Improving Perioperative Temperature Management. Anesthesia and Analgesia 2008, 107(5).

3. Diaz M, Becker DE: Thermoregulation: physiological and clinical considerations during sedation and general anesthesia. Anesthesia progress 2010, 57(1):25-32; quiz 33-24.

4. Castaneda AR, Jonas RA, Mayer JE, Hanley FL: Cardiac Surgery of the Neonate and Infant. In. Edited by Castaneda AR, 1st edn. University of Michigan; 1994.

5. Frank SM, Fleisher LA, Breslow MJ, Higgins MS, Olson KF, Kelly S, Beattie C: Perioperative maintenance of normothermia reduces the incidence of morbid cardiac events - A randomized clinical trial. Jama-Journal of the American Medical Association 1997, 277(14).

6. Kurz A, Sessler DI, Lenhardt R: Perioperative normothermia to reduce the incidence of surgical-wound infection and shorten hospitalization. New England Journal of Medicine 1996, 334(19).

7. Schmied H, Kurz A, Sessler DI, Kozek S, Reiter A: Mild hypothermia increases blood loss and transfusion requirements during total hip arthroplasty. Lancet 1996, 347(8997).

8. Winkler M, Akca O, Birkenberg B, Hetz H, Scheck T, Arkilic CF, Kabon B, Marker E, Grubl A, Czepan R et al: Aggressive warming reduces blood loss during hip arthroplasty. Anesthesia and Analgesia 2000, 91(4):978-984.

9. Rajagopalan S, Mascha E, Na J, Sessler DI: The effects of mild perioperative hypothermia on blood loss and transfusion requirement. Anesthesiology 2008, 108(1).

10. Lenhardt R, Marker E, Goll V, Tschernich H, Kurz A, Sessler DI, Narzt E, Lackner F: Mild intraoperative hypothermia prolongs postanesthetic recovery. Anesthesiology 1997, 87(6).

11. Lawson L, Bridges EJ, Ballou I, Eraker R, Greco S, Shively J, Sochulak V: Accuracy and precision of noninvasive temperature measurement in adult intensive care patients. American Journal of Critical Care 2007, 16(5).

12. Pompei F, Pompei M: Non-invasive temporal artery thermometry: Physics, physiology, and clinical accuracy. In: Conference on Thermosense XXVI: Apr 13-15 2004; Orlando, FL. Spie-Int Soc Optical Engineering: 61-67.

13. Moran JL, Peter JV, Solomon PJ, Grealy B, Smith T, Ashforth W, Wake M, Peake SL, Peisach AR: Tympanic temperature measurements: Are they reliable in the critically ill? A clinical study of measures of agreement. Critical Care Medicine 2007, 35(1).

14. O'Grady NP, Kalil A, Barie P, Bleck T: Misguided guidelines on noninvasive thermometry The authors reply. Critical Care Medicine 2009, 37(1).

15. Haugk M, Stratil P, Sterz F, Krizanac D, Testori C, Uray T, Koller J, Behringer W, Holzer M, Herkner H: Temperature monitored on the cuff surface of an endotracheal tube reflects body temperature. Critical Care Medicine 2010, 38(7).

16. Sessler DI: Temperature monitoring and perioperative thermoregulation. Anesthesiology 2008, 109(2):318-338.

17. McIlvoy L: Comparison of brain temperature to core temperature: a review of the literature. The Journal of neuroscience nursing : journal of the American Association of Neuroscience Nurses 2004, 36(1).

18. Arunachalam K, Stauffer PR, Maccarini PF, Jacobsen S, Sterzer F: Characterization of a digital microwave radiometry system for noninvasive thermometry using a temperature-controlled homogeneous test load. Physics in Medicine & Biology 2008, 53(14):3883-3901.

19. Klemetsen O, Birkelund Y, Maccarini PF, Stauffer P, Jacobsen SK, Electromagnet A: Design of Small-sized and Low-cost Front End to Medical Microwave Radiometer. Piers 2010 Cambridge: Progress in Electromagnetics Research Symposium Proceedings, Vols 1 and 2 2010:932-936.

20. Klemetsen O, Birkelund Y, Jacobsen SK, Maccarini PF, Stauffer PR: Design of Medical Radiometer Front-End for Improved Performance. Prog Electromagn Res B Pier B 2011, 27:289-306.

21. Hand JW: Physical techniques for delivering microwave energy to tissues. The British journal of cancer Supplement 1982, 5:9-15.

22. Bardati F, Iudicello S: Modeling the visibility of breast malignancy by a microwave radiometer. IEEE Trans Biomed Eng 2008, 55(1):214-221.

23. Camart JC, Despretz D, Prevost B, Sozanski JP, Chive M, Pribetich J: New 434 MHz interstitial hyperthermia system monitored by microwave radiometry: theoretical and experimental results. International Journal of Hyperthermia 2000, 16(2):95-111.

24. Dubois L, Sozanski JP, Tessier V, Camart JC, Fabre JJ, Pribetich J, Chive M: Temperature control and thermal dosimetry by microwave radiometry in hyperthermia. IEEE Trans Microw Theory Tech (USA) 1996, 44(10, pt.2):1755-1761.

25. Jacobsen S, Stauffer PR: Can we settle with single-band radiometric temperature monitoring during hyperthermia treatment of chestwall recurrence of breast cancer using a dual-mode transceiving applicator? Phys Med Biol 2007, 52(4):911-928.

26. Stauffer PR, Jacobsen S, Neuman D: Microwave array applicator for radiometry controlled superficial hyperthermia. In: Thermal Treatment of Tissue: Energy Delivery and Assessment. Edited by Ryan TP, vol. 4247. San Jose: Proceedings of SPIE; 2001: 19-29.

27. Wang SS, VanderBrink BA, Regan J, Carr K, Link MS, Homoud MK, Foote CM, Estes NA, 3rd, Wang PJ: Microwave radiometric thermometry and its potential applicability to ablative therapy. J Interv Card Electrophysiol 2000, 4(1):295-300.

28. Hand JW, Van Leeuwen GMJ, Mizushina S, Van De Kamer JB, Maruyama K, Sugiura T, Azzopardi DV, Edwards AD: Monitoring of deep brain temperature in infants using multi-frequency microwave radiometry and thermal modelling. Physics in Medicine and Biology 2001, 46(7):1885-1903.

29. Maruyma K, Mizushina S, Sugiura T, Van Leeuwen GMJ, Hand JW, Marrocco G, Bardati F, Edwards AD, Azzopardi D, Land D: Feasibility of noninvasive measurement of deep brain temperature in newborn infants by multifrequency microwave radiometry. IEEE Trans Microw Theory Tech (USA) 2000, 48(11, pt.2):2141-2147.

30. Oikonomou A, Karanasiou IS, Uzunoglu NK: Phased-array near field radiometry for brain intracranial applications. Progress in Electromagnetics Research-Pier 2010, 109:345-360.

31. Arunachalam K, Maccarini P, De Luca V, Bardati F, Snow B, Stauffer P: Modeling the detectability of vesicoureteral reflux using microwave radiometry. Phys Med Biol 2010, 55(18):5417-5435.

32. Snow BW, Arunachalam K, De Luca V, Maccarini PF, Klemetsen O, Birkelund Y, Pysher TJ, Stauffer PR: Non-invasive vesicoureteral reflux detection: Heating risk studies for a new device. Journal of Pediatric Urology 2011, 7(6).

33. Stauffer P, Maccarini P, Arunachalam K, Salahi S, De Luca V, Boico A, Klemetsen O, Birkelund Y, Jacobsen S, Bardati F et al: Microwave Radiometry for Non-Invasive Detection of Vesicoureteral Reflux (VUR) Following Bladder Warming In: Proc of SPIE: Edited by Ryan T. SPIE Press, Bellingham WA 2011 PMCID:3409575: 7901OV-7901-7911.

34. Arunachalam K, Maccarini P, De Luca V, Tognolatti P, Bardati F, Snow B, Stauffer P: Detection of vesicoureteral reflux using microwave radiometry-system characterization with tissue phantoms. IEEE Trans Biomed Eng 2011, 58(6):1629-1636.

35. Rodrigues DB, Maccarini PF, Salahi S, Colebeck E, Topsakal E, Pereira PJS, Limao-Vieira P, Stauffer PR: Numerical 3D modeling of heat transfer in human tissues for microwave radiometry monitoring of brown fat metabolism. In: Conference on Energy-Based Treatment of Tissue and Assessment VII: Feb 3-4 2013; San Francisco, CA. SPIE.

36. Maccarini PF, Rodrigues DB, Oliveira TR, Stauffer PR: Radiometric profiling for brain temperature monitoring. To be submitted 2014.

37. Stauffer PR, Snow BW, Rodrigues DB, Salahi S, Oliveira TR, Reudink D, Maccarini PF: Non-Invasive Core Temperature Measurement in Brain: Demonstration in a Head Phantom and Initial Clinical Experience. The Neuroradiology Journal 2013, Submitted.

38. Rumsey VH: Frequency independent antennas. Proceedings of the Institute of Radio Engineers 1957, 45(3):385-385.

39. Dyson JD: The Equiangular Spiral Antenna. IRE Transactions on Antennas Propagation 1959, AP-7:181-187.

40. Duhamel RH, Isbell DE: Broadband logarithmically periodic antenna structures. Proceedings of the Institute of Radio Engineers 1957, 45(3):385-385.

41. Thaysen J, Jakobsen K, Appel-Hansen J: A logarithmic spiral antenna for 0.4 to 3.8 GHz. Applied Microwave & Wireless 2001.

42. Thaysen J, Jakobsen KB, Appel-Hansen J: A logarithmic spiral antenna for 0.4 to 3.8 GHz. Applied Microwave & Wireless 2001.

43. Dyson J: The Equiangular Spiral Antenna. IRE Transactions on Antennas Propagation 1959, AP-7:181-187.

44. Kaiser JA: The Archimedean two-wire spiral antenna. IRE Transactions on Antennas Propagation 1960, 8(3):312 - 323.

45. Balanis C: Antenna Theory: Analysis and Design, 3 edn. Hoboken, New Jersey: John Wiley & Sons, Inc.; 2005.

46. Ahlbom A, Bergqvist U, Bernhardt JH, Cesarini JP, Court LA, Grandofo M, Hietanen M, McKinlay AF, Repacholi MH, Sliney DH et al: Guidelines for limiting exposure to time-varying electric, magnetic, and electromagnetic fields (up to 300 GHz) (vol 74, pg 494, 1998). Health Physics 1998, 75(4):442-442.

47. Birkelund Y, Klemetsen O, Jacobsen SK, Arunachalam K, Maccarini P, Stauffer PR: Vesicoureteral reflux in children: a phantom study of microwave heating and radiometric thermometry of pediatric bladder. IEEE Trans Biomed Eng 2011, 58(11):3269-3278.

48. Pozar DM: Microwave Engineering, 2nd edn. New York: John Wiley & sons, Inc.; 1998.

49. LaSorte NJ, Barnes WJ, Refai HH, Ieee: Characterization of the Electromagnetic Environment in a Hospital and Propagation Study. Emc 2009: Ieee International Symposium on Electromagnetic Compatibility, Technical Paper 2009:135-140.

50. Federal Communications Commission online table of frequency allocations. In.: http://transition.fcc.gov/oet/spectrum/table/fcctable.pdf; April, 16 2013.

51. Gabriel C: Compilation of the dielectric properties of body tissues at RF and microwave frequencies. In: Occupational and environmental health directorate. Edited by Base BAF. Texas (USA); 1996.

52. Kanda MY, Ballen M, Salins S, Chou CK, Balzano Q: Formulation and characterization of tissue equivalent liquids used for RF densitometry and dosimetry measurements. Ieee Transactions on Microwave Theory and Techniques 2004, 52(8):2046-2056.

53. Jacobsen S, Stauffer PR, Neuman DG: Dual-mode antenna design for microwave heating and noninvasive thermometry of superficial tissue disease. Ieee Transactions on Biomedical Engineering 2000, 47(11):1500-1509.

54. Arunachalam K, Maccarini PF, De Luca V, Bardati F, Snow BW, Stauffer PR: Modeling the detectability of vesicoureteral reflux using microwave radiometry. Phys Med Biol 2010, 55(18):5417-5435.

55. Duhamel RH, Scherer JP: Frequency-independent antennas. In: Antenna Engineering Handbook. Edited by Johnson RC, 3rd edn. New York: McGraw-Hill, Inc.; 1993.

56. Carr KL: Microwave Radiometry - Its Importance to the Detection of Cancer. Ieee T Microw Theory 1989, 37(12):1862-1869.

57. Mizushina S, Ohba K, Abe K, Mizoshiri S, Sugiura T: Recent trends in medical microwave radiometry. IEICE Transactions on Communications 1995, E78-B(6):789-798.

58. Sterzer F: Microwave radiometers for non-invasive measurements of subsurface tissue temperatures. Automedica 1987, 8:203-211.

59. Shaeffer J, El-Mahdi AM, Carr KL: Cancer detection studies using a 4.7 Gigahertz radiometer. Cancer Detect Prev 1981, 4(1-4):571-578.

60. Sessler DI: Perioperative heat balance. Anesthesiology 2000, 92(2).

61. Hayman LA, Shukla V, Ly C, Taber KH: Clinical and imaging anatomy of the scalp. Journal of Computer Assisted Tomography 2003, 27(3):454-459.

CHAPTER 3

Chapter 4

Target-specific multiphysics model for murine bladder heating studies

Abstract

Purpose: Murine tumor models are often used to study new cancer treatments. To investigate thermally enhanced treatments, appropriate heating techniques must be established for each tumor site. The classic approach used to design microwave antennas for local heating involves SAR (specific absorption rate) rather than temperature optimization, even though temperature is the ultimate goal. In this project, we develop a model that characterizes all major thermal mechanisms that affect local heating of murine bladder with a microwave applicator, including body thermoregulation, anesthesia and accurate environmental conditions.

Methods: A micro magnetic resonance scan was segmented using Avizo v7 software to demarcate the bladder, uterus and large intestine from a female mouse with 20 g weight. The segmented 3D objects are imported into COMSOL Multiphysics v4.2 to implement a fully coupled fluid dynamics and heat transfer analysis, which combine SAR calculated from Ansys HFSS v15 with blood perfusion, heat conduction, metabolic heat production, thermal storage, natural convection currents within the urine, skin surface radiation and air convection. In the hyperthermia temperature range, both perfusion and metabolism increase with temperature. These variations are significant and increase the complexity of the model since nonlinear solvers must be used. For experimental confirmation, mice are placed on a 38 °C heated pad. This way, mice are maintained at thermoneutral conditions and thus avoid anesthesia-induced hypothermia. Also, the antenna has a water bolus with controlled temperature to avoid overheating skin. A goal function is established to ensure that the bladder is heated efficiently in the therapeutic range [42, 43] °C while sparing the remaining tissues from high temperatures (>42 °C).

Results: The optimized bolus temperature is 37 °C using 13 W as input antenna power. This particular arrangement maintains the bladder in a therapeutic range [41.5, 43.3] °C

while sparing the remaining tissues from dangerous temperatures: the maximum non-target tissue temperature is 42.8 °C in the subcutaneous tissue. The simulated temperatures of the organs are in agreement with experimental results. The simulated average temperature in the uterus follows closely ([0.8, 1.0] °C) the average temperature in the bladder. Thus, the uterus becomes a viable surrogate for bladder monitoring without invasive probes.

Conclusions: A new thermo-fluid model allows a temperature-based optimization of murine bladder heating with water-cooled microwave applicator. This complete analysis shows that temperature dependent biological properties as well as the effects of anesthesia must be accounted to capture the transient temperatures in mice. Numerical and experimental results are consistent and thus validating the thermo-fluid model and consequently the efficacy of this local bladder heating approach. This analysis can be extended to be used in clinical thermal therapy planning for deep-seated targets such as tumors.

Keywords: Microwave hyperthermia, Bioheat transfer, Fluid dynamics, Bladder cancer, Specific absorption rate, Thermoregulation, and Anesthesia.

This chapter addresses research work carried out on the target-specific multiphysics modeling for murine bladder heating studies, and has been published/submitted for publication as follows:

1. **Rodrigues DB**, Salahi S, Pereira PJS, Limão-Vieira P, Landon CD, Oliveira TR, Etienne W, Inman BA, Dewhirst MW, and Stauffer PR et al: Target-specific multiphysics model for murine bladder heating studies. Physics in Medicine and Biology 2013, Submitted.
2. Colebeck E, **Rodrigues DB**, Maccarini PF, Stauffer PR, TopSakal E: Brown and white fat dielectric properties in rats. Physics in Medicine and Biology 2013, Submitted.
3. Salahi S, Maccarini PF, **Rodrigues DB**, Etienne W, Landon CD, Inman BA, Dewhirst MW, Stauffer PR: Miniature microwave applicator for murine bladder hyperthermia studies. International Journal of Hyperthermia 2012, 28(5):456-465.

4. **Rodrigues DB**, Salahi S, Pereira PJS, Limão-Vieira P, Maccarini PF, Stauffer PR: A temperature optimization technique for localized heating in small animals. In: 2012 Society of Thermal Medicine Annual Meeting: April 13-16; Portland OR, EUA: Edited by Mercer J. 2012.
5. Salahi S, **Rodrigues DB**, Maccarini PF, Stauffer PR: Wideband conformal metamaterial antenna for pediatric bladder hyperthermia. In: 2012 Society of Thermal Medicine Annual Meeting: April 13-16; Portland OR, EUA: Edited by Mercer J. 2012.

Award:

ANSYS HALL OF FAME 2013

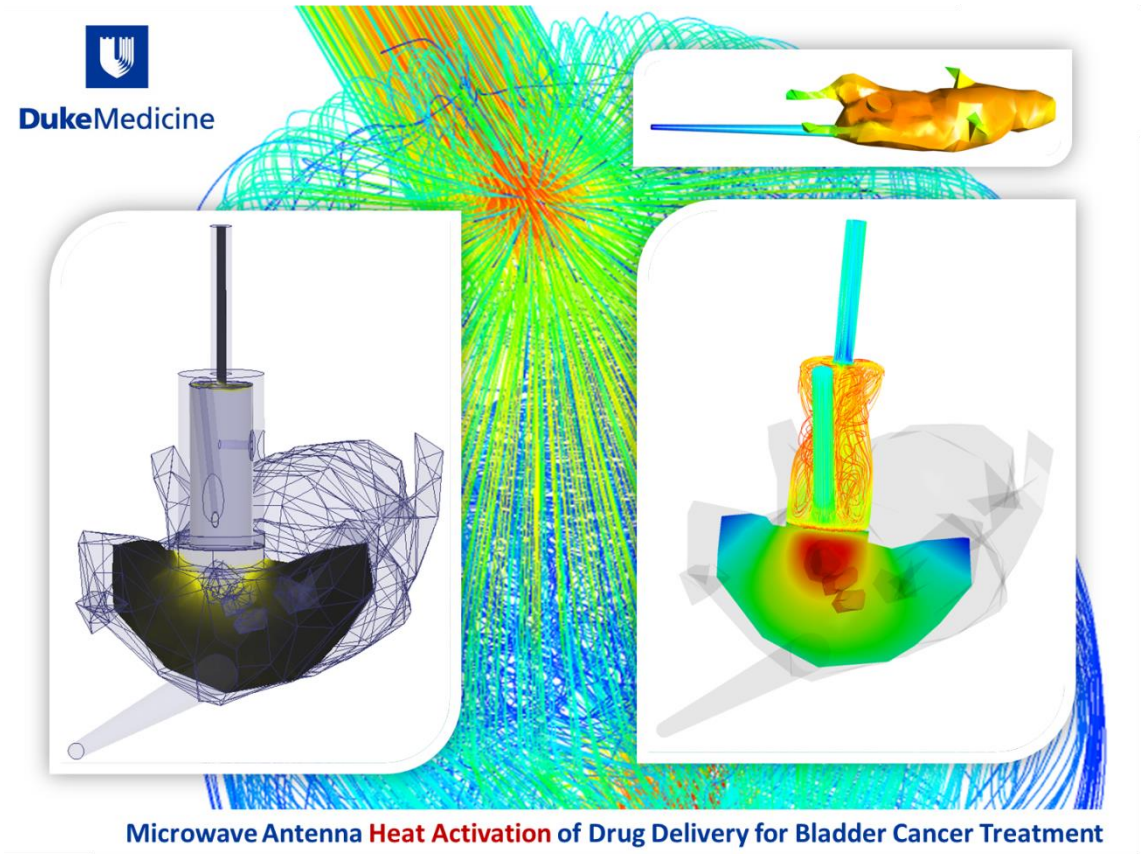

4.1. Introduction

Superficial bladder cancer is currently treated with intravesicular chemotherapy using mitomycin-C (MMC). Similarly to other chemotherapy drugs, tumor cells, however, eventually develop a resistance to MMC, rendering the treatment less effective or completely ineffective [1]. *In vitro* studies have shown that the application of hyperthermia (increasing temperature to [42, 43] °C) to cancer cells increases their sensitivity to MMC and reverses MMC resistance [2]. Hyperthermia has other relevant effects on tumor microenvironment [3]: elevated tissue temperature increases blood perfusion, tumor metabolic rate, permeability of blood vessel wall, and consequently enhanced drug uptake into the tumor cells [4]. Hyperthermia can also be used in combination with thermosensitive liposomes to increase the efficacy of drug delivery to tumors, as shown in [5], using another drug, namely doxorubicin. Furthermore, a recent pilot study in 18 patients demonstrated a safe and reliable method for heating bladder in [40, 43] °C as an adjuvant therapy during MMC treatments [6]. Given the promising implications of all these studies, we are now interested in using established murine bladder cancer models to study the mechanisms behind the increased effectiveness while using adjuvant hyperthermia in MMC/doxorubicin treatments.

The most commonly used method for inducing hyperthermia in murine tumors is to submerse the tumor bearing portion of the mouse into a hot water bath [7-11]. This method has been useful mainly for tumors in the hind limb, where the region immersed can be limited primarily to the target tumor mass. However, this method cannot provide selective power deposition into tissues located in deep regions. On the other hand, methods based on water bath heating of murine bladder would require circulation of heated water through the bladder or submersing the lower half of the mouse's body. The first method is not technically achievable for a small bladder (0.15 ml volume) and the latter one would heat the entire lower region of the mouse. This would increase the mouse's core temperature to dangerous levels, which could induce toxic effects. Other methods for local heating of deep-seated organs like the urinary bladder have been explored. A few examples include ultrasound transducers [12] and RF (radiofrequency) heating with parallel-plate configurations which have been shown to heat effectively superficial flank tumors in mice [13]. Ferrite powder [14, 15], water-based ferrofluids [16] or iron oxide nanoparticles [17] could be instilled into the bladder and heated up with the application of an external magnetic field. Although these methods are

potentially effective, they are expensive and may require invasive methods to effectively deliver the metal powders, ferrofluids or nanoparticles to the region of interest.

Our research group introduced recently a novel microwave antenna applicator [18] to non-invasively heat deep-seated targets in small animals. The applicator consists of a circular waveguide antenna which design parameters were optimized to focus electromagnetic (EM) power deposition in the bladder. The power deposition was quantified in terms of Specific Absorption Rate (SAR in W/kg) and is dependent on the EM-field and the input power of the antenna (P_{ant}). Furthermore, the near-field antenna deposition pattern is typically very energetic and non-uniform [19]. The applicator thus integrates a water circulation system with controlled temperature that serves two purposes: focus the microwave heating into deeper regions by removing heat from the surface and avoids overheating the skin and subcutaneous tissue.

In this work, we use the previous applicator to develop a target-specific multiphysics model for microwave localized heating in the mouse's bladder region. We account for all major thermal mechanisms that affect local heating of murine bladder with a microwave applicator, including body thermoregulation, anesthesia, forced convection due to water circulation and accurate environmental conditions. In particular, and to our knowledge, the effect of anesthesia was not yet accounted in any biological heat transfer model. One approach to develop a mouse model is to scale down existing rat models. However, this strategy presents questionable accuracy due to the different organ and body proportions [20]. Thus, we develop a 3D reconstruction of the mouse and its critical anatomical structures.

SAR results are used in the heat transfer model as a heat source and are calculated independently from the heat transfer model. This uncoupled simulation is valid since electrical properties do not change significantly in the hyperthermia temperature range (below $\leq$ 44 °C) [21, 22]. The input temperature of the water-loaded waveguide (T_{bolus}) requires a coupled thermo-fluid simulation between the waveguide and antenna. Urine fluid dynamics is also simulated to account for possible convection currents within the bladder region. This multiphysics model is schematized in Figure 4.1 and includes more two important elements to be analyzed: the effect of anesthesia on the overall heat transfer analysis and the temperature dependence of biological properties that is especially relevant in animals with high surface-area-to-volume ratio, such as mice.

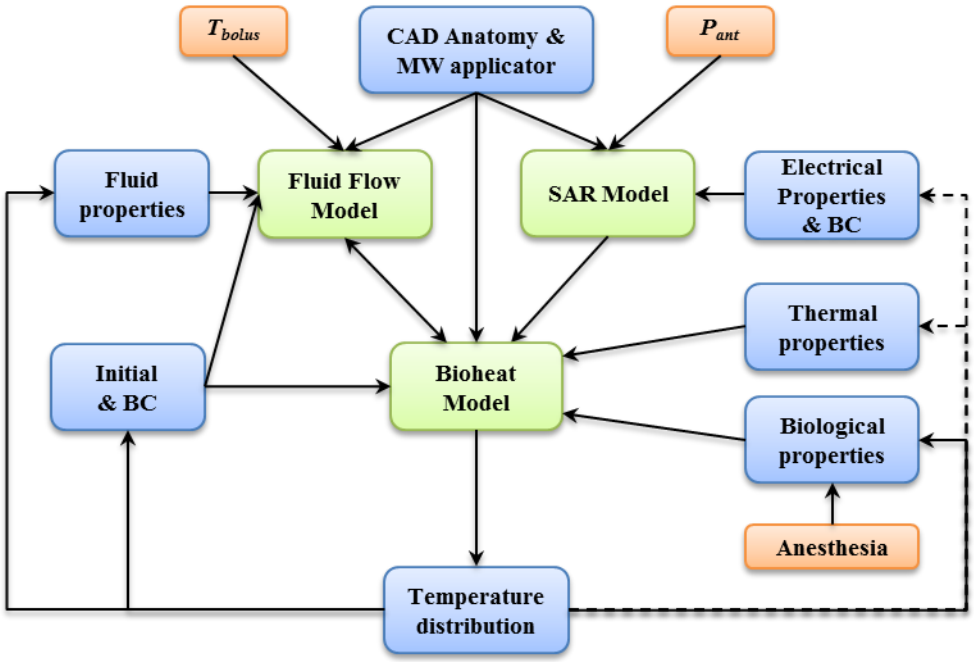

Figure 4.1 – Multiphysics modeling: steps in the bioheat transfer model involving heat sources from microwave (MW) heating coupled to a thermo-fluid model to simulate the forced convection at the interface mouse/antenna and natural convection in the urine. The term bioheat is used to characterize the heat transfer in biological tissues. The dotted line represent the temperature independence of thermal and electrical properties which is valid in the hyperthermia range ([37, 44] °C).

Both input parameters – antenna power (P_{ant}) and cooling bolus temperature (T_{bolus}) – are user-controllable and used in a temperature-based optimization algorithm. The goal function is to ensure that the bladder is heated efficiently in the therapeutic range [42, 43] °C while sparing the remaining tissues from high temperatures (>42 °C).

The determination of proper temperature profiles inside living biological tissues is a complicated and challenging scientific task. This is due to the variety of thermal mechanisms intrinsic to biological systems and to uncertainties in parameter values obtained from laboratory tests in vivo. These uncertainties may result from: the heterogeneous nature of the biological tissue, the temperature of the sample, the age and type of the species, the preparation procedure of biological samples and the level of anisotropy in the tissue [23]. To reduce the uncertainty associated with biological properties, the biological data presented in this work are chosen for our particular experimental setup. Moreover, the multiphysics model is formulated to be applied to any experiment or even using other miniature applicator designs.

4.2. Methods

In this section, we first introduce the experimental setup since it is essential to understand its steps in order to develop an accurate transient computational model. The microwave applicator is presented afterwards so we can further develop the modeling strategy for simulating focused bladder heating in mice. This strategy couples the virtual device with the virtual mouse as well as the different physics involved in the microwave heating. Thus a multiphysics computational model is created.

4.2.1. Experimental setup for in vivo murine bladder heating studies

A female C57BL/6 mouse (20 g weight, 11 weeks old) is anesthetized with 65 mg/kg sodium pentobarbital (Nembutal). The mouse is placed on a thermal pad at 38 °C to maintain thermoneutral conditions throughout the experiment (Figure 4.2). This particular anesthesia leads to an 8 °C decrease in core temperature which takes around 30 min [24, 25] to establish. Heating performance of the applicator is tested in mouse with full bladder volumes of, approximately, 0.15 ml. Temperature measurements in the mouse pelvis are obtained from Luxtron fiber optic probes (LumaSense Technologies, Santa Clara, CA) inside polyurethane catheters with 0.81 mm diameter. These catheters are inserted in three different locations and placed under the circular waveguide antenna: invasively in the subcutaneous tissue ([0,1] mm depth), through vagina up to the uterus ([2, 3] mm depth) and through rectum up to the large intestine ([4, 5] mm depth). Systemic temperature is measured with a fiber optic probe inserted orally. The temperatures are collected and displayed in real-time using LabVIEW software (National Instruments, Austin, TX). This software allows the user to manually control the applicator power as needed to maintain the desired temperature distribution in the mouse. Murine *in vivo* studies described in this work are conducted in accordance with the Institutional Animal Care and Use Committee at Duke University.

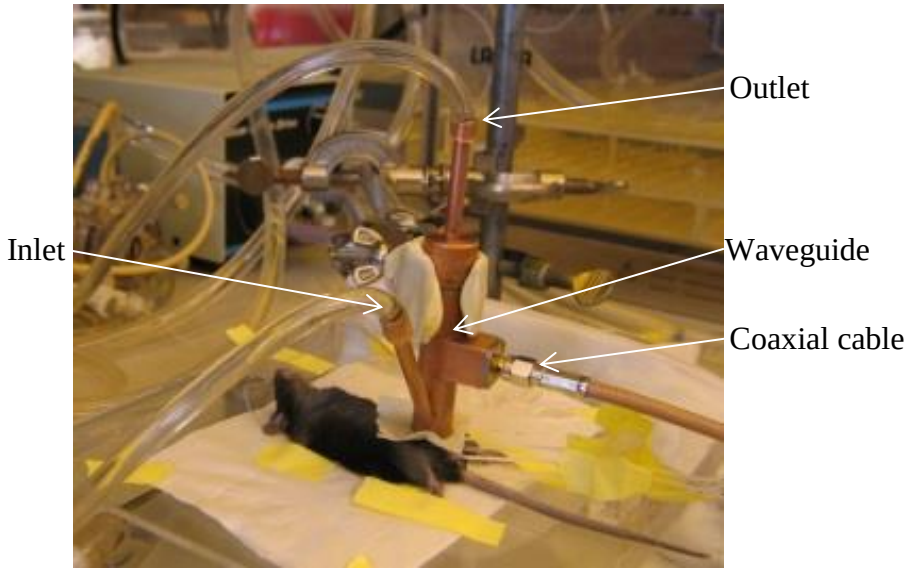

Figure 4.2 –Snapshot of experimental setup for murine bladder hyperthermia study with applicator positioned on mouse lower abdomen.

4.2.2. Microwave hyperthermia applicator

The hyperthermia applicator was developed for murine studies and consists of a deionized water-loaded circular waveguide that operates at 2.45 GHz (Figure 4.3). The antenna design parameters (Figure 4.3a) were optimized for power deposition in the murine bladder (based on SAR) and for reducing the mismatch (S_{11}, see equation (1)) at the interface between antenna and mouse. This optimization led to an optimal waveguide of 9.5 mm diameter and a probe length of 1.5 mm (Figure 4.3) [18]. The backshort distance was fixed at 3.4 mm (λ/4, where λ is the wavelength).

The antenna integrates a surface cooling system (bolus) as shown in Figure 4.3c, which allows cooling the surface at a certain temperature (T_{bolus}) and remove the excess of heating from the skin and subcutaneous tissue. The corresponding virtual device was designed in HFSS v15 (Ansys Inc, Philadelphia PA) and is presented in Figure 4.3d.

The S_{11} values are here given in decibels as follows:

$$S_{11}(dB) = 20\log_{10}\left(|\Gamma|\right) \quad (1)$$

where Γ is the input voltage reflection coefficient [26].

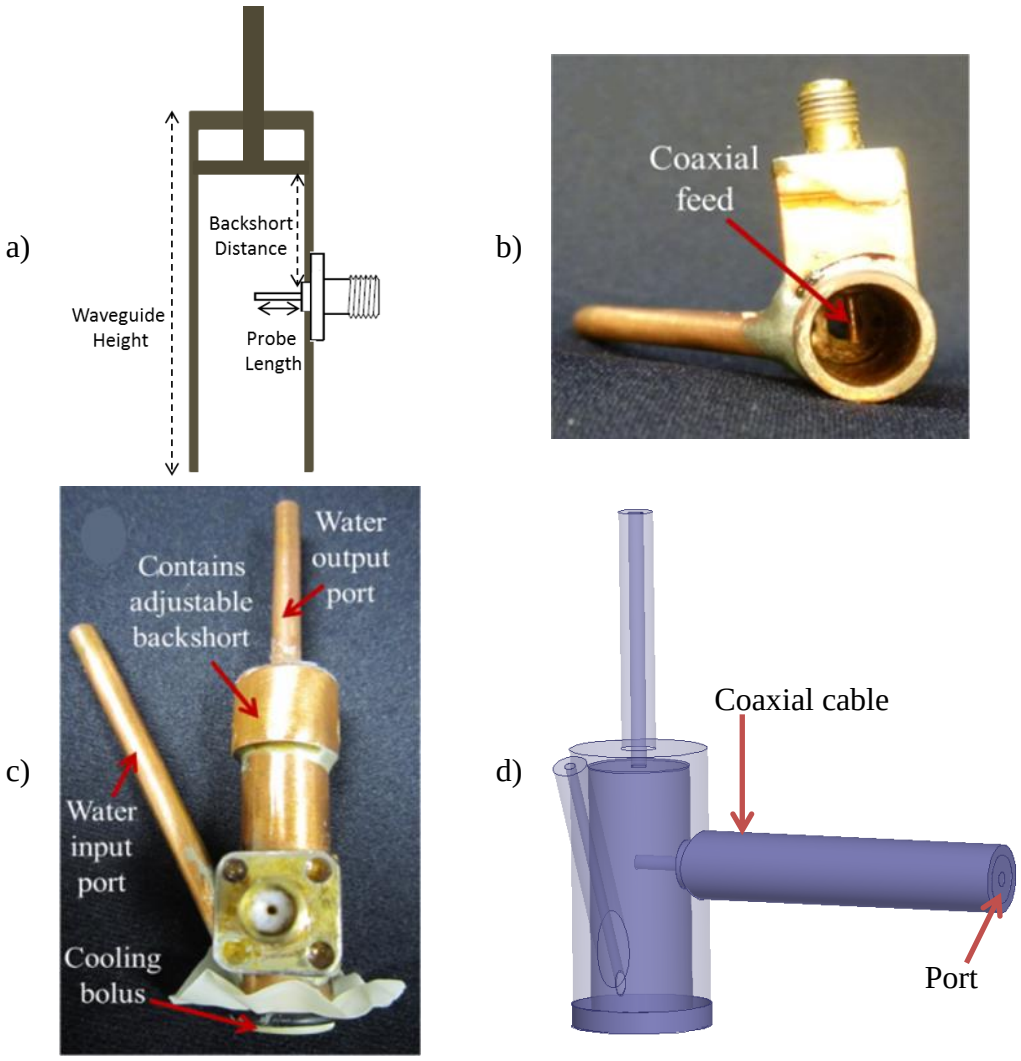

Figure 4.3 – Microwave applicator: a) parameters to optimize SAR and S_{11}; b) bottom-view of 2.45 GHz applicator; c) front-view of the 2.45 GHz applicator; d) virtual applicator designed in HFSS 15.

4.2.3. Virtual mouse phantom

The 3D computer-aided design (CAD) model of the mouse is accurately developed from micro magnetic resonance (microMR) images obtained from Duke University's Center for In Vivo Microscopy (7T Magnex Scientific magnet). The images are used to create the 3D model with a resolution of 6.25 μm in all three dimensions. Using Avizo software package v7 (Visualization Sciences Group, Burlington, MA), the microMR images are segmented to yield 3D surfaces of the mouse's body and the critical organs, *i.e.*, bladder, uterus, and large intestine (Figure 4.4a). These surfaces are assumed to be the outer boundary of a uniform volume of tissue and imported to DesignModeler (Ansys Inc., Philadelphia PA) for further clean-up of geometry irregularities. The mouse's tail is not possible to accurately be segmented in Avizo and is created in

DesignModeler by means of an elongated (80.0 mm length) and thin cone (3.4 mm base diameter) to mimic real tail geometry. A concentric cone with 1.9 mm base diameter is subtracted to the previous object to mimic the inner bone. The brain, heart, liver and kidneys are also incorporated in DesignModeler. Although these organs are not in the heating region, they play a relevant role in the mice heat balance as will be discussed latter. The bladder region is scaled to create a urine domain and a thin bladder wall with 0.35 mm thickness. The remaining region of the virtual mouse is composed of an homogeneous mixture of 89% lean mass, 9% fat and 2% bone [27]. This region is denoted by "body" in the remaining document. Figure 4.4b shows the applicator positioning over the pelvis.

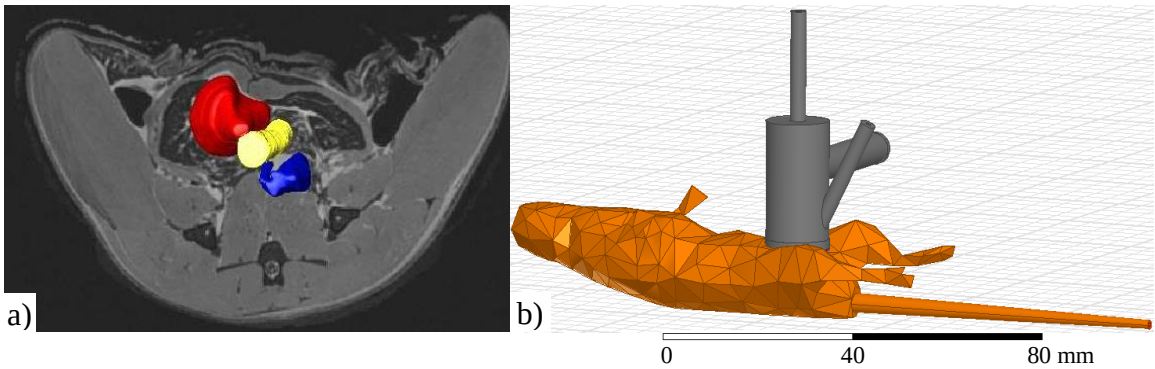

Figure 4.4 – 3D CAD model of the mouse: a) transversal section of the caudal part of the body in the region of the urinary bladder (red) and its adjacent organs: uterus (yellow) and large intestine (blue); b) virtual mouse coupled with the MW applicator.

4.2.3.1. Thermophysical properties

Mouse thermal properties (density ρ, specific heat capacity C_p and thermal conductivity k) are presented in Table 4.1 and assumed to be the same as in humans [28, 29]. The electrical properties (relative permittivity ε_r and electric conductivity σ) used in the model are frequency dependent [30] and presented in Table 4.1 for 2.45 GHz. Urine electrical properties are characterized at normothermic temperature (37 °C) using a coaxial dielectric probe (E85070C, Agilent Technologies, Santa Rosa CA) connected to a network analyzer (E5071C, Agilent Technologies).

Table 4.1 – Mice thermal and dielectric properties.

Tissue	ρ (kg/m^3)	C_p (J/kg/K)	k (W/m/K)	σ (S/m)	ε_r
Skin	1109	3391	0.37	1.592	42.853
Fat	911	2348	0.21	0.105	5.280
Muscle	1090	3421	0.49	1.739	52.729
Bladder wall	1086	3581	0.52	0.685	18.001
Uterus	1088	3655	0.54	2.247	57.814
Intestine	1088	3655	0.54	3.170	54.425
Bone	1762	1505	0.32	0.477	12.814
Body	1036	3099	0.41	1.249	38.494
Blood	1050	3617	0.52	2.545	58.264
Urine	1035	4174	0.56	7.427	71.238
Brain	1046	3630	0.51	1.511	42.539
Heart	1081	3686	0.56	2.256	54.814
Kidneys	1066	3763	0.53	2.430	52.742
Liver	1079	3540	0.52	1.686	43.035

4.2.4. SAR model

In microwave (MW) frequencies, heating is primarily induced through power deposition due to ionic conduction and dielectric losses, which is directly proportional to the electric field (***E***-field) [31]. The ***E***-field maintained by the antenna is calculated by solving the wave equation derived from Maxwell's equations assuming a time-harmonic electric field $\boldsymbol{E}_i(\boldsymbol{r},t)=\boldsymbol{E}_{0i}(\boldsymbol{r})\exp(j\omega t)$, which is given by

$$\nabla^2 \boldsymbol{E}_{0i}(\boldsymbol{r}) + \omega^2 \mu_0 \varepsilon_0 \varepsilon_{ci} \boldsymbol{E}_{0i}(\boldsymbol{r}) = \boldsymbol{0} \tag{2}$$

where

$$\nabla^2 \boldsymbol{E}_{0i}(\boldsymbol{r}) = \nabla^2 E_{0ix}(\boldsymbol{r})\boldsymbol{e}_x + \nabla^2 E_{0iy}(\boldsymbol{r})\boldsymbol{e}_y + \nabla^2 E_{0iz}(\boldsymbol{r})\boldsymbol{e}_z \tag{3}$$

Equation (2) is solved using the finite element method (FEM) in HFSS and $\boldsymbol{r}$ (m) is the 3D position vector inside the computational domain, ε_0 and μ_0 are free space dielectric permittivity (8.854×10^{-12} F/m) and magnetic permeability (1.257×10^{-6} N/A^2), respectively, $\varepsilon_{ci} = \varepsilon_{ri} - j\sigma_i/(\omega\varepsilon_0)$ is the complex dielectric permittivity that is modeled to be homogeneous within each medium and $\omega = 2\pi f$ is the angular frequency (Hz).

Moreover E_{0il} ($l = x,y,z$) are the components of the electric field $\boldsymbol{E}_{0i}$. Note that equation (2) is only valid for non-magnetic materials (e.g. biological tissues) where magnetic permeability is approximated to μ_0 [32]. The subscript i represents each individual region ($1 \leq i \leq n$, $n \in \mathbb{N}$ with n the number of regions) in the computational domain that includes both the antenna and mouse. For convenience, we drop the subscript i throughout this chapter except in the numbered equations.

We use a tangential element basis function of the first order to interpolate field values from both nodal values at vertices and on edges. First order basis functions use 20 unknown variables per tetrahedron with quadratic interpolation. In HFSS the initial edge length l_t of each tetrahedral element is determined from the material's relative permittivity ε_r and operating frequency f using $l_t = c/(3 \cdot f \cdot (\varepsilon_r)^{1/2})$. The mesh is then automatically refined based on the computed $\boldsymbol{E}$-field to obey a maximum deltaS = 0.02, where deltaS is the change in the magnitude of the scattering parameters (S_{11}) between two consecutive iterations. We surround the virtual head phantom with an air domain to study the possibility of developing $\boldsymbol{E}$-fields surrounding the antenna. An absorbing boundary condition (named radiation boundary in HFSS) is imposed at the boundaries of the full computational domain. This boundary condition guarantees that none of the wave propagating to the boundary is reflected back into the computational domain [26].

In order to simulate the energy input in the solution domain, a wave port is assigned in the coaxial entry port (Figure 4.3d). In HFSS, a wave port represents the region where the source supplies energy to the solution domain. Firstly, HFSS calculates a 2D solution for the wave port and subsequently uses that solution as the source for the 3D model. The 2D solution is achieved by exciting the port with an incident wave mode with power correspondent to P_{ant} [33].

Once the $\boldsymbol{E}$-field is calculated, it is necessary to compute the energy absorption within tissues which is responsible for the temperature increase. As mentioned, the absorption is characterized by the Specific Absorption Rate (*SAR*) and is given by the amount of energy absorbed per unit mass (W/kg). SAR is given by

$$SAR_i(\boldsymbol{r}) = \frac{\sigma_i}{2\rho_i}\left|\boldsymbol{E}_{0i}(\boldsymbol{r})\right|^2 \tag{4}$$

4.2.4.1. S_{11} and SAR Validation

We use a latex membrane sealed over the front opening of the waveguide to contain the circulating water. The applicator is then placed adjacent to skin over the pelvis of C57BL/6 mice (Harlan Laboratories, Indianapolis, IN) and S_{11} is measured using an Agilent E5071C network analyzer. To confirm the validity of SAR patterns simulated by HFSS, the SAR pattern of the applicator is measured with an electric field probe (APREL Laboratories, Ottawa, Ontario, Canada). This probe is used to scan a 3D tank a with a 1 mm step size. This tank contains tissue-equivalent liquid using procedures that have been published previously [34]. In particular, the tank contains a mixture of Tween 80 and deionized water to create a liquid that simulates muscle tissue at 2.45 GHz. The measured dielectric constant is within 5% and the electrical conductivity within 1% of published values [35].

4.2.5. Bioheat transfer model

To simulate heat transfer in biological tissues – bioheat transfer – it is necessary to account for the convective effect of blood perfusion and the heat generation caused by metabolism. In 1948, Pennes developed a model that accounted for these two biological properties as well as other external heat sources [36, 37]:

$$\rho_i C_{pi} \frac{\partial T_i}{\partial t}(\boldsymbol{r},t) = \nabla \cdot \left(k_i \nabla T_i(\boldsymbol{r},t)\right) + B_i(\boldsymbol{r},t) + M_i(\boldsymbol{r},t) + P_{di}(\boldsymbol{r}) \quad (5)$$

where

$$P_{di}(\boldsymbol{r}) = \rho_i SAR_i(\boldsymbol{r}) \quad (6)$$

and P_d is the volumetric power loss density (W/m^3). The use of both P_d and *SAR* is due to the fact that physicians are used to the terminology *SAR* whereas for heat transfer purposes P_d is more suitable due its units. The heat transfer in tissues described by equation (5) is controlled by heat storage $\rho C_p \partial T/\partial t$, thermal conduction $\nabla\cdot(k\nabla T)$ derived from Fourier's Law**,** dissipation of heat through blood flow *B*, metabolic heat rate *M* and by the heat source P_d that represents the volumetric heat generation converted from electromagnetic energy [36-38]. All these quantities have units of power per unit volume (W/m^3). Despite limitations [37, 39], such as the simplification of blood vascular network, Pennes' model has been experimentally validated [40] and often

chosen for the development of numerical schemes in mouse studies [18, 41-44]. The temperature dependence of the thermophysical properties ρ, C_p and k are not accounted in this model since it only becomes relevant for higher temperatures than the ones used in hyperthermia, such as ablation [21, 22].

4.2.5.1. Boundary conditions

The heat transfer in mouse skin takes into account heat losses due to air convective cooling and thermal radiation governed by Stefan-Boltzmann law. The combined boundary condition of both surface heat transfer effects is given by

$$-\boldsymbol{n}\cdot\left(k_{skin}\nabla T_{skin}(\boldsymbol{r},t)\right)=h_{air}(T_{skin}(\boldsymbol{r},t)-T_{air})+\sigma_b\varepsilon_{skin}(T_{skin}^4(\boldsymbol{r},t)-T_{air}^4) \quad (7)$$

where $\boldsymbol{n}$ is the unit vector normal to the skin surface, h_{air} is the air heat convection coefficient (W/m^2/K), T_{air} is room temperature (K), σ_b is the Stefan-Boltzmann constant (5.67×10^{-8} W/m^2/K^4) and ε_{skin} is the average dimensionless body emissivity constant. The convection coefficient h_{air} at the skin surface is given by [45]

$$h_{air}=\frac{\left(\rho C_p\alpha\right)_{air}}{2.7d^{0.4}(\upsilon_{air}/v_{air})^{0.6}} \quad (8)$$

where $(\rho\, C_p)_{air}$ is the volumetric heat capacity of air (J/m^3/K), α_{air} is the thermal diffusivity of air (m^2/s), d is a characteristic dimension of the mouse (m), v_{air} is wind speed (m/s) and υ_{air} is kinematic viscosity of air (m^2/s).

Table 4.2 – Heat exchange properties at skin at 25 °C.

Property	Value	Unit	Reference
ε_{skin}	0.82	-	[46]
$(\rho C_p)_{\text{air}}$	1198.4	J/m^3/K	[46]
α_{air}	22×10^{-6}	m^2/s	[46]
d body	0.085	m	Measured
υ_{air}	15.5×10^{-6}	m^2/s	[46]
v_{air}	0.05	m/s	[41]
h_{air}	3.33	W/m^2/K	From equation (8)

When combined, convection and radiative effects are three times higher in the tail of a deer mouse (similar weight to C57BL/6 mice) than in the furry torso at room temperature [47]. Therefore, heat transfer coefficients can be estimated leading to a $\varepsilon_{skin,tail}$ = 0.90 and $h_{air,tail}$ = 19.98 W/m^2/K. The temperature of the water entering the bolus is set to a constant T_{bolus} and is user-controllable. The mouse lies on a heat pad set to T_{pad} (around 38 °C) to compensate the heat loss due to anesthesia.

Heat loss through respiration is omitted since we assume that is does not affect heat transfer in the bladder region. Evaporation is not expected to occur since mice are being heated to be at thermoneutral conditions and present impaired thermoregulation due to anesthesia. Mice have other behavioral thermoregulation mechanisms [48], such as saliva spreading to increase evaporative water loss, but these mechanisms are not possible due to anesthesia. The particular case of saliva spreading would also involve an autonomic response – increased saliva production – that is also impaired due to anesthesia. In awake mice, physiological stress and exercise increase body temperature and should be accounted in the bioheat transfer model [41, 42].

4.2.5.2. Blood perfusion

Blood perfusion can be estimated using the volumetric blood flow rate ω_B (kg/s/m^3). In Pennes' model, blood perfusion is represented by a heat sink term given by

$$B_i(\boldsymbol{r},t) = \omega_{Bi}(\boldsymbol{r},t) C_{p,b}\left(T_a - T_i(\boldsymbol{r},t)\right) \tag{9}$$

where T_a is arterial blood temperature and $C_{p,b}$ is the specific heat capacity of blood (Table 4.1). During hyperthermia blood perfusion behaves as a heat sink that accounts for the convective cooling caused by blood, thus removing the excess heating in the thermally stressed areas. In Pennes' model, perfusion is assumed to be non-directional and is only valid for tissues with healthy microvasculature, blood flowing through vessels with isotropically distributed orientations and dimensions not exceeding 0.2 mm diameter. In other scenarios directional effects of blood flow should be included [21, 49]. Note that we account for blood perfusion temperature dependence whereas in the classical Pennes' model blood perfusion is considered constant [50].

Blood perfusion plays a key role in hyperthermia treatments and depends on a wide variety of factors besides temperature: factors local to the tissue (pH, O_2, type of tissue,

size of tumor); external factors which directly control local flow (parasympathetic nervous system, hormones); external factors that affect indirectly local blood flow (heart rate, blood pressure, skin temperature, anesthesia); and also on the therapeutic approach, e.g., the type, duration and number of hyperthermia treatments [51-53]. It is a complex biological phenomenon and we must rely on experimental-based models to estimate blood perfusion parameter dependences.

Song experiments [54] in muscle and skin of Sprague Dawley (SD) rats demonstrated that exist a tissue-dependent threshold (T_{cr}) where blood vessels start to shut down due to excessive stress and as a consequence blood perfusion drops [50]. In these experiments, temperature dependence assumed a semi-Gaussian profile [22, 55] given by

$$\omega_{Bi}(\mathbf{r},t) = \omega_{0i}\left(1+\omega_{1i}(t_{heat})\exp\left(-\frac{(T_i(\mathbf{r},t)-T_{cri}(t_{heat}))^2}{s_i(t_{heat})}\right)\right) \tag{10}$$

where ω_0 is basal blood perfusion, and coefficients s and ω_1 as well as T_{cr} are dependent on tissue and heating time (t_{heat}). Table 4.3 shows these coefficients for t_{heat} = 15 min, determined from Song experiments [54]. Due to lack of experimental data, organ tissues are assumed to have the same coefficients as muscle. Note that although our final goal is to address bladder tumors, the experiments are carried out in normal bladders thus we use bladder properties.

As mentioned, blood perfusion is also dependent on anesthesia. Diller *et al.* [52] compiled perfusion data for different animals – including rats – and compared the effects of different anesthetics. Since there are no mice studies included, we choose to analyze rat's perfusion data; we focus on the studies where sodium pentobarbital was administrated and compare blood perfusion results with and without this anesthetic [56, 57]. We define R_ω as the anesthesia induced change in rat's blood perfusion and assume it to be the same as in mice. The resulting impaired blood perfusion by anesthesia ω_A is then given by

$$\omega_{Ai} = R_{\omega i}\omega_{0i} \tag{11}$$

Although equation (11) does not capture the transient decrease of blood perfusion, it is valid for steady state conditions. We choose basal blood perfusion (ω_0) in mice from Stott *et al.* [58] since they used the same anesthetic and concentration as in the

aforementioned experiment: sodium pentobarbital (60 mg/kg). The full list of perfusion related properties is presented in Table 4.3.

Table 4.3 – Mice blood perfusion properties with and without anesthesia: effect of sodium pentobarbital (60 mg/kg) and temperature dependent parameters for 15 min heating time.

Tissue	ω_0 (kg/s/m^3)	ω_A (kg/s/m^3)	R_ω	ω_1	s (°C^2)	T_{cr} (°C)
Skin	2.038	1.359	0.67	13.146	1.6	45
Body	7.139	2.161	0.30	3.896	3	45
Bladder wall	25.889	17.295	0.67	4.336	3	45
Uterus	34.239	19.932	0.58	4.336	3	45
Large intestine	42.589	21.134	0.50	4.336	3	45
Bone	1.650	1.336	0.81	0.334	3.5	45
Brain	27.931	15.925	0.57	4.336	3	45
Heart	77.025	41.051	0.53	4.336	3	45
Kidneys	34.660	27.983	0.81	4.336	3	45
Liver	33.636	22.470	0.67	4.336	3	45

4.2.5.3. Metabolism

The quantification of metabolism in murine is not straightforward, especially because of murine's core temperature instability throughout the day [48, 59]. The total metabolic heat production in mice is given by the sum of a basal value M_0 (W/m^3) and an additional heat term, which may be produced by local autonomic responses such as normal activity, shivering and/or non-shivering thermogenesis [42, 60]. In the current study, the mouse is anesthetized and heated with a thermal pad at 38 °C to maintain thermal comfort. Thus, the mentioned autonomic responses do not occur and are not taken into account in the metabolic heat rate modeling. During heating, however, the autonomic thermoregulatory response due to temperature increase becomes significant and must be accounted. In the hyperthermia range of temperature, metabolism seems to have a linear behavior with temperature as suggested by Gillooly *et al.* [61]. His theory is that metabolism is governed by temperature through its effects on rates of biochemical reactions that vary with temperature according to the Boltzmann-Arrhenius law (equation (12))

(12) $$M_i(\boldsymbol{r},t) = M_{0i}\exp\left(E_a\frac{T_i(\boldsymbol{r},t)-T_i(\boldsymbol{r},0)}{k_B T_i(\boldsymbol{r},t)T_i(\boldsymbol{r},0)}\right)$$

where k_b is the Boltzmann constant (8.62×10^{-5} eV/K) and E_a is the mean activation energy (eV) of metabolism that is species-dependent and can be determined empirically [62]. The activation energy for mice is here determined from the average of three independent mice studies – 0.69 eV [66] and 0.67 eV [67, 68] – yielding E_a = 0.68 eV. These values are within the predicted range [0.6, 0.7] eV for activation energy [63].

Another approach to quantify the temperature dependence of metabolism is given by the van't Hoff Q_{10} effect [64]

(13) $$M_{iQ_{10}}(\boldsymbol{r},t) = M_{0i}Q_{10}^{\frac{T_i(\boldsymbol{r},t)-T_i(\boldsymbol{r},0)}{10}}$$

where Q_{10} is a species-dependent constant determined empirically. Comparing equations (12) and (13), one can conclude that these expressions are mathematically equivalent if Q_{10} is temperature dependent and determined by equations (12) and (13). In fact, Q_{10} values are temperature dependent by definition since they change every 10 °C. For this reason and since the Boltzmann-Arrhenius expression has its foundation in statistical thermodynamics [65], we choose equation (12) to describe the temperature dependence of metabolic heat generation.

The final element on equation (12) is the basal metabolic rate that is both species and tissue specific [69]. First, we need to estimate the total amount of energy produced by the animal Q_{TOTAL} (W), which can be achieved from an allometric relationship developed by Roberts et al. [70],

(14) $$Q_{TOTAL} = 4.9m_m^{0.667}$$

valid for mammalian species where m_m is the mass (kg) of the mammal. Note that the statistical methods employed in this relationship used data gathered in thermoneutral conditions. For a 0.020 kg weight mouse the estimated energy is then 0.36 W.

In order to estimate the tissue specific M_0, it is critical to consider the highly metabolic organs even though they are not in the bladder region: liver, brain, kidneys and heart. This is especially relevant due to the high surface-area-to-volume ratio of mice. To estimate the tissue specific M_0, we use the allometric relationships developed by Wang *et al.* [69],

$$
\begin{aligned}
Q_{liver} &= 1.09 m_m^{0.60} \\
Q_{brain} &= 0.24 m_m^{0.62} \\
Q_{kidneys} &= 0.23 m_m^{0.77} \\
Q_{heart} &= 0.26 m_m^{0.86} \\
Q_{remaining} &= 1.36 m_m^{0.60}
\end{aligned}
\tag{15}
$$

However, Wang *et al.* [69] did not refine the data to thermoneutral conditions as implemented by Roberts et al. [70]. Thus, the tissue-specific M_0 is calculated using

$$M_{0,i} = \frac{Q_i}{V_i} \frac{Q_{TOTAL}}{Q_{liver} + Q_{brain} + Q_{kidneys} + Q_{heart} + Q_{remaining}} \tag{16}$$

where V_i is the volume of tissue i (Table 4.4).

Table 4.4 – Metabolic heat rate properties.

Tissue	M_0 (W/m^3)	M_A (W/m^3)	R_M
Skin	3003	2002	0.67
Body	5727	1734	0.30
Bladder wall	48011	32073	0.67
Uterus	52566	30600	0.58
Large intestine	76846	38134	0.50
Bone	5166	4181	0.81
Brain	99267	56600	0.57
Heart	204996	109254	0.53
Kidneys	150456	121469	0.81
Liver	170566	113943	0.67

As in blood perfusion, we are interested to account the effect of anesthesia on the metabolic heat rate. In normal tissues, energy metabolism and blood flow are tightly coupled through a variety of local auto-regulatory mechanisms. Under equilibrium conditions, regional rates of metabolism and tissue perfusion are highly correlated [71]. Thus, we define $R_M = R_\omega$ as the anesthesia induced change in mice's metabolic heat rate and establish the following relationship:

$$M_{Ai} = R_{Mi} M_{0i} \tag{17}$$

where M_A (W/m^3) is the metabolic heat rate after anesthesia, which is valid for steady state conditions. The values of M_A are presented in Table 4.4.

4.2.5.4. Effect of anesthesia and thermoregulation

Four different scenarios were chosen to access the combined effect of anesthesia and thermoregulation (ω_B and M temperature dependence) on the simulated temperature profile (see table 3). Under anesthesia, the coefficients ω_0 and M_0 in equations (10) and (12) are substituted by ω_A and M_A, respectively.

Table 4.5 – Scenarios to study anesthesia and thermoregulation effects on temperature simulations.

	Anesthesia	Blood flow rate (ω_B) and metabolic heat rate (M)
Case 1	Yes	Constant: $\omega_B = \omega_A$ and $M = M_A$
Case 2	Yes	Temperature dependent: $\omega_B(T)$ and $M(T)$
Case 3	No	Constant: $\omega_B = \omega_0$ and $M = M_0$
Case 4	No	Temperature dependent: $\omega_B(T)$ and $M(T)$

4.2.6. Fluid flow model

Fluid flow distribution inside water bolus is calculated by solving Navier-Stokes and mass continuity equations for an incompressible and Newtonian fluid given by [72],

$$\rho_i \frac{\partial \boldsymbol{u}_i}{\partial t}(\boldsymbol{r},t) + \rho_i \boldsymbol{u}_i(\boldsymbol{r},t)\cdot\nabla \boldsymbol{u}_i(\boldsymbol{r},t) = -\nabla p_i(\boldsymbol{r},t) + \mu_i(\boldsymbol{r},t)\nabla^2 \boldsymbol{u}_i(\boldsymbol{r},t) + \boldsymbol{F}_i(\boldsymbol{r},t) \quad (18)$$

$$\nabla\cdot\boldsymbol{u}_i(\boldsymbol{r},t) = 0 \quad (19)$$

In equations (18) and (19), $\boldsymbol{u}$ is the velocity vector (m/s), p is the pressure distribution (N/m^2), t is the time (s), μ is the material dynamic viscosity (kg/s/m) that is temperature dependent and $\boldsymbol{F}$ the volume force induced by gravity (N/m^3). Each term in equation (18) has the units of force per unit volume; the term $\partial\boldsymbol{u}/\partial$t represents the acceleration of the fluid, $\boldsymbol{u}\cdot\nabla\boldsymbol{u}$ the convective acceleration, ∇p the pressure gradient and $\mu\nabla^2\boldsymbol{u}$ the momentum losses due to viscosity. Equation (19) is a consequence of constant density, where $\nabla\cdot\boldsymbol{u}$ is the time rate of change of the volume of a moving fluid element, per unit volume.

The inlet flow velocity is measured experimentally (0.2 liter/min) and a laminar outflow is defined on the surface normal to the outlet side (Figure 4.3c). A no-slip boundary condition is applied on the walls that surround the bolus. This condition dictates that the velocity is equal to the null vector at the wall ($\boldsymbol{u}(\boldsymbol{r})|_{wall} = \boldsymbol{0}$) [72].

4.2.6.1. Heat transfer in fluids

Spatial distributions of fluid velocity (***u***) and calculated P_d are incorporated in thermal simulations. In fluid regions (water and urine), temperature is determined from

$$\rho_i C_{pi}\left(\frac{\partial T_i}{\partial t}(\boldsymbol{r},t)+\nabla\cdot\left(T_i(\boldsymbol{r},t)\boldsymbol{u}_i(\boldsymbol{r},t)\right)\right)=\nabla\cdot\left(k_i\nabla T_i(\boldsymbol{r},t)\right)+P_{di}(\boldsymbol{r}). \quad (20)$$

Each term in equation (20) has units of power per unit volume. Both equation (20) and bioheat equation (5) are derived from the classical heat equation. The additional term $\rho C_p \nabla\cdot(T\boldsymbol{u})$ represents the convective currents induced by temperature gradients.

At the inlet we impose the Dirichlet boundary condition $T(\boldsymbol{r},t)|_{inlet} = T_{bolus}$ while at the outlet we have a Neumann boundary condition $\boldsymbol{n}\cdot(\nabla T(\boldsymbol{r},t))|_{outlet} = 0$. At the wall we apply a convective cooling boundary condition described by equation (7) but without the radiation term and replacing k_{skin} by the thermal conductivity of antenna's copper k_{copper}. Finally, we assume continuity boundary conditions (temperature and heat flux) at the interface skin/antenna.

4.2.6.2. Dimensionless numbers

To determine the flow regime we use Reynolds number $Re = u_m D/v$ where v is the kinematic viscosity (m^2/s), u_m = 0.42 m/s is the mean fluid velocity over the tube cross section and D = 3.2 mm is the inlet tube diameter. The kinematic viscosity of water is temperature dependent (Figure 4.5) and within the range of bolus temperature used in this study ([33, 42] °C) the Reynolds number varies from 1782 to 2115. The laminar regime of a fully developed flow occurs when $Re < 2300$ [73] which is satisfied in the present study. We include a 10 cm tube in the inlet/outlet of the waveguide (Figure 4.3) to allow the fluid to fully develop.

The effect of viscous heating can be estimated using the Brinkman number: $Br = v\rho u_m^2/(k\Delta T)$. Using ΔT = 10 °C results $Br << 1$, thus viscous heating in the water-loaded waveguide is expected to be negligible [72]. In urine we also neglect the viscous heating since the characteristic velocity is smaller than the one in the water. In a similar manner, the Richardson number $Ri = g\,\beta\,\Delta T\,D/u_m^2$ presents the effect of natural *vs.* forced convection, where g = 9.8 m/s^2 is the gravitational acceleration, β the thermal expansion coefficient. For water $\beta = 2.76\times10^{-4}$ 1/K which leads to $Ri << 1$. This condition states that natural convection is negligible when compared to forced convection [72].

However, in urine it is difficult to estimate the velocity and thus any of the dimensionless numbers. Therefore, we incorporate the gravitation effect to account for possible natural convection currents.

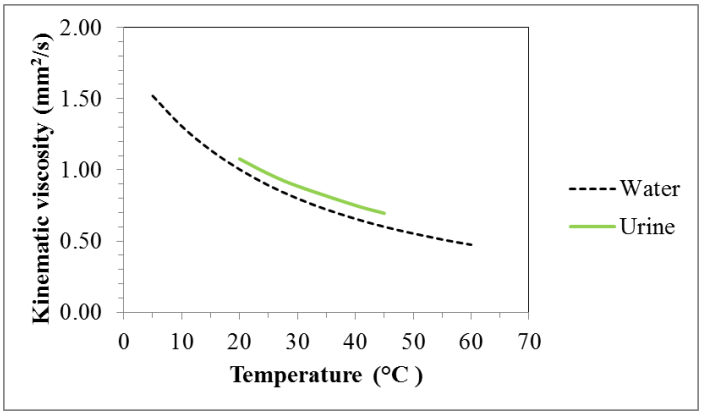

Figure 4.5 – Temperature dependency of the kinematic viscosity of water and urine [74].

4.2.7. Numerical considerations of the thermo-fluid model

We use COMSOL Multiphysics v4.2 (COMSOL, Palo Alto, CA) – a finite element software – to solve the combined bioheat transfer equation (5), Navier-Stokes equations (18)-(19) and the heat transfer equation (20) in fluids. These equations are integrated in time using an implicit linear multistep method (backward differentiation formula – BDF) coupled with a GMRES solver (generalized minimum residual solver) enhanced with a geometric multigrid pre-conditioner [75]. We use GMRES since it is more suitable for nonlinear problems but, as an iterative solver, it converges faster and more robustly if element quality is high [76, 77]. The element quality histogram is presented in Figure 4.6.

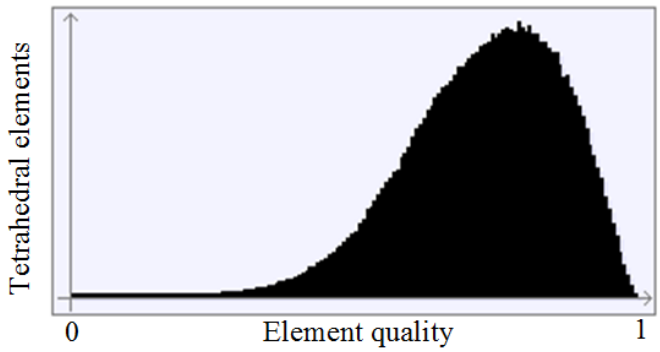

Figure 4.6 – Element quality histogram with a total of 634817 tetrahedral elements, where 0.0 represents a degenerated element and 1.0 represents a completely symmetric element.

The numerical solutions are computed in the mesh nodes with grid settings summarized in Table 4.6. Before computing the volume meshes, we add an extra fine mesh at the interface between the antenna and mouse to improve the numerical solution at this particular location that presents high temperature gradients. We also guarantee a sufficiently fine mesh across the thickness of all channels (inlet and outlet) using a minimum of 8 mesh elements. Further refinements do not change any of the variables under study and thus, a mesh-independent solution is achieved.

Table 4.6 – Grid settings for all objects in the thermo-fluid model.

Region	Tetrahedral elements	Maximum size (mm)	Maximum growth rate
Subcutaneous	20956	2.74	1.3
Body	350243	2.74	1.3
Bladder wall	39886	2.74	1.3
Uterus	38358	2.74	1.3
Large intestine	28719	2.74	1.3
Tail	23130	7.54	1.4
Brain	16211	2.74	1.3
Heart	4964	2.74	1.3
Kidneys	8169	2.74	1.3
Liver	16295	2.74	1.3
Urine	18781	2.74	1.3
Water bolus	69105	3.25	1.13
Interface mouse/antenna	467	1.41	1.08

4.2.8. Temperature initialization

COMSOL uses a Newton-type (GMRES) iterative method to solve nonlinear systems of partial differential equations (PDEs). This solution method is particularly sensitive to the initial estimate of the solution which implies having consistent initial solutions and boundary conditions. From the moment that anesthesia is induced, there are concurrent transient phenomena that contribute to the spatial temperature distribution. In fact, the mouse is being cooled due to the reduced metabolic activity induced by anesthesia. On the other hand, the mouse is being heated with a thermal pad to maintain its body

temperature. The thermal pad temperature T_{pad} helps dictate core temperature and thus, we assume that arterial temperature (T_a) in equation (9) is set to T_{pad}. This assumption is reinforced due to the high surface-area-to-volume ratio of mice and the high area being heated with the thermal pad.

A steady state simulation is performed using anesthesia induced changes in blood perfusion and metabolic rate. *SAR* is set to zero and the thermal pad heating is represented by a boundary condition that guarantees 38 °C in the mouse's back. The resulting steady state temperature $T_{ss}(\boldsymbol{r})$ will feed the transient simulation (T_t) as $T_t(\boldsymbol{r},0) = T_{ss}(\boldsymbol{r})$. This approach is valid assuming that once the experiment starts the body is in thermal equilibrium due to thermal pad heating and anesthesia-induced hypothermia. We expect that is the case since it takes around 30 min from the moment of anesthesia injection until microwave heating starts.

4.2.9. Temperature-based Optimization

A temperature-based optimization algorithm is formulated and integrated to the steady state multiphysics model to estimate the optimal applied power and bolus temperature. Our goal is to ensure that the bladder (our target) is heated efficiently in the therapeutic range [42, 43] °C ($T_{targetmin}$ = 42 °C and $T_{targetmax}$ = 43°C) while sparing the remaining tissues from high temperatures (<42 °C). These two requirements are concurrent since heating the bladder will heat forcibly its surroundings. The optimization algorithm establishes the optimal compromise between both requirements.

The final step is to define the inequality constraints: (1) the global maximum temperature is controlled to be below T_{cr} (defined previously in Table 4.3); (2) the temperature in non-target tissues is kept below the minimum therapeutic level ($T_{targetmin}$) to prevent overheating. The first constraint is more relevant since necrosis might occur above T_{cr}. Thus, we introduce weighting factors (w) in the objective function as follows:

$$
\begin{aligned}
J\left(P_{ant},T_{bolus}\right) = {} & w_1 \int\limits_{\substack{\boldsymbol{r}\in target \\ T_{target}<T_{targetmax}}} \left(T_{targetmax} - T_{target}\left(\boldsymbol{r};P_{ant},T_{bolus}\right)\right)^2 dV_{target} \\
& + w_2 \sum_{i=1}^{n-1} \int\limits_{\substack{\boldsymbol{r}\notin target \\ T_i>T_{targetmin}}} \left(T_i\left(\boldsymbol{r};P_{ant},T_{bolus}\right) - T_{targetmin}\right)^2 dV_i \\
& + w_3 \sum_{i=1}^{n} \int\limits_{\substack{\boldsymbol{r}\in V \\ T_i>T_{cr}}} \left(T_i\left(\boldsymbol{r};P_{ant},T_{bolus}\right) - T_{cr}\right)^2 dV_i
\end{aligned}
\qquad (21)
$$

where $w_1 = w_2 = 1$ and $w_3 = 1000$ to ensure the above requirements. The objective function J, defined as above, guarantees that large deviations from desired temperatures, *i.e.*, cold spots in the bladder and hot spots in healthy tissue, increase significantly the objective function. The objective function is evaluated in the entire 3D domain, where V is the volume defined by the full mouse object. This optimization strategy is based on two algorithms presented elsewhere [22, 78]. Both antenna power (P_{ant}) and bolus temperature (T_{bolus}) are input of the temperature-based optimization scheme, and the optimal pair (P_{ant}, T_{bolus}) is determined when J is minimum. This scheme improves the previous SAR-based optimization used to developed the microwave applicator [18]. For convenience we present the results in terms of the normalized goal function J_n ($0 \leq J_n \leq 1$) given by

$$J_n\left(P_{ant}, T_{bolus}\right) = \frac{J\left(P_{ant}, T_{bolus}\right)}{\max\left(J\left(P_{ant}, T_{bolus}\right)\right)} \tag{22}$$

4.3. Results

4.3.1. Experimental results

In vivo murine bladder hyperthermia studies are conducted to validate numerical results observed in simulation. As seen in the mouse 1 experiment (Figure 4.7), MW power (15W) is turned on at 5 minutes. The steady state region is reached around 13 minutes. In this region, the subcutaneous tissue is maintained around 40 ºC due to the cooling effects of 37 ºC water circulating inside the applicator. Tissues around the bladder (large intestine and uterus) are increased to [42, 43] ºC while the core body temperature is maintained around 38 ºC throughout the heating period due to the use of a thermal pad heater. The MW power is turned off at 18 minutes and the tissue temperature returns to normothermic conditions after 5 minutes. A similar procedure is used for the remaining 4 mice with minor variations in cooling bolus temperature, MW power level and heating start and stop times.

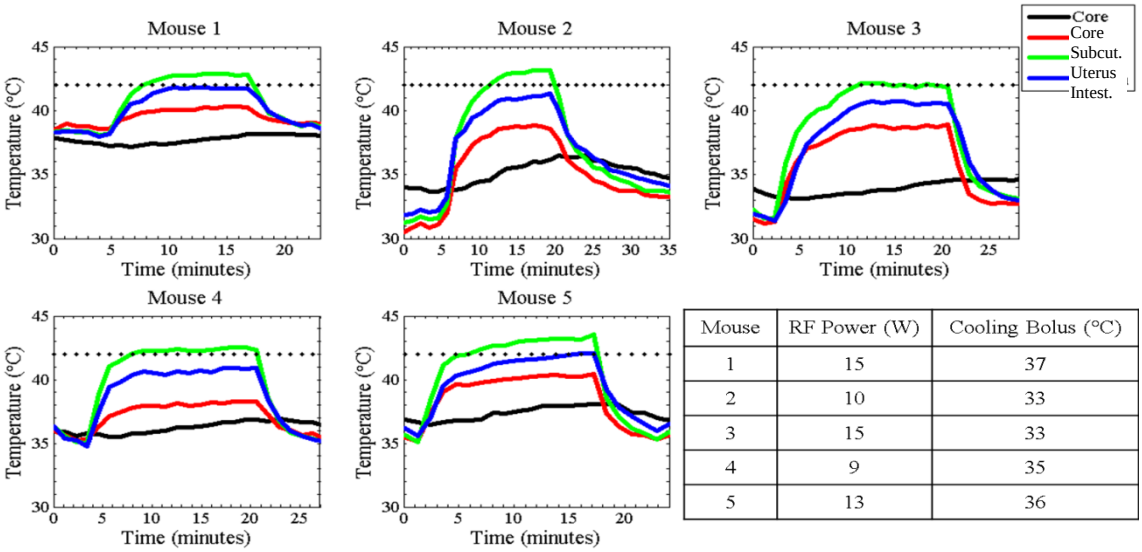

Mouse	RF Power (W)	Cooling Bolus (°C)
1	15	37
2	10	33
3	15	33
4	9	35
5	13	36

Figure 4.7 – Temperature data taken from five independent *in vivo* studies of murine bladder hyperthermia. Temperature increases when MW power is turned on (around [2, 5] minutes) and decreases when MW power is turned off (around [18, 20] minutes). The dotted line means 42˚C.

4.3.2. SAR model

SAR and S_{11} are measured in a muscle-equivalent liquid phantom and compared to numerical results. The simulated S_{11} is most accurate below 2.60 GHz (Figure 4.8) with a relative error ≤ 5 %. At 2.45 GHz S_{11} is approximately -20 dB, which means that 1% of power is reflected at the interface between the antenna and mouse.

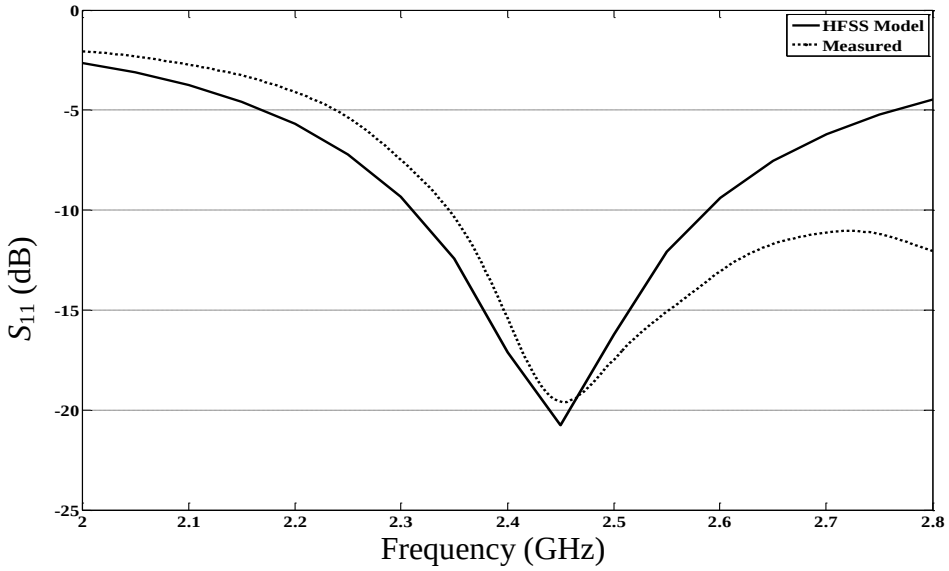

Figure 4.8 – S_{11} simulation results (HFSS) compared to measurements using an Agilent E5071C network analyzer.

Figure 4.9 shows that the SAR pattern simulated in HFSS matches well to the SAR data that are measured in muscle-equivalent phantom using an ***E***-field scanning probe. The ***E***-field probe contains three orthogonal dipoles centered 3 mm from the tip; therefore, SAR patterns are recorded with the closest measurements of 3 mm from the antenna front face (Figure 4.9c). The error between the simulated and measured SAR does not exceed 10%. Applying a moving average to the simulated data suggests that errors in the side lobe regions may be due to the fact that the diameter of the electric field probe used for SAR measurement is 70% as large as the waveguide aperture.

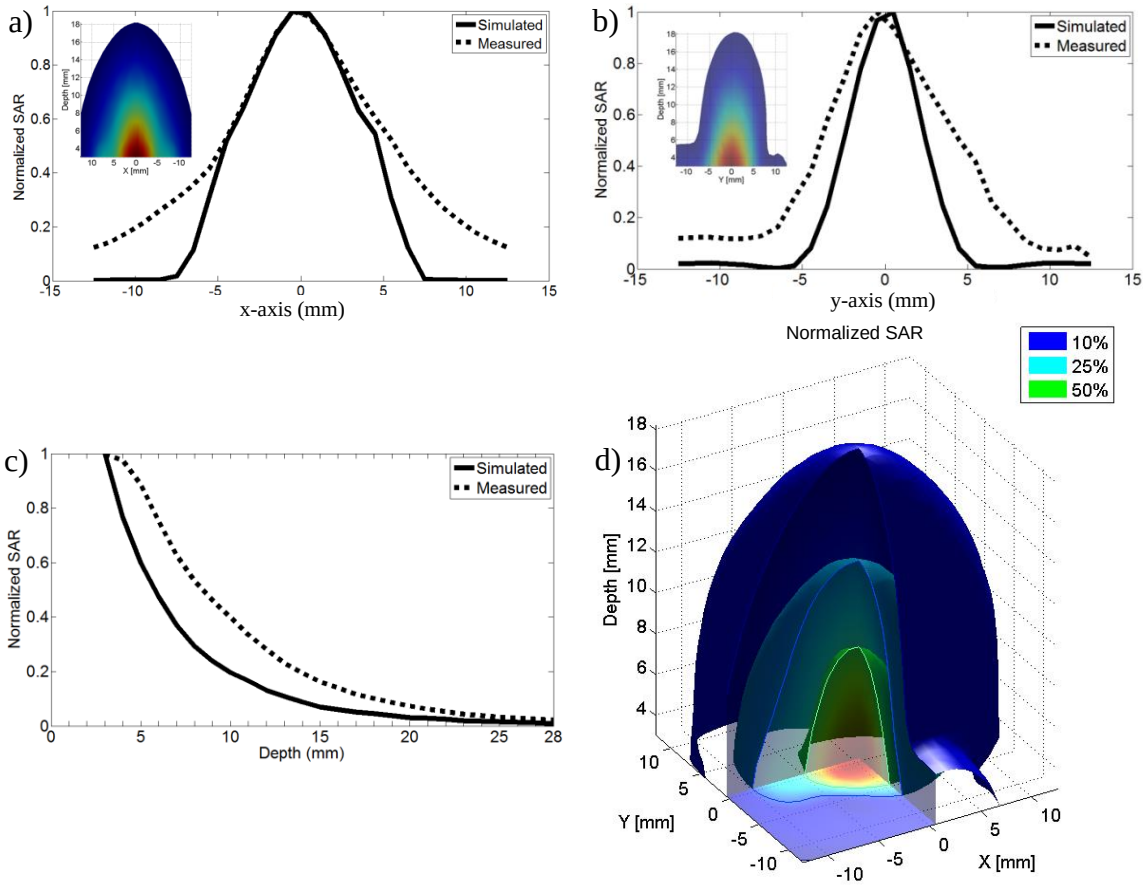

Figure 4.9 – SAR simulated with HFSS compared to measurements with all values normalized to the maximum value at 3 mm depth: a) profile across x-axis, b) profile across y-axis, c) depth profile; d) 3D SAR measurements in muscle phantom.

Simulations of power loss density $P_d = \rho SAR$ in the mouse model (Figure 4.10) indicate that maximum power deposition occurs in the skin and subcutaneous tissue directly above the bladder. The temperature of skin and subcutaneous tissue can be lowered by circulating appropriate temperature water through the applicator. Figure 4.10 also shows that the waveguide is able to deposit energy at depth in the bladder region as intended.

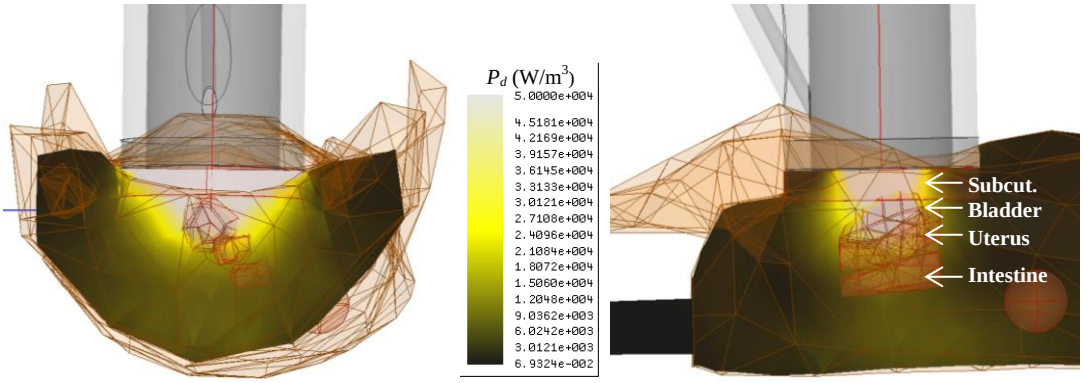

Figure 4.10 – HFSS P_d (W/m^3) simulation in mouse model: a) x-axis profile; b) y-axis profile.

4.3.3. Bioheat transfer model

4.3.3.1. Mice temperature initialization

Experimental results from mouse 1 (Figure 4.7) are used to initialize temperature in the mouse's body for the transient simulation. We first simulate the steady state temperature in the mouse (see equation (5)) for three distinct cases: mouse in thermoneutral conditions T_a = 38 °C (Figure 4.11a); mouse under pentobarbital anesthesia considering T_a = 30 °C to account for a 8 °C temperature drop [24] due to anesthesia (Figure 4.11b); and mouse under anesthesia but being heated by a thermal pad (T_{pad}) at 38 °C, thus warming the blood that circulates through the body at T_a = 38 °C (Figure 4.11c). The latter steady state solution $T_{ss}(\boldsymbol{r})$ is taken as the initial temperature for the transient simulation $T_t(\boldsymbol{r}, t)$ leading to $T_t(\boldsymbol{r}, 0) = T_{ss}(\boldsymbol{r})$.

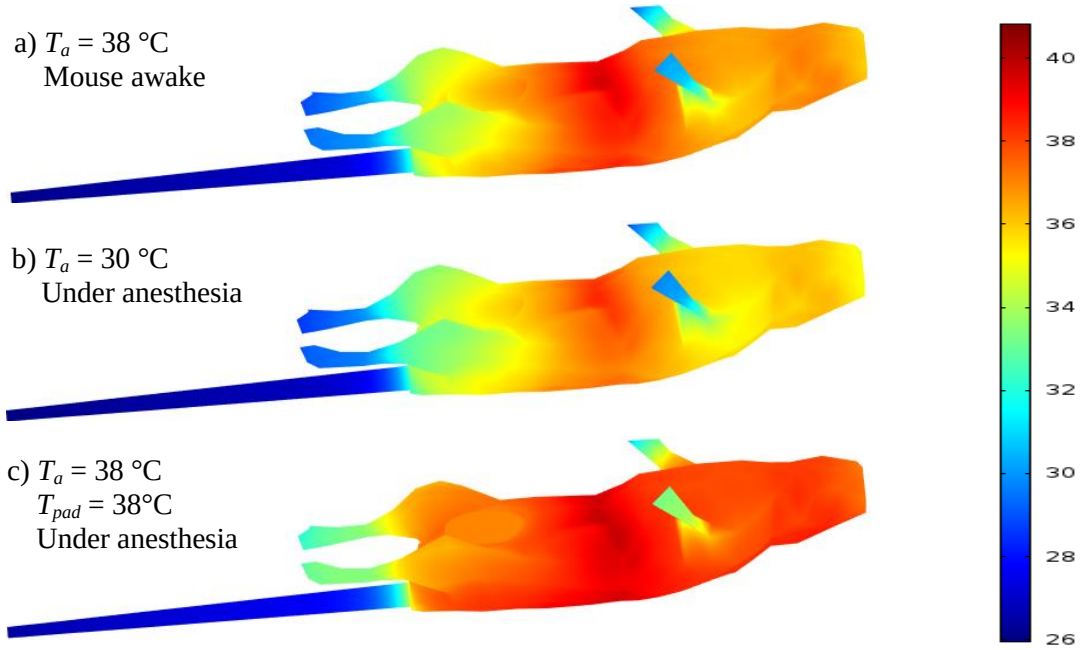

Figure 4.11 – 3D steady state temperature distribution in mouse under: a) thermoneutral conditions, b) anesthesia-induced hypothermia and c) anesthesia plus thermal pad heating.

4.3.3.2. Transient temperature results

The numerical studies are implemented to mimic, as closely as possible, experiment shown in Figure 4.7, where P_{ant} = 15 W and T_{bolus} = 37°C. The probes are inserted into the mouse with some degree of uncertainty (order of mm) associated with its placement. In order to compare numerical results with experimental ones, we choose to present the minimum, average and maximum temperatures in the target regions of the subcutaneous tissue, uterus and large intestine. This is considered to ensure that we cover the probe location in our simulations. The target region of each organ is located within a cylinder of the diameter of the antenna and extending down under the antenna. From Figure 4.12 we can observe that there is a good agreement between experimental and simulated temperatures. Note that temperatures in the subcutaneous tissue and outside the heating period are not predicted under the simulated range defined by the minimum and maximum temperature. However, in the uterus and intestine the experimental and simulated temperature agree outside this heating period. Furthermore, in all cases simulated and experimental temperatures agree during microwave heating.

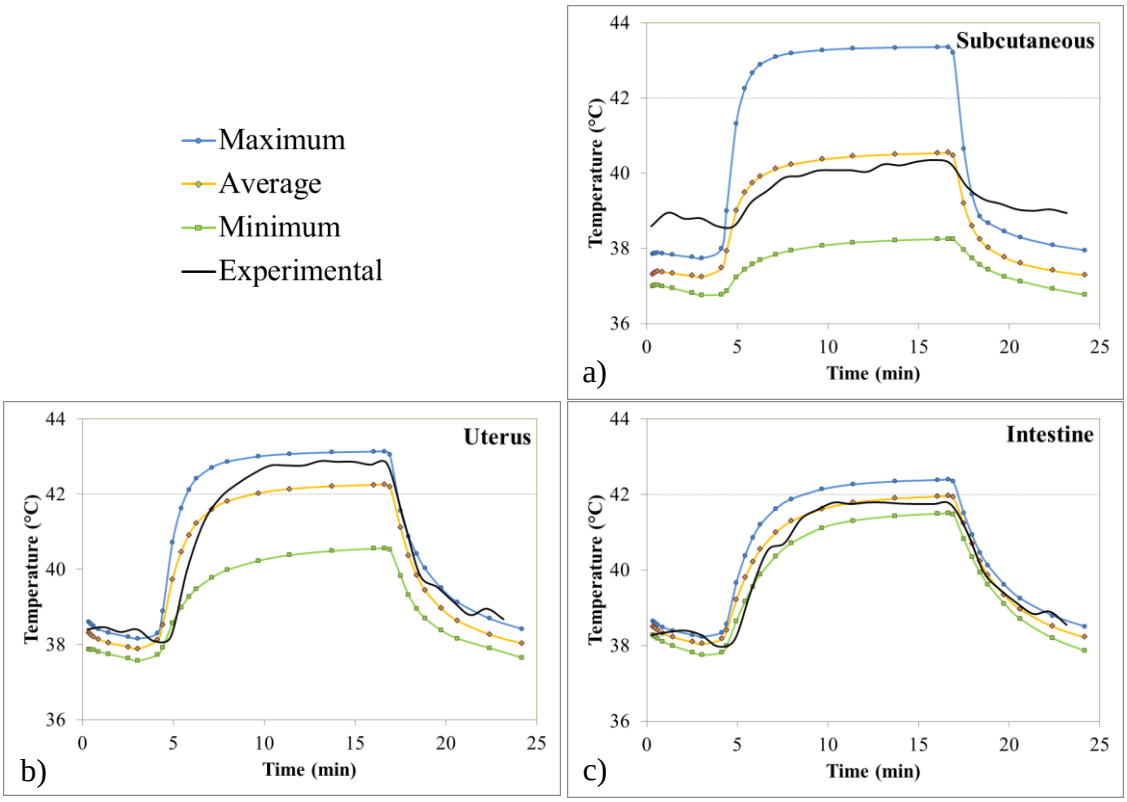

Figure 4.12 – Transient simulations in the anesthetized mouse *vs.* experimental data using P_{ant} = 15 W, T_{bolus} = 37 °C and T_{pad} = 38 °C: a) subcutaneous tissue, b) uterus and c) large intestine.

4.3.3.3. Relative temperature simulations

To study the relative heating of all target regions directly under the antenna, the corresponding average temperatures are presented in Figure 4.13. During microwave heating the uterus and intestine are [0.8, 1.0] °C and [1.1, 1.7] °C, respectively, below the average temperature of the bladder. The difference between bladder and uterus average temperatures is almost constant during heating period. Thus, uterus can be a good surrogate for bladder temperature with $T_{bladder} = T_{uterus} + 0.9$ during microwave heating.

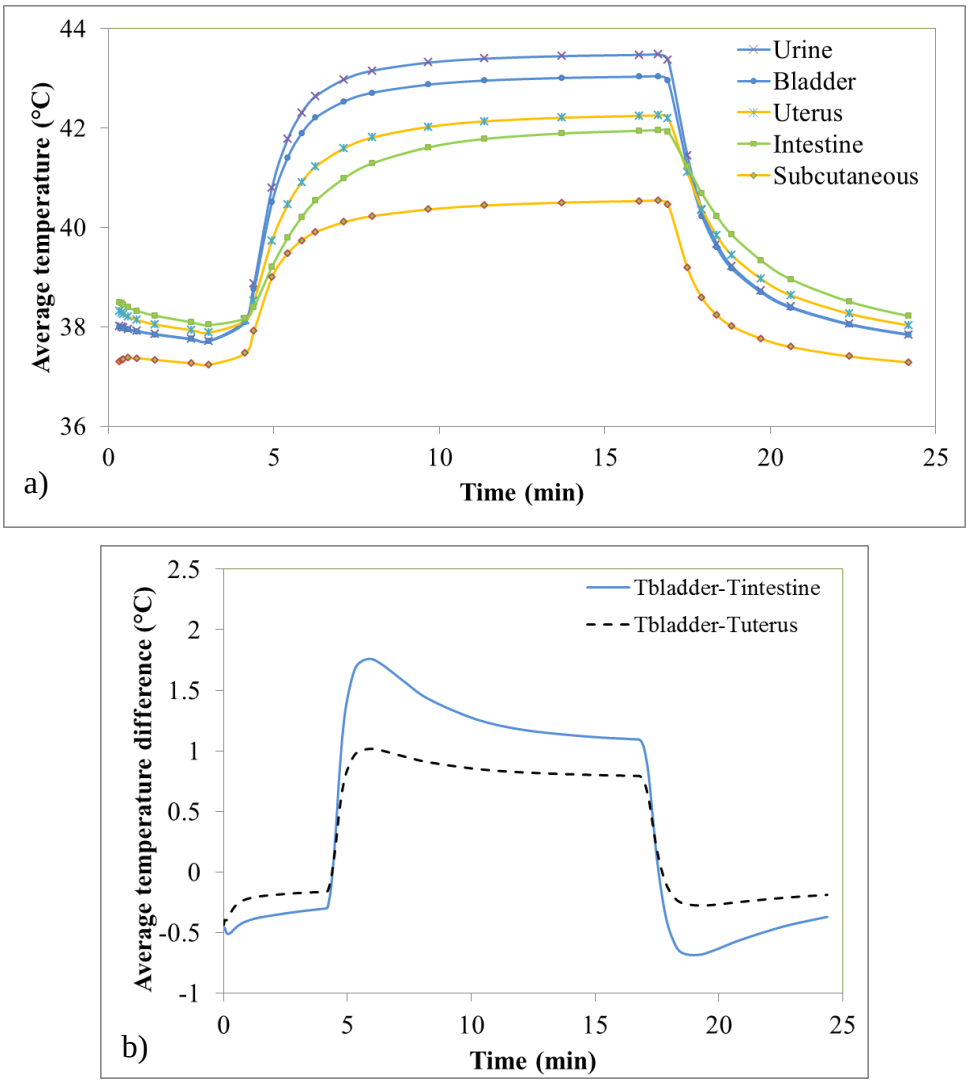

Figure 4.13 – Transient simulations in the anesthetized mouse using P_{ant} = 15 W, T_{bolus} = 37 °C and T_{pad} = 38 °C: a) average temperatures for different target regions and b) difference between average temperatures of bladder and intestine as well as bladder and uterus to determine the best bladder surrogate.

4.3.3.4. Effect of anesthesia and thermoregulation

The temperature volume histogram for bladder is presented in Figure 4.14 for the case studies introduced in Table 4.5. We choose the bladder since it is our target organ. Simulations were performed under the same conditions as shown in Figure 4.12 (P_{ant} = 15 W and T_{bolus} = 37°C), which corresponds to Case 2 in Table 4.5. Case 2 shows that the temperature in the bladder region is in the intended range [41.5, 43.8] °C. The remaining cases explore variable blood flow rates (equations (10) and (11)) and metabolic heat rates (equations (12) and (17)) dependencies. One can observe a shift in temperature to the right (Case 1) and to the left (Cases 3 and 4) when comparing to Case 2. This shows a significant influence of anesthesia and thermoregulation on bladder temperature distributions.

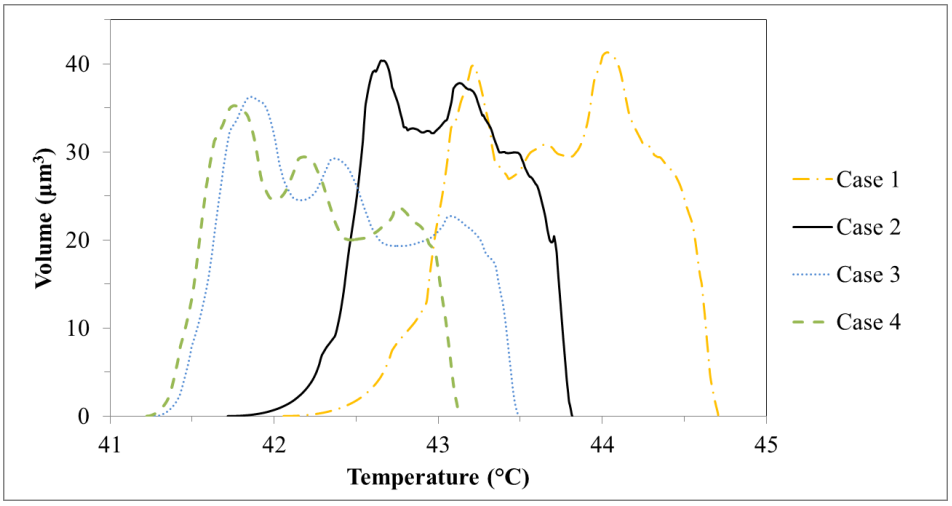

Figure 4.14 – Temperature volume histograms in the mouse's bladder at t = 16.3 min: effect of temperature dependence and anesthesia on blood perfusion (ω_B) and metabolic heat rate (M).

Figure 4.15 presents the transient behavior for Cases 1, 3 and 4 in the uterus and large intestine. The transient profile of the nominal Case 2 is already shown in Figure 4.12. We can observe that not accounting for thermoregulation and anesthesia effects, the proper transient behavior during experiment cannot be captured. In particular, Case 1 does not establish a steady state as seen in experiment or the nominal Case 2 (Figure 4.12). The remaining Cases 3 and 4 result in inaccurate predictions where all simulated temperature values are below than those of experiment during the heating period.

a) Case 1: constant $\omega_B = \omega_A$ and $M = M_A$ with mouse under anesthesia.

b) Case 3: constant $\omega_B = \omega_0$ and $M = M_0$ with mouse awake.

c) Case 4: ω_B and M temperature dependent with mouse awake.

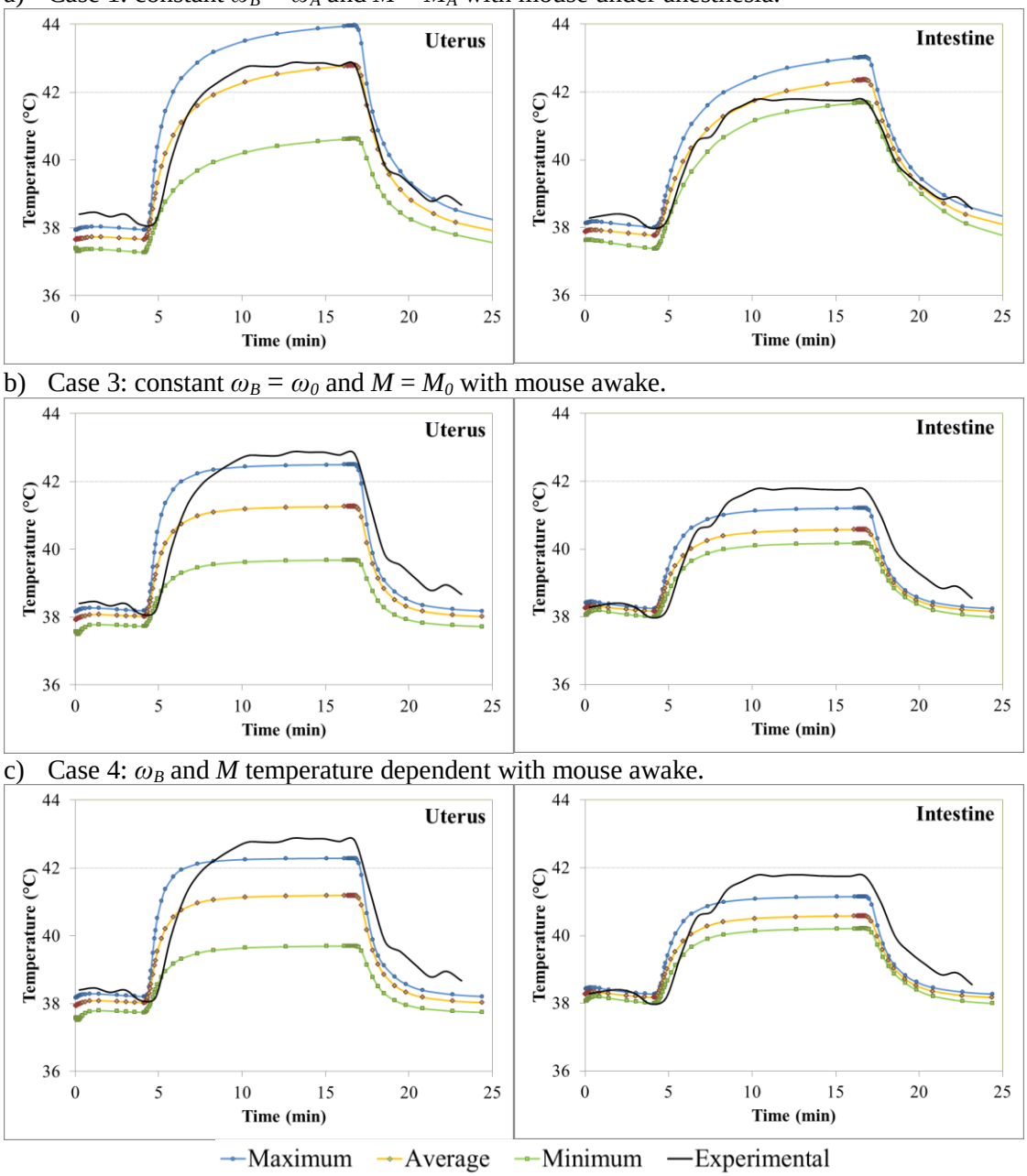

Figure 4.15 – Effect of anesthesia and thermoregulation on the transient temperature simulations. Experimental data for mouse 1 with P_{ant} = 15 W, T_{bolus} = 37 °C and T_{pad} = 38 °C.

4.3.3.5. Effect of water bolus

Figure 4.16 presents the effect of the water bolus temperature (T_{bolus}) on the temperature profile over the heating region. One can observe that as T_{bolus} decreases the hot spot moves towards the bladder region. This shows the relevance of developing an optimization algorithm to choose the optimal T_{bolus} and P_{ant} combination to focus heating in the bladder.

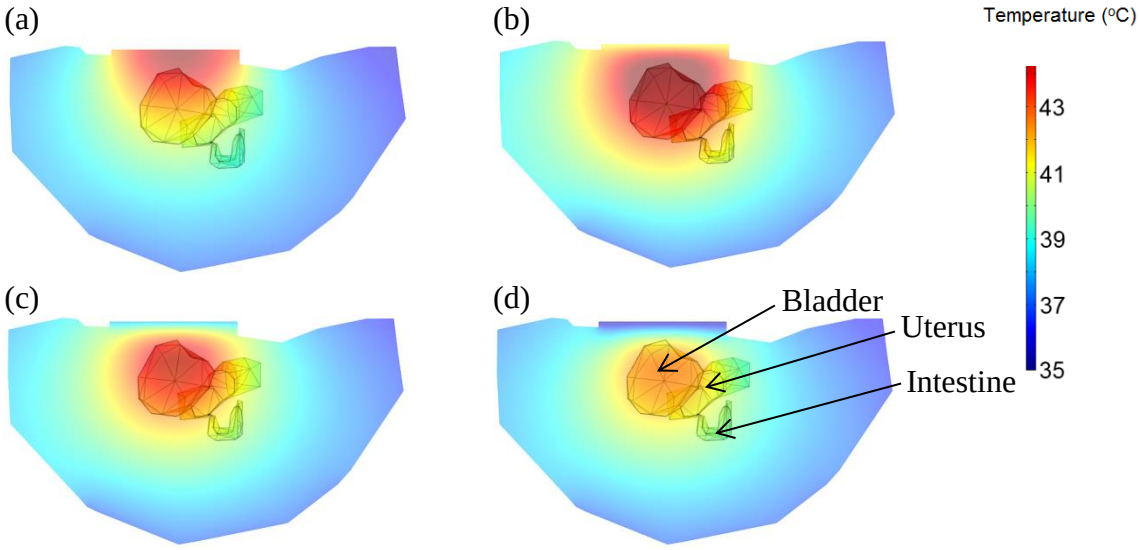

Figure 4.16 – 2D slice temperature profiles in mouse body, bladder, uterus and large intestine with no water circulation (a) and with bolus temperature constant at 41 °C (b), 38 °C (c) and 35 °C (d). MW power is set at 5 W (a) and (b), (c), (d) at 12 W.

4.3.4. Optimization results

The simulation-based optimization studies are shown in Figure 4.17. The profile of each curve (J_n vs T_{bolus}) assumes a parabolic shape and the optimal value is taken where the minimum occurs. It is interesting to notice that changing the antenna power leads to a similar parabolic curve but shifted on the x-axis. Furthermore, the goal function J_n does not change significantly (0.05 ± 0.02, see Table 4.7) among the minimum values for each curve. For this reason, we plot the pairs (P_{ant}, T_{bolus}) for each minimum and a linear relationship is found between the two quantities (Figure 4.18). This relationship is given by $P^*_{ant} = -2.81T^*_{bolus} + 3.70$, where the asterisk stands for dimensionless quantities: $P^*_{ant} = P_{ant}/P_{ave}$ and $T^*_{bolus} = T_{bolus}/T_a$, where $P_{ave} = 13.5$ W is the average power in the analyzed range.

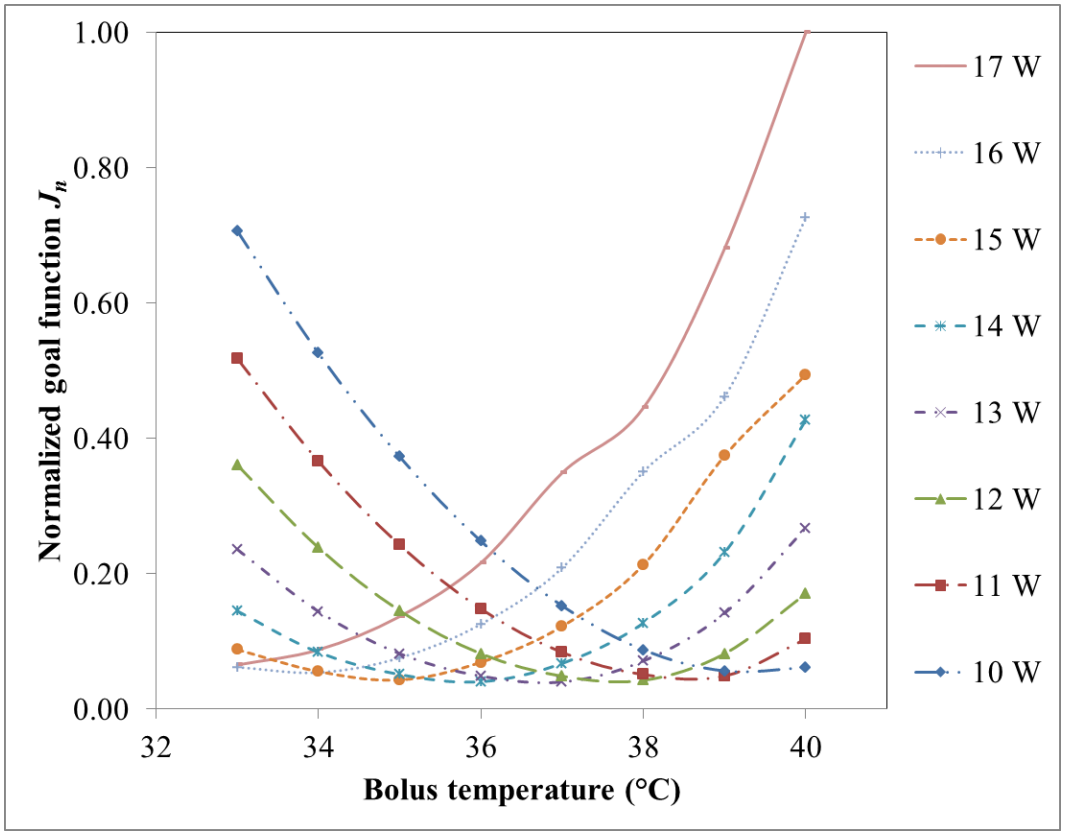

Figure 4.17 – Optimization results using parametric variations of the antenna power (P_{ant}) and bolus temperature (T_{bolus}).

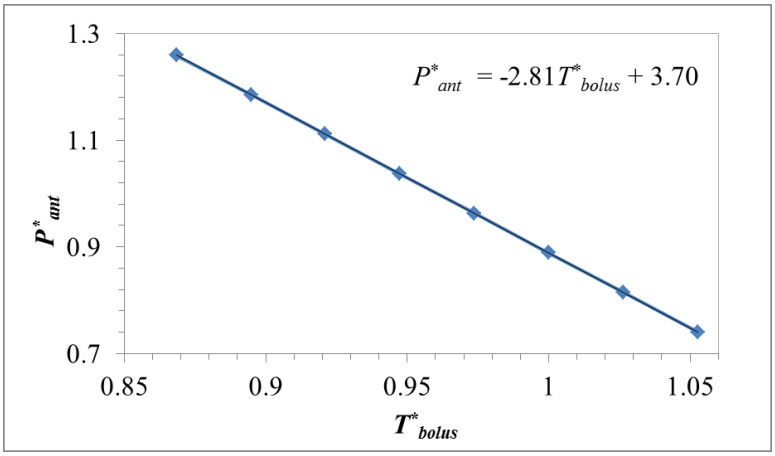

Figure 4.18 – Linear relationship obtained here $P^*_{ant} = -2.81T^*_{bolus} + 3.70$ that allows optimized results for focused bladder heating.

Table 4.7 shows in detail the goal function values for each optimized parametric pair and the correspondent average bladder and maximum subcutaneous temperatures. These quantities are critical parameters implicit to the optimization algorithm (equation (21)). These results are obtained using equation (21) with $T_{targetmin}$ = 42 °C, $T_{targetmax}$ = 43 °C

and T_{cr} = 45 °C. Note that we also present the simulated values of these parameters for the mouse 1 experimental settings P_{ant} = 15 W and T_{bolus} = 37 °C.

Table 4.7 – Minimum goal function for the optimized parametric pairs (P_{ant}, T_{bolus}) and correspondent average bladder and maximum subcutaneous temperatures.

P_{ant} (W)	T_{bolus} (°C)	Minimum J_n	Average $T_{bladder}$ (°C)	Maximum $T_{subcutaneous}$ (°C)
10	40	0.061	42.28	43.03
11	39	0.049	42.30	42.93
12	38	0.043	42.30	42.81
13	37	0.040	42.29	42.68
14	36	0.041	42.27	42.54
15	35	0.043	42.24	42.39
16	34	0.054	42.45	42.44
17	33	0.065	42.43	42.29
15	**37**	**0.120**	**42.96**	**43.41**

4.4. Discussion and future work

A multiphysics model based on numerical techniques is developed using tissue specific data to facilitate the creation of an accurate therapy planning for prediction of temperature. Although the proposed model is based on an existing microwave applicator, it contributes with unique aspects. This model accounts for the dynamics of biological properties that depend on temperature – $\omega_B(T)$, $M(T)$ – as well as anesthesia. Blood perfusion temperature dependence takes into account the duration of heating and the basal values of M_0 provide a realistic total power contribution from metabolism. Altogether, we have created a comprehensive multiphysics model that predicts optimal settings for a MW heating system that produces localized heating of a deep-seated target: murine bladder.

The CAD model is developed for a female C57BL/6 mouse (20 g weight, 11 weeks old) but it can be adjusted for different ages/weights by scaling the CAD model up or down. As mentioned, the CAD model accounts for the presence of bone in the tail. In the remaining regions bone is not visible in the segmented microMR and the pelvic bones are far from the heated region. From these reasons bone is not segmented. X-ray

microtomography images should be considered for future treatment planning studies where bones are in proximity to the treatment region.

In the microwave heating experiment (Figure 4.7) the bladder is healthy, *i.e.*, without tumor. Our goal is to prove the efficiency of the microwave applicator and multiphysics model. Once moving to experiments with tumors, we also have to accurately segmentate the tumor anatomy and include its specific properties in the virtual model.

As seen in Figure 4.7, temperature profiles induced by the bladder hyperthermia treatment look similar in all five mice. In this model, we assume that the mouse is at an initial thermal equilibrium. This happens in the mouse 1 experiment which is used as a case study in our numerical model. The organs temperatures of mice 2 and 3 begin at the initial time (t = 0 min) are approximately 31 °C. This temperature is expected for mice under anesthesia and without any external heating device [24, 25]. The initial organs' temperature of mice 4 and 5 are 36 °C and in the following [1, 3] min the temperature is still decreasing. These differences might be related to either the inherent irregularity of mice core temperature throughout the day (dependent on environmental conditions, age and even induced stress from manipulation) [59] or some different timing in the thermal pad heating procedure. We anticipate that the anesthetized mouse can reach a thermal equilibrium in thermoneutral conditions ([37, 38] °C) using a standard therapy protocol. The different initial temperature conditions may be the reason for differences in the amount of MW power and temperature of cooling bolus used to heat the bladder at [42, 43] °C.

Measured S_{11} of the prototype applicator matches the simulated S_{11} within 5% at 2.45 GHz (Figure 4.8). The small difference may be explained by the convergence criteria used in simulation; convergence is achieved when a maximum change of 5% in the S_{11} parameter is found between two consecutive adaptive mesh steps. At frequencies above 2.60 GHz the error is >5% due to the fact that we use a dispersive model for the different tissues and convergence of S_{11} is only required at the frequency of interest (2.45 GHz).

Simulated and measured *SAR* values reveal the same pattern of power deposition in muscle-equivalent liquid (Figure 4.9). The highest difference between simulated and measured SAR is apparent in the side lobe regions, likely due to the diameter of the electric field probe used to measure SAR. However, measurements confirm (Figure 4.7)

that the cooling water eliminates temperature rise in tissues superficial to the bladder and thus negates any deleterious effect that side lobes would have. The cooling effect becomes especially relevant since maximum power deposition occurs in the skin and subcutaneous tissue directly above the bladder (Figure 4.10).

Figure 4.11 shows the initialization of body temperature used in the transient simulation. In thermoneutral conditions the difference between surface temperature $T_{surface}$ and core temperature T_{core} is expected to be T_{core} - $T_{surface} \leq 1.0$°C [70]. Core temperature is determined based on the volume average temperature of all organs giving T_{core} = 37.9 °C. Skin temperature is calculated based on the average temperature over all skin surface except the tail surface, leading to $T_{surface}$ = 36.9 °C. The difference T_{core} - $T_{surface}$ is then in the experimental expected range. Regarding to surface tail average temperature, we obtain T_{tail} = 27.3 °C, which is significantly lower than $T_{surface}$. This difference is in accordance with the thermoregulatory function of the tail which serves as a heat-loss organ [79].

The experimental results are in agreement with temperatures observed in each organ (Figure 4.12), especially during heating period. Outside the period of heating, our model does not capture the correct temperature in subcutaneous tissue. We suspect that this is due to difficulties associated with ascertaining the exact location of the probe. This becomes even more relevant when very high temperature gradients occur as in the case of subcutaneous tissue (Figures 4.12 and 4.16). Even so, the model captures the transient temperature behavior of the critical organs: uterus and large intestine. We expect that the experimental temperature should be between the simulated average and maximum temperatures, due to the direction of heat flow (from the pelvis to the back) and the location of the probes that is centered with the antenna. This is the case of the uterus whereas in the large intestine the experimental temperature follows the simulated average temperature. The good agreement between the proposed multiphysics model and experimental results demonstrates that this model is useful in predicting internal tissue temperatures during murine hyperthermia studies.

From numerical simulations, we can show that the results mentioned above (Figure 4.12) do not change even if fluid dynamics is not considered into the urine region. This indicates that both natural convection and viscous heating do not contribute to the heat transfer in the bladder region. This is valid for a bladder volume of 0.15 ml. Note that the bladder volume can be controlled experimentally by extracting all the urine and

injecting a saline fluid with fixed volume and similar properties to urine. Thus, among different mice with similar weights the contribution of both natural convection and viscous heating remains negligible. The developed multiphysics method can be used for bigger bladder volumes. However, the conclusions regarding natural convection and viscous heating require further studies.

Figure 4.13a shows average temperatures simulated in the organs bladder, uterus, intestine, subcutaneous tissue as well as in the urine region. Urine temperature follows closely the bladder temperature. Urine is expected to be at a higher temperature since it does not include the heat sink associated with blood perfusion that removes heat. The average temperature difference between uterus and bladder (Figure 4.13b) is fairly constant during the heating period ($\pm$ 0.1 °C). These results further indicate that the uterus is an appropriate surrogate to monitor bladder temperature during hyperthermia treatments.

As far as we know, no previous studies addressed the thermal effects induced by anesthesia and thermoregulation. The latter is addressed by proper temperature dependence of biological properties: blood perfusion $\omega_B(T)$ and metabolic heat rate $M(T)$. We propose improved constitutive relationships for these properties. The relationship for $\omega_B(T)$ takes into account not only temperature but also the time of heating since blood perfusion is dependent on both variables. The relationship for metabolism is based on the Boltzmann-Arrhenius law. Furthermore, the basal values of M_0 provide a realistic total power contribution from metabolism. Moreover, both relationships for $\omega_B(T)$ and $M(T)$ take into account tissue-specific properties.

Figure 4.14 shows the temperature volume histograms (TVH) in the bladder for four distinct cases to address both thermal effects. It is readily seen that at t = 16.3 min, which corresponds to a steady state region, the bladder temperature is in the interval [41.5, 43.8] °C for the nominal Case 2. Considering anesthesia effects and constant biological properties (Case 1, ω_A and M_A), the TVH in the bladder shifts to the right towards higher temperatures as compared to Case 2. Both $\omega_B(T)$ and $M(T)$ increase since temperature increases during heating. Blood perfusion acts as a heat sink whereas metabolism acts as a heat source. This is clearly shown in the next figure (Figure 4.19) where we observe the power density defined by ρSAR, $M(T)$, M_A, $\omega_B(T)C_{p,b}(T_a\text{-}T)$ and $\omega_A C_{p,b}(T_a\text{-}T)$, which are integrated over the bladder volume and shown as a function of time. We add the power contribution from ρSAR to act as a reference for the heating

period. One can observe that the power difference associated with $\omega_B(T)$ and ω_A is much higher than the power difference associated with $M(T)$ and M_A. Since blood perfusion is a heat sink and metabolism a heat source, by decreasing the heat sink as in Case 1, temperature has to increase when compared with Case 2.

In Cases 3 and 4 (Figure 4.14) anesthesia is not taken into account. This implies that biological properties (ω_B and M) are not affected by the coefficients $R_\omega = R_M$ (equations (11) and (17)). When comparing with Case 2, the biological properties in Cases 3 and 4 are higher by the same factor ($1/R_\omega = 1/R_M$). Thus, the relative contribution of blood perfusion and metabolism (Figure 4.19) to the overall heat balance remains the same, *i.e.*, the heat sink dominates. Thus, by not accounting anesthesia, the TVH is shifted to the left towards lower temperatures as compared to Case 2 (Figure 4.14). Note that Cases 1 and 2 (under anesthesia) have a higher temperature differential than Cases 3 and 4 (mouse awake). This is a reflection of the more effective thermoregulation while the mouse is awake, in other words, under anesthesia thermoregulation is impaired as expected.

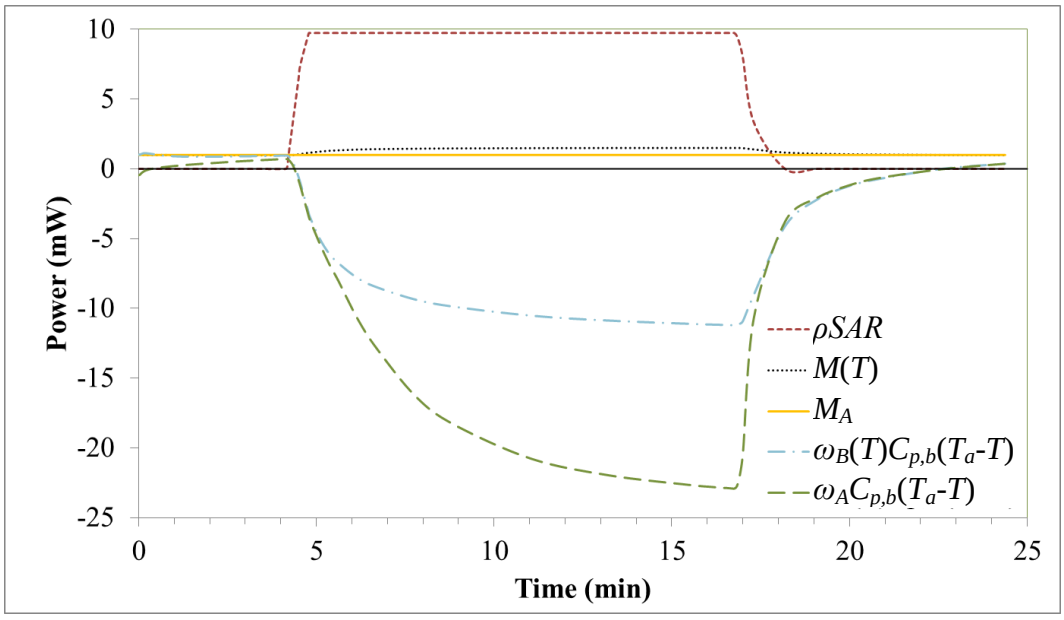

Figure 4.19 – Power contribution from ρSAR, $M(T)$, M_A, $\omega_B(T)C_{p,b}(T_a\text{-}T)$ and $\omega_A C_{p,b}(T_a\text{-}T)$ in the bladder during microwave heating as a function of time. The simulations assume the mouse under anesthesia.

The values in Figure 4.14 with the mouse awake are only presented with the intention to show the importance of using accurate biological data. These simulations with the

mouse awake have no physical parallel: while awake, mice would not have impaired behavioral thermoregulation and stress would contribute to increase core temperature. Moreover, the insertion of probes would necessarily induce pain in the mouse.

Figure 4.16 shows 2D slices in the critical region for different water bolus conditions. In particular, Figure 4.16a shows a hot spot in the surface skin due to the absence of the bolus cooling effect. The hot spot in the skin is in accordance with the higher power deposition at this particular location (Figure 4.10). The effect of different input temperatures in the water bolus is clearly visible as temperature reduces from 41 °C to 35 °C: the hot spot moves towards the bladder thus increasing the treatment efficiency. Note that after the experimental hyperthermia treatments, visual inspection of the mouse skin directly under the applicator reveals no burnings which agrees with the low surface temperatures obtained from numerical results (Figures 4.14 and 4.16).

The main goal of any hyperthermia treatment planning is to deliver heat efficiently to the target while sparing the non-target regions. This goal is achieved mathematically by equation (21) with results shown in Figure 4.17. We find that for the presented setup, there exist not one but several possible combinations of the two parameters (P_{ant}, T_{bolus}) that lead to optimized results with objective function $J_n = 0.05 \pm 0.02$. This explains why different combinations of P_{ant} and T_{bolus} – as verified experimentally (see Figure 4.7) – result in similar heating patterns. This leads to the possibility of developing a versatile heating procedure where choosing one parameter, P^*_{ant} or T^*_{bolus}, the other one is obtained from the relationship found here given by $P^*_{ant} = -2.81T^*_{bolus} + 3.70$ (Figure 4.18). Similar relationships should be found for mice with different weights using the same mathematical method.

Among the simulated results, the best pair is P_{ant} = 13 W and T_{bolus} = 37 °C (J_n = 0.04, Table 4.7). This pair is similar to the one used in mouse 1 experiment: P_{ant} = 15 W and T_{bolus} = 37 °C. Figure 4.20, presented below, shows that the bladder temperature obtained with the optimized parameters (13 W, 37 °C) has a significant difference of 0.5 °C when compared to the pair (15 W, 37°C): [41.5, 43.3] °C *vs.* [42.0, 43.8] °C, respectively. The same shift in maximum temperature occurs in subcutaneous tissue: 42.8°C (blue curve) *vs.* 43.3°C (red curve). This is especially relevant since the optimized temperature ranges for the pair (13 W, 37 °C) are more suitable for treatments with mitomycin-C or thermosensitive liposomes.

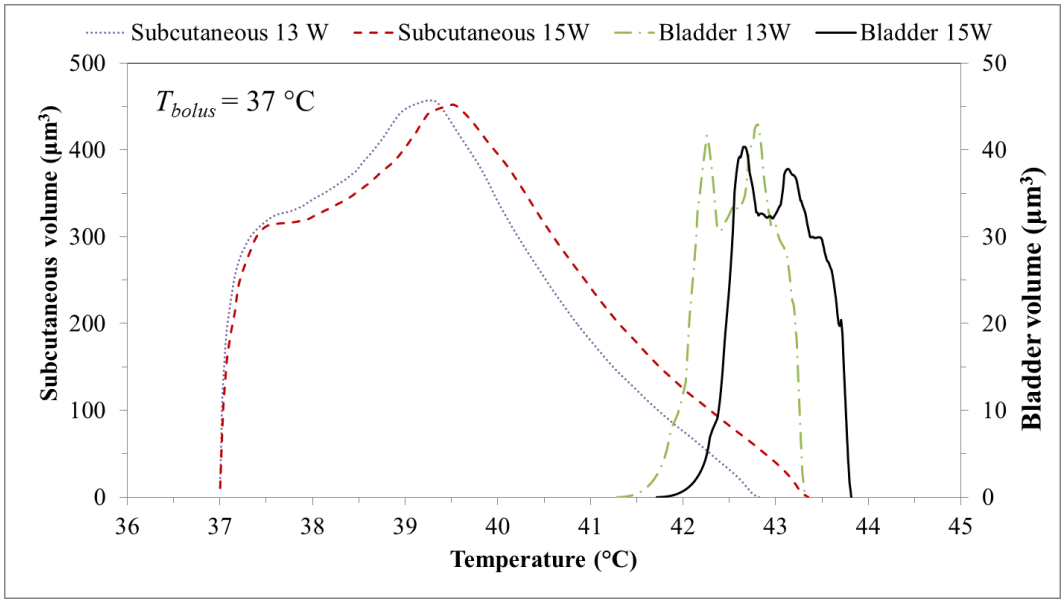

Figure 4.20 – Temperature volume histograms in the mouse's bladder and subcutaneous tissue at t = 16.3 min: optimized by the pair P_{ant} = 13 W and T_{bolus} = 37 °C *vs.* experimental nominal pair used in the numerical scheme validation P_{ant} = 15 W and T_{bolus} = 37 °C.

4.4.1. Future studies

At this moment we only test the multiphysics model for one case study. Further simulations will be required to validate the consistency of this model. However, there are several conclusions obtained in this work that should be accounted in future experiments. The first one is the need to establish a standard experimental procedure to guarantee that the mouse is at thermal equilibrium when the heating is turned on. This implies that the thermal pad temperature imposes arterial temperature, *i.e.*, $T_a = T_{pad}$ as we assumed in our model. With standardized initial conditions and $T_a = T_{pad}$, we predict that the optimal pair (P_{ant}, T_{bolus}) will remain the same. As seen in Figure 4.7, mice 2 and 3 are not in thermal equilibrium and thus the heating procedure had to be adjusted.

A control study to evaluate the transient decrease of temperature due to anesthesia is planned to occur in the near future. To perform this control study we will need to measure core temperature without the other stimuli provided by the microwave applicator and thermal pad heater. Such study will allow to calibrate the coefficients R_ω and R_M (equations (11) and (17)) to realistic time dependent functions. Thus, heating will be available to start at any time after administrating anesthesia since the multiphysics model will take the transient decrease effects of anesthesia into consideration.

Another key point will be related with the probe location, especially the invasive one. The precise location of the probe will be properly assessed with controlled penetration distances. This task will be supported with microMR images from the mouse. Furthermore, controlling the distance over the vagina and rectum will lead to a more precise location in the intestine and uterus. Other probes in the skin, tail and pelvis surface will be important to evaluate the boundary conditions performance.

In these studies, water bolus temperature is only measured at the input port. In future studies, measuring both the temperature at the input and output of the waveguide as well as at the interface antenna/skin, will be useful to validate the electro-thermo-fluid model inside the waveguide.

In this work we do not address potential inaccuracies derived from the heating pad. A feedback-controlled constant temperature mat such as the CMA 450 Temperature Controller (CMA Microdialysis AB, Solna, Sweden) will be used to better maintain core body temperature throughout the heat treatments.

Finally, the optimization presented in this paper is based on temperature. This approach is the most adequate since our goal is to heat the bladder within a certain temperature range to enhance drug delivery. The same modeling strategy could be implemented if using hyperthermia as a stand-alone technique to treat cancer by thermal damage. However, in this case a different optimization algorithm based on cell death should be developed [80].

4.5. Conclusions

A new electro-thermo-fluid (multiphysics) model is proposed to allow a temperature-based optimization of murine bladder heating with a water-cooled microwave applicator. This model incorporates tissue-specific biological data and includes a different approach based on tissue-specific constitutive relationships for blood perfusion and metabolism. This comprehensive analysis shows that temperature dependent biological properties as well as the effects of anesthesia must be accounted to capture the absolute and transient temperatures in mice. Simulations further indicate that the uterus is a convenient surrogate to monitor bladder temperature with a temperature difference of 0.9 °C during heating. The temperature-based optimization proves to

maintain the bladder at a desired therapeutic level [41.5, 43.3] °C while sparing remaining tissues from dangerous temperatures. The good agreement between numerical and experimental results achieved with this multiphysics model demonstrates that it can be used to accurately predict internal temperatures during murine hyperthermia studies. Therefore, electromagnetic and thermo-fluid simulations can be used as a reliable system design and improve treatment planning for hyperthermia applications.

Acknowledgements

The authors would like to acknowledge support from NIH grant CA42745-21-23. Special gratitude to ANSYS and COMSOL for the continuous software support. Dário Barros Rodrigues acknowledges the Portuguese Foundation for Science and Technology (FCT-MEC) for a post-graduate scholarship SFRH/BD/73215/2010 and together with Pedro Pereira and Paulo Limão-Vieira the grant PEst-OE/FIS/UI0068/2011. The authors would also like to acknowledge Donald Pearce Jr. of the Duke University Medical Instrument Shop for his work in constructing the prototype applicators.

References

1. Israel L, Chahinian P, Depierre A: Response of 65 measurable epidermoid bronchogenic tumors of known spontaneous doubling time to four different chemotherapeutic regimens--strategic deductions. Med Pediatr Oncol 1975, 1(2):83-93.

2. Wallner KE, Banda M, Li GC: Hyperthermic enhancement of cell killing by mitomycin C in mitomycin C-resistant Chinese hamster ovary cells. Cancer research 1987, 47(5):1308-1312.

3. Falk MH, Issels RD: Hyperthermia in oncology. International Journal of Hyperthermia 2001, 17(1):1-18.

4. Gofrit ON, Shapiro A, Pode D, Sidi A, Nativ O, Leib Z, Witjes JA, van der Heijden AG, Naspro R, Colombo R: Combined local bladder hyperthermia and intravesical chemotherapy for the treatment of high-grade superficial bladder cancer. Urology 2004, 63(3):466-471.

5. Needham D, Anyarambhatla G, Kong G, Dewhirst MW: A new temperature-sensitive liposome for use with mild hyperthermia: Characterization and testing in a human tumor xenograft model. Cancer Research 2000, 60(5):1197-1201.

6. Vujaskovic Z, Craciunescu O, Stauffer P, Carroll M, Lan L, Dewhirst M, Inman B: Pilot study of external hyperthermia and intravesical mitomycin-C to treat recurrent bladder cancer after failed standard therapy. In: ASCO Annual Meeting: 2010. Journal of Clinical Oncology.

7. Joiner MC, Steel GG, Stephens TC: Response of two mouse tumours to hyperthermia with CCNU or melphalan. Br J Cancer 1982, 45(1):17-26.

8. Peller M, Schwerdt A, Hossann M, Reinl HM, Wang T, Sourbron S, Ogris M, Lindner LH: MR characterization of mild hyperthermia-induced gadodiamide release from thermosensitive liposomes in solid tumors. Invest Radiol 2008, 43(12):877-892.

9. Hill SA, Denekamp J: The effect of vascular occlusion on the thermal sensitization of a mouse tumour. Br J Radiol 1978, 51(612):997-1002.

10. Meyer DE, Shin BC, Kong GA, Dewhirst MW, Chilkoti A: Drug targeting using thermally responsive polymers and local hyperthermia. J Control Release 2001, 74(1-3):213-224.

11. Mukhopadhaya A, Mendecki J, Dong X, Liu L, Kalnicki S, Garg M, Alfieri A, Guha C: Localized hyperthermia combined with intratumoral dendritic cells induces systemic antitumor immunity. Cancer Res 2007, 67(16):7798-7806.

12. Marmor JB, Hilerio FJ, Hahn GM: Tumor eradication and cell survival after localized hyperthermia induced by ultrasound. Cancer Res 1979, 39(6 Pt 1):2166-2171.

13. Marmor JB, Hahn N, Hahn GM: Tumor cure and cell survival after localized radiofrequency heating. Cancer Res 1977, 37(3):879-883.

14. Nomura S, Mukasa S, Yamasaki H, Maehara T, Aono H, Kikkawa H, Satou K, Yukumi S, Watanabe Y: Inductive heating of mg ferrite powder in high-water content phantoms using AC magnetic field for local hyperthermia. Heat Transfer Eng 2007, 28(12):1017-1022.

15. Maehara T, Konishi K, Kamimori T, Aono H, Naohara T, Kikkawa H, Watanabe Y, Kawachi K: Heating of ferrite powder by an AC magnetic field for local hyperthermia. Jpn J Appl Phys 1 2002, 41(3A):1620-1621.

16. Attaluri A, Ma RH, Qiu Y, Li W, Zhu L: Nanoparticle distribution and temperature elevations in prostatic tumours in mice during magnetic nanoparticle hyperthermia. International Journal of Hyperthermia 2011, 27(5):491-502.

17. Sonvico F, Mornet S, Vasseur S, Dubernet C, Jaillard D, Degrouard J, Hoebeke J, Duguet E, Colombo P, Couvreur P: Folate-conjugated iron oxide nanoparticles for solid tumor targeting as potential specific magnetic hyperthermia mediators: Synthesis, physicochemical characterization, and in vitro experiments. Bioconjugate Chem 2005, 16(5):1181-1188.

18. Salahi S, Maccarini PF, Rodrigues DB, Etienne W, Landon CD, Inman BA, Dewhirst MW, Stauffer PR: Miniature microwave applicator for murine bladder hyperthermia studies. International Journal of Hyperthermia 2012, 28(5):456-465.

19. Birkelund Y, Jacobsen S, Arunachalam K, Maccarini P, Stauffer PR: Flow patterns and heat convection in a rectangular water bolus for use in superficial hyperthermia. Physics in Medicine and Biology 2009, 54(13).

20. McIntosh RL, Deppeler L, Oliva M, Parente J, Tambuwala F, Turner S, Winship D, Wood AW: Comparison of radiofrequency exposure of a mouse dam and foetuses at 900 MHz. Physics in Medicine and Biology 2010, 55(4):N111-N122.

21. Paulides MM, Stauffer PR, Neufeld E, Maccarini PF, Kyriakou A, Canters RAM, Diederich CJ, Bakker JF, Van Rhoon GC: Simulation techniques in hyperthermia treatment planning. International Journal of Hyperthermia 2013, 29(4):346-357.

22. Lang J, Erdmann B, Seebass M: Impact of nonlinear heat transfer on temperature control in regional hyperthermia. IEEE Transactions on Biomedical Engineering 1999, 46(9):1129-1138.

23. Trakic A, Crozier S, Liu F: Numerical modelling of thermal effects in rats due to high-field magnetic resonance imaging (0.5-1 GHz). Physics in Medicine and Biology 2004, 49(24):5547-5558.

24. Johnson R, Fowler JF, Zanelli GD: Changes in mouse blood-pressure, tumor blood-flow, and core and tumor temperatures following Nembutal or urethane anesthesia. Radiology 1976, 118(3):697-703.

25. Oconnor MF, Howerton TC, Collins AC: Effects of pentobarbital in mice selected for differential sensitivity to ethanol. Pharmacology Biochemistry and Behavior 1982, 17(2):245-248.

26. Pozar DM: Microwave Engineering, 2nd edn. New York: John Wiley & sons, Inc.; 1998.

27. Nagy TR, Clair AL: Precision and accuracy of dual-energy X-ray absorptiometry for determining in vivo body composition of mice. Obesity Research 2000, 8(5):392-398.

28. Hasgall PA, Neufeld E, Gosselin MC, Klingenböck A, Kuster N: IT'IS Database for thermal and electromagnetic parameters of biological tissues. In. www.itis.ethz.ch/database; 2011.

29. McIntosh RL, Anderson V: A comprehensive tissue properties database provided for the thermal assessment of a human at rest. Biophysical Reviews and Letters 2010, 5(3).

30. Gabriel C: Compilation of the dielectric properties of body tissues at RF and microwave frequencies. In: Occupational and environmental health directorate. Edited by Base BAF. Texas (USA); 1996.

31. Vorst AV, Rosen A, Kotsuka Y: RF/Microwave Interaction with Biological Tissues. Hoboken, NJ: John Wiley & Sons; 2006.

32. Ahlbom A, Bergqvist U, Bernhardt JH, Cesarini JP, Court LA, Grandofo M, Hietanen M, McKinlay AF, Repacholi MH, Sliney DH et al: Guidelines for limiting exposure to time-varying electric, magnetic, and electromagnetic fields (up to 300 GHz) (vol 74, pg 494, 1998). Health Physics 1998, 75(4):442-442.

33. ANSYS I: An introduction to HFSS: Fundamentals principles, concepts, and use. 2012, Release 14.5 www.ansys.com.

34. Neuman DG, Stauffer PR, Jacobsen S, Rossetto F: SAR pattern perturbations from resonance effects in water bolus layers used with superficial microwave hyperthermia applicators. International Journal of Hyperthermia 2002, 18(3):180-193.

35. Gabriel C: Compilation of the dielectric properties of body tissues at RF and microwave frequencies. In. Edited by Occupational and environmental health directorate RRD, vol. Report N.AL/OE-TR- 1996-0037. Brooks Air Force Base, Texas (USA); 1996.

36. Wissler EH: Pennes' 1948 paper revisited. Journal of Applied Physiology 1998, 85:36-42.

37. Pennes HH: Analysis of tissue and arterial blood temperatures in the resting human forearm. Journal of Applied Physiology 1948, 1(2):93-122.

38. Song C, Choi I, Nah B, Sahu S, Osborn J: Microvasculature and perfusion in normal tissues and tumors. In: Thermoradiotherapy and thermochemotherapy. Edited by Seegenschmiedt Mh FPVCCe, vol. Volume 1, Biology, Physiology and Physics. Berlin, New York: Springer-Verlag; 1995: 139-159.

39. Fan J, Wang L: Analytical theory of bioheat transport. Journal of Applied Physics 2011, 109(10).

40. Kolios MC, Worthington AE, Sherar MD, Hunt JW: Experimental evaluation of two simple thermal models using transient temperature analysis. Physics in Medicine and Biology 1998, 43(11):3325-3340.

41. Trakic A, Liu F, Crozier S: Transient temperature rise in a mouse due to low-frequency regional hyperthermia. Physics in Medicine and Biology 2006, 51(7):1673-1691.

42. Grosman B, Shaik OS, Helwig BG, Leon LR, Doyle FJ, III: A physiological systems approach to modeling and resetting of mouse thermoregulation under heat stress. Journal of Applied Physiology 2011, 111(3).

43. Salloum M, Ma RH, Zhu L: An in-vivo experimental study of temperature elevations in animal tissue during magnetic nanoparticle hyperthermia. International Journal of Hyperthermia 2008, 24(7):589-601.

44. Rylander MN, Feng YS, Zhang YJ, Bass J, Stafford RJ, Volgin A, Hazle JD, Diller KR: Optimizing heat shock protein expression induced by prostate cancer laser therapy through predictive computational models. Journal of Biomedical Optics 2006, 11(4).

45. Wooden KM, Walsberg GE: Effect of wind and solar radiation on metabolic heat production in a small desert rodent, Spermophilus tereticaudus. Journal of Experimental Biology 2000, 203(5):879-888.

46. Campbell GS, Norman JM: Introduction to Environmental Biophysics, 2nd edn. Verlag, New York: Springer; 2000.

47. Conley KE, Porter WP: Heat-loss regulation - role of appendages and torso in the deer mouse and the white-rabbit. Journal of Comparative Physiology B-Biochemical Systemic and Environmental Physiology 1985, 155(4):423-431.

48. Gordon CJ: Thermal physiology of laboratory mice: Defining thermoneutrality. Journal of Thermal Biology 2012, 37(8):654-685.

49. Flyckt VMM, Raaymakers BW, Lagendijk JJW: Modelling the impact of blood flow on the temperature distribution in the human eye and the orbit: fixed heat transfer coefficients versus the Pennes bioheat model versus discrete blood vessels. Physics in Medicine and Biology 2006, 51(19):5007-5021.

50. Song CW: Effect of local hyperthermia on blood-flow and microenvironment - a review. Cancer Research 1984, 44(10):4721-4730.

51. Griffin RJ, Dings RPM, Jamshidi-Parsian A, Song CW: Mild temperature hyperthermia and radiation therapy: Role of tumour vascular thermotolerance and relevant physiological factors. International Journal of Hyperthermia 2010, 26(3):256-263.

52. Diller KR, Valvano JW, Pearce JA: Bioheat Transfer. In: The CRC Handbook of Mechanical Engineering, Second Edition. Edited by Frank Kreith DYG. Boca Raton: CRC Press; 2005.

53. Stauffer PR: Evolving technology for thermal therapy of cancer. International Journal of Hyperthermia 2005, 21(8):731-744.

54. Song CW, Lokshina A, Rhee JG, Patten M, Levitt SH: Implication of blood-flow in hyperthermic treatment of tumors. IEEE Transactions on Biomedical Engineering 1984, 31(1):9-16.

55. Tompkins DT, Vanderby R, Klein SA, Beckman WA, Steeves RA, Frye DM, Paliwal BR: Temperature-dependent versus constant-rate blood perfusion modeling in ferromagnetic thermoseed hyperthermia - Results with a model of the human prostate. International Journal of Hyperthermia 1994, 10(4):517-536.

56. Seyde WC, McGowan L, Lund N, Duling B, Longnecker DE: Effects of anesthetics on regional hemodynamics in normovolemic and hemorrhaged rats. American Journal of Physiology 1985, 249(1).

57. Tuma RF, Irion GL, Vasthare US, Heinel LA: Age-related-changes in regional blood-flow in the rat. American Journal of Physiology 1985, 249(3).

58. Stott WT, Dryzga MD, Ramsey JC: Blood-flow distribution in the mouse. Journal of applied toxicology : JAT 1983, 3(6):310-312.

59. Gordon CJ: Quantifying the instability of core temperature in rodents. Journal of Thermal Biology 2009, 34(5):213-219.

60. Sessler DI: Temperature monitoring and perioperative thermoregulation. Anesthesiology 2008, 109(2):318-338.

61. Gillooly JF, Brown JH, West GB, Savage VM, Charnov EL: Effects of size and temperature on metabolic rate. Science 2001, 293(5538):2248-2251.

62. Brown JH, Gillooly JF, Allen AP, Savage VM, West GB: Toward a metabolic theory of ecology. Ecology 2004, 85(7):1771-1789.

63. Allen AP, Gillooly JF: The mechanistic basis of the metabolic theory of ecology. Oikos 2007, 116(6):1073-1077.

64. White CR, Phillips NF, Seymour RS: The scaling and temperature dependence of vertebrate metabolism. Biology Letters 2006, 2(1):125-127.

65. Gillooly JF, Allen AP, Savage VM, Charnov EL, West GB, Brown JH: Response to Clarke and Fraser: effects of temperature on metabolic rate. Functional Ecology 2006, 20(2):400-404.

66. Yao J, Maslov KI, Zhang Y, Xia Y, Wang LV: Label-free oxygen-metabolic photoacoustic microscopy in vivo. Journal of Biomedical Optics 2011, 16(7).

67. Barclay C, Woledge R, Curtin N: Effects of UCP3 genotype, temperature and muscle type on energy turnover of resting mouse skeletal muscle. Pflugers Archiv-European Journal of Physiology 2009, 457(4):857-864.

68. Gordon CJ, Stead AG: Effect of ethyl-alcohol on thermoregulation in mice following the induction of hypothermia or hyperthermia. Pharmacology Biochemistry and Behavior 1988, 29(4):693-698.

69. Wang ZM, O'Connor TP, Heshka S, Heymsfield SB: The reconstruction of Kleiber's law at the organ-tissue level. Journal of Nutrition 2001, 131(11):2967-2970.

70. Roberts MF, Lightfoot EN, Porter WP: A New Model for the Body Size-Metabolism Relationship. Physiological and Biochemical Zoology 2010, 83(3):395-405.

71. Mankoff DA, Dunnwald LK, Partridge SC, Specht JM: Blood Flow-Metabolism Mismatch: Good for the Tumor, Bad for the Patient. Clinical Cancer Research 2009, 15(17).

72. Anderson J, Degrez G, Degroote J, Dick E, Grundmann R, Vierendeels J: Computational Fluid Dynamics: Springer; 2009.

73. Incropera FP, Dewitt DP, Bergman TL, Lavine AS: Fundamentals of heat and mass transfer, 6th edn. USA: John Wiley & Sons, Inc.; 2007.

74. Inman BA, Etienne W, Rubin R, Owusu RA, Oliveira TR, Rodriques DB, Maccarini PF, Stauffer PR, Mashal A, Dewhirst MW: The impact of temperature and urinary constituents on urine viscosity and its relevance to bladder hyperthermia treatment. Int J Hyperthermia 2013.

75. Briggs WL, Henson VE, McCormick SF: A Multigrid Tutorial, 2nd edn: The Society for Industrial and Applied Mathematics (SIAM); 2000.

76. Drizdal T, Togni P, Visek L, Vrba J: Comparison of Constant and Temperature Dependent Blood Perfusion in Temperature Prediction for Superficial Hyperthermia. Radioengineering 2010, 19(2):281-289.

77. COMSOL: COMSOL Multiphysics User's guide. 2011, v4.2 www.comsol.com.

78. Chen X, Diederich CJ, Wootton JH, Pouliot J, Hsu IC: Optimisation-based thermal treatment planning for catheter-based ultrasound hyperthermia. International Journal of Hyperthermia 2010, 26(1):39-55.

79. Gordon CJ: Influence of heating rate on control of heat-loss from the tail in mice. American Journal of Physiology 1983, 244(6):R778-R784.

80. Pearce JA: Comparative analysis of mathematical models of cell death and thermal damage processes. International Journal of Hyperthermia 2013, 29(4):262-280.

CHAPTER 4

Chapter 5

Concluding remarks

This thesis outlines a robust method for the development of target-specific models. The end goal is to couple all relevant physics in a single approach and include the interaction between a medical device and the specific target in a virtual environment. This way, both medical device and therapeutic or diagnostic techniques are optimized for their specific goals. The medical devices explored here are microwave antennas both used in the passive and active mode. The antenna design is implemented using the specific target and its surrounding relevant structures. A single physics is used to compute the electric fields and a power-based optimization algorithm is established to improve the antenna efficiency. However, to simulate all relevant physical and biological phenomena, we need to introduce a multiphysics model. By accounting the heat transfer and fluid dynamics together with a temperature-based optimization algorithm, one can design a treatment planning for cancer therapy and thus treat the disease with higher efficiency.

The main drawback of computer modeling is the need of experimental validation. However, combining both strategies produces more effective medical devices and reduces the product development cycle. This is implemented by identifying and characterizing the target tissue and its relevant surrounding structures with accurate 3D imaging and segmentation techniques. The next step is to design the antenna and couple it with the previous segmented CAD model. The final design is then optimized in a simulation environment centered on target-defined specifications. Experimental data is used whenever possible in this iterative process, e.g., in thermophysical properties or boundary conditions. A final experimental setup is always a required component to validate the design and its results. This combined approach are in agreement with the new commission set recently by the National Institutes of Health (NIH) to provide

procedures to standardize the verification and validation of computational modeling for medical devices.

The combined approach between modeling and experiment is used to design and manufacture a radiometric sensor for brain temperature monitoring. The key element of the sensor is a tapered 2.5 cm log-spiral antenna. Its optimized design allow an average antenna efficiency of 50.3 % in the optimized [1.1, 1.6] GHz band, where the efficiency is given by ratio between the power collected from brain and all the power collected by the antenna. This particular arrangement presents a theoretical bandwidth Δf = 530 MHz that fits the standard for ultra-wideband (UWB) designation. The materials chosen allow to manufacture a 2.5 cm log-spiral antenna embedded in a 2.8 cm low-cost radiometric sensor with sufficiently small size to be conformal with the human head during surgery. The sensor is tested on a full scale multi-layer tissue phantom of the human head. The calculated radiometric equivalent brain temperature tracks within 0.4 °C of measured brain phantom temperature, when the brain phantom is lowered 10 °C and then returned to original temperature (37 °C) over a 4.6-hour experiment. A clinical case confirms our ability to non-invasively monitor temperature in deep brain that correlates loosely with core measurements in rectum and nasopharynx. The simulations demonstrate the different received energy contributions from scalp, skull and brain tissues, which pave the way for temperature profiling in the human head. We anticipate that this newly developed sensor can help reducing surgical complications, thereby reducing overall costs and improving clinical outcomes for patients in recovery from post-surgical hypothermia.

It is clear that hyperthermia enhances the effects of chemo- and radiotherapies. The presented microwave applicator and the target-specific multiphysics modeling (TSMM) approach is intended to allow scientists to investigate the basic principles underlying the increased effectiveness of using adjuvant hyperthermia in chemo- and radiotherapies. Results confirm that using the TSMM approach one can heat effectively and non-invasively murine regions located at depth with minimal increase in core temperature. The implemented analysis shows that temperature dependent biological properties as well as the effects of anesthesia must be accounted to accurately capture the absolute and transient temperature variations in mice during microwave heating. Simulations further indicate that the uterus is a convenient surrogate to monitor bladder temperature. The thermal-based optimization proved the feasibility of maintaining the bladder at a

desired therapeutic level [41.5, 43.3] °C while sparing surrounding tissues from dangerous temperatures. Therefore, electromagnetic and thermo-fluid simulations can be used to provide reliable system design and improved treatment planning for hyperthermia in murine studies. Additionally, these pre-clinical studies facilitate the characterization of the pharmacokinetics and pharmacodynamics of novel chemotherapeutic drugs packaged in thermally sensitive liposomes, thereby expediting the translation of new therapeutic approaches into clinical trials.

To summarize, the main contributions of this thesis are the following: (1) the development of an analytical solution to characterize the heat transfer in a multi-layer perfused tissue; (2) the design and manufacturing of a multi-layer physical model of the human head that surrogates the temperature distribution across the scalp, with adjustable thickness, bone and brain; (3) the design and manufacturing of a new antenna design for brain temperature monitoring; (4) the development of a comprehensive target-specific multiphysics model to allow focused microwave heating in murine bladder, where the temperature outcome can be predicted *in silico*.

CHAPTER 5

Biography

Dário Barros Rodrigues

Born

October 5, 1984

Coimbra, Portugal

Education

- **Universidade Nova de Lisboa, Lisbon Portugal**
  PhD in Biomedical Engineering, November 2013
  MS in Biomedical Engineering, December 2007
  BS in Biomedical Engineering, July 2005
- **Duke University, Durham USA**
  Research Scholar (2011-2013)

Honors and Affiliations

- Best Student Award for Integrated BS+MS Program in Biomedical Engineering (2002-2007)
- National Graduate Research Scholarship (2008-2010) SFRH/BD/42305/2007 from the Portuguese Foundation for Science and Technology (FCT-MCTES)
- International Graduate Research Scholarship (2011-2012) SFRH/BD/73215/ 2010 from FCT-MCTES
- ANSYS Hall of Fame 2013
- 2013 New Investigator Travel Award (Society for Thermal Medicine) sponsored by NIH

- IEEE Member (since 2011)
- Biomedical Engineering Society Member (since 2012)
- Society of Thermal Medicine Member (since 2012)
- European Microwave Association (since 2013)
- International Society for Optics and Photonics (since 2013)

Full articles

1. **Rodrigues DB**, Maccarini PF, Salahi S, Oliveira TO, Pereira PJS, Limao-Vieira P, Snow BW, Reudink D, Stauffer PR: Design and optimization of an ultra-wideband and compact microwave antenna for radiometric monitoring of brain temperature. Progress In Electromagnetics Research 2013, Submitted.
2. **Rodrigues DB**, Salahi S, Pereira PJS, Limão-Vieira P, Landon CD, Oliveira TR, Etienne W, Inman BA, Dewhirst MW, Stauffer PR et al: Target-specific multiphysics model for murine bladder heating studies. Physics in Medicine and Biology 2013, Submitted.
3. Stauffer PR, Snow BW, **Rodrigues DB**, Salahi S, Oliveira TR, Reudink D, Maccarini PF: Non-Invasive Core Temperature Measurement in Brain: Demonstration in a Head Phantom and Initial Clinical Experience. The Neuroradiology Journal 2013, Submitted.
4. E Colebeck, Hood AZ, **Rodrigues DB**, Maccarini PF, Stauffer PR, TopSakal E: Measurement of microwave dielectric properties of brown and white adipose tissue in rats. Physics in Medicine and Biology 2013, Submitted.
5. **DB Rodrigues**, PJS Pereira, PM Limao-Vieira, PR Stauffer, and PF Maccarini. "Study of the one dimensional and transient bioheat transfer equation: multilayer solution development and applications." International Journal of Heat and Mass Transfer; 62:153-162 2013.
6. **DB Rodrigues**, PF Maccarini, S Salahi, E Colebeck, E Topsakald, PJS Pereira, P Limao-Vieira, and PR Stauffer "Numerical 3D modeling of heat transfer in human tissues for microwave radiometry monitoring of brown fat metabolism." SPIE proceedings of the Conference on Energy-Based Treatment of Tissue and Assessment VII; 2013 February 2-7; San Jose CA, USA.
7. PR Stauffer, S Salahi, **DB Rodrigues**, E Topsakal, TO Ribeiro, A Prakash, and PF Maccarini. "Stable Microwave Radiometry System for Long Term Monitoring of Deep Tissue Temperature." SPIE proceedings of the Conference on Energy-Based Treatment of Tissue and Assessment VII; 2013 February 2-7; San Jose CA, USA. Invited Proceeding.
8. BA Inman, W Etienne, R Rubin, RA Owusu, TO Ribeiro, **DB Rodriques**, PF Maccarini, PR Stauffer, MW Dewhirst. "The impact of temperature and urinary constituents on urine viscosity and its relevance to bladder hyperthermia treatment" International Journal of Hyperthermia; 29(3):206-210 2013.
9. S Salahi, PF Maccarini, **DB Rodrigues**, W Etienne, CD Landon, BA Inman, MW Dewhirst, and PR Stauffer. "Miniature Microwave Applicator for Murine Bladder Hyperthermia Studies." International Journal of Hyperthermia; 28(5):456-65 2012.
10. **DB Rodrigues**, PJS Pereira, PM Limao-Vieira, and PF Maccarini. "Analytical solution to the transient 1D bioheat equation in a multilayer region with spatial dependent heat sources." Proceedings of the BIOMED 2011; 2011 February 16-18; Innsbruck, Austria, Proceeding No. 723-092, Pages 96-103.

11. **DB Rodrigues** and VB Vassilenko. "Characterization of pressure reduction/relief devices regarding to temperature and galvanic skin response." Proceedings of the 3rd National Conference on Biomechanics; 2009 February 11-12; Bragança, Portugal.

Full articles (to be submitted)

1. Analytical solution to the transient 2D bioheat equation in a multilayer region with spatial dependent heat sources. European Journal of Applied Mathematics.
2. **Rodrigues DB**, Oliveira TR, Salahi S, Aknine G, Maccarini PF, Stauffer PR: Metamaterial-inspired antenna for phased array heating of adult bladder. Physics in Medicine and Biology.
3. Oliveira TR, Salahi S, **Rodrigues DB**, Stauffer PR, Wilson C, Grant G, Dewhirst M, Maccarini PF: Design of low-cost and noninvasive microwave applicator to thermal activate the drug delivery in murine brain tumor. IEEE Transactions on Biomedical Engineering.
4. Oliveira TR, Wilson C, Salahi S, **Rodrigues DB**, Stauffer PR, Grant G, Dewhirst M, Maccarini PF: Noninvasive mild hyperthermia and thermosensitive liposome for enhanced intratumoral drug delivery in glioblastoma multiforme. Journal of Controlled Release.
5. Maccarini PF, **Rodrigues DB**, Oliveira TR, Stauffer PR: Radiometric profiling for brain temperature monitoring. IEEE Transactions on Biomedical Engineering.

Conference abstracts and posters

1. **DB Rodriques**, PR Stauffer, S Salahi, PF Maccarini. "Design of 3D conical log-spiral antenna for focused radiometric deep temperature readings". Proceedings of the Society of Thermal Medicine; 2013 April 17-21; Aruba, USA.
2. PR Stauffer, **DB Rodriques**, TO Ribeiro, E Topsakal, PF Maccarini. "Microwave Radiometry System for Non-invasive Long Term Monitoring of Deep Tissue Temperature". Proceedings of the Society of Thermal Medicine; 2013 April 17-21; Aruba, USA.
3. PR Stauffer, PF Maccarini, **DB Rodriques**, S Salahi, O Craciunescu, Y Yuan, S Das. "Towards Integration of Treatment Monitoring with Thermal Modeling for Improved Control of Heat Treatments" The 11th International Congress of Hyperthermic Oncology; 2012 August 28-31; Kyoto, Japan. Invited Abstract.
4. **DB Rodrigues**, S Salahi, PJS Pereira, P Limao-Vieira, PF Maccarini, and PR Stauffer. "A temperature optimization technique for localized heating in small animals." Proceedings of the Society of Thermal Medicine; 2012 April 13-16; Portland OR, USA, Abstract No. 0006.

5. S Salahi, **DB Rodrigues**, PF Maccarini, and PR Stauffer. "Wideband conformal metamaterial antenna for pediatric bladder hyperthermia." Proceedings of the Society of Thermal Medicine; 2012 April 13-16; Portland OR, USA, Abstract No. 0037.
6. S Salahi, PF Maccarini, **DB Rodrigues**, MW Dewhirst, and PR Stauffer. "Miniature microwave applicators for focused heating in small animals." Poster at the Society of Thermal Medicine 2011 Annual Meeting; 2011 April 26-28; Washington, USA.
7. **DB Rodrigues** and VB Vassilenko. "Principles and Applications of Experimental Measurement of Galvanic Skin Response." Poster at the 16th National Conference on Physics; 2008 September 3-6; Caparica, Portugal.

Invited Talks (most relevant)

1. "Target-Specific Multiphysics Modeling For Thermal Medicine Applications: the role of a Biomedical Engineer." Biomedical and Biophysics Engineering course; 2013 November 29; Lisboa, Portugal.
2. "Target-Specific Multiphysics Modeling For Thermal Medicine Applications." IBEB Seminars; 2013 November 19; Lisboa, Portugal.
3. "Advanced multiphysics modeling for applications in thermal medicine." CEFITEC Seminars; 2012 September 19; Caparica, Portugal.
4. "Advanced multiphysics modeling in thermal medicine." 7th Annual Meeting of Biomedical Engineering Students; 2012 March 8-11; Marinha Grande, Portugal.
5. "Multiphysics modeling in thermal medicine: from the model to clinic." Duke Seminars in Medical Physics; 2012 February 18; Durham, USA.
6. "CE marking, optimization and characterization of a pressure reduction surface to bedded patients." Biomedical Engineering: Past, Present and Future; 2009 May 21; Setúbal, Portugal.
7. "Development of a non-invasive probe to measure blood perfusion using thermal diffusion technique." 3rd Seminar on Biomedical Engineering; 2008 December 11-12; Bragança, Portugal.
8. "CE marking, optimization and characterization of a pressure reduction surface to bedded patients." 3rd Annual Meeting of Biomedical Engineering Students; 2008 April 17-20; Vila Nova de Milfontes, Portugal.